THE UNIVERSITY *of* EDINBURGH

The Topological Properties of SnTe and Fe_3Sn_2

Christopher O'Neill
Principal Supervisor - Andrew Huxley

A thesis submitted in fulfilment of the requirements
for the degree of Doctor of Philosophy
to the
University of Edinburgh

Abstract

The aim of this thesis was to identify topologically protected states in the materials SnTe and Fe_3Sn_2. Such states are currently receiving a large amount of interest due to their applications for spintronic devices. Recently SnTe was discovered to be a crystalline topological insulator, a state of matter where its surface is highly conducting while the bulk remains insulating. However detection of these surface states is difficult using transport measurements, since the bulk is not totally insulating but still contains a large number of free carriers.

SnTe undergoes a rhombohedral structural distortion on cooling caused by a soft transverse optic phonon, with the exact T_c strongly dependent on the carrier concentration. The distortion acts to lower crystal symmetry removing some of the symmetries that protect the surface state. Single crystal samples displaying the structural transition were grown and investigated using inelastic X-ray scattering to measure the phonon softening previously reported by other authors. The soft phonon was seen to recover again after distortion indicative of a 2^{nd} order ferroelectric transition. This is the first reported discovery of the recovery showing the distortion is ferroelectric in nature.

Shubnikov de Haas quantum oscillations were measured to study the Fermi surface under ambient and high hydrostatic pressure conditions. A distortion of the Fermi surface caused by the structural transition was evident, resulting in 4 distinct oscillation frequencies. However at applied pressures above 6 kbar, the transition was suppressed and only 1 oscillation measured. A two component Hall response also becomes apparent under high pressure. The possible origin of this and its relation to possible surface states is discussed.

The anomalous Hall effect was also measured in the ferromagnet Fe_3Sn_2 which has a bilayer Kagome structure. Previous measurements on polycrystalline Fe_3Sn_2 suggested a non-collinear spin rotation from the spins pointing along the c-axis

at high temperature to lying in the a-b plane below 80 K. A spin glass phase is then expected below 80 K. Single crystal magnetisation measurements carried out in this thesis show the spins are in the a-b plane at high temperatures and begin to display a ferromagnetic component along the c-axis approaching 80 K. The difference is accounted for by considering the demagnetising factor in the plate shaped single crystals. For this temperature range an applied field along the c-direction however rotates the moments towards c. At intermediate fields there are strong features evident in both the anomalous Hall effect and magnetoresistance. These features may be due to a topological Hall effect caused by a non-collinear spin structure. The possible existence of Skyrmion excitations was also recently discussed theoretically in Fe_3Sn_2. Our data is more suggestive of static Skyrmions known to cause topological Hall effects in MnSi.

Lay Summary

In this thesis I describe the research I have done during my PhD to identify topologically protected states using transport measurements. Such protected states are currently receiving a large amount of interest due to their possible applications in spintronic devices. The research was split into two projects working on different materials, namely single crystals of SnTe and Fe_3Sn_2.

SnTe was recently discovered to be a crystalline topological insulator, where its surfaces are highly conducting and are topologically protected by the mirror symmetry of the lattice. However on cooling it undergoes a rhombohedral distortion that lowers the crystal symmetry, destroying some of the surface states. Single crystal samples were grown and the phonon dispersion curves measured using inelastic X-ray scattering. A soft transverse optic phonon was seen to recover again after distortion indicating the transition is ferroelectric in nature. Transport measurements under ambient and high hydrostatic pressure conditions contained Shubnikov de Haas quantum oscillations. The oscillations showed the distortion is suppressed at pressures above 6 kbar and a two component Hall response also becomes apparent, possibly due to the surface states, is discussed.

The ferromagnet Fe_3Sn_2 was also investigated and compared to previous measurements on polycrystals by other authors who suggested a non-collinear spin rotation from the c-axis to the a-b plane on cooling. Single crystal magnetisation measurements carried out in this thesis show the spins are in the a-b plane at high temperatures and rotate towards the c-axis on cooling. The difference is accounted for by the demagnetising factor of the single crystals. For small applied fields along the c-axis, there are strong features in both the anomalous Hall effect and magnetoresistance. These may possibly be due to a topological Hall effect like that seen in MnSi caused by static Skyrmions.

Declaration

Except where otherwise stated, the research undertaken in this thesis was the unaided work of the author. Where the work was done in collaboration with others, a significant contribution was made by the author.

C. O'Neill

Acknowledgements

I would like to begin by thanking my supervisor Prof. Andrew Huxley for giving me the opportunity to carry out the work in this thesis and for his guidance throughout. I would also like to thank Dr Dmitry Sokolov, Dr Chris Stock and Dr Andreas Hermann for their help and guidance. Further to this I would like to thank Dr Andrew Wills for providing crystals, Dr Konstantin Kamenev in helping with and providing pressure cells and Dr Alexei Bossak for beam line assistance on ID28. Also the workshop staff, particularly Mr Andrew Downie and Mr Ronnie Proc for their help. My office mates Julian Schmehr, William Whitley and Rachel Husband. Other group members Dr Jean-Philippe Reid, Calum Lithgow and Michal Kepa for their help. I would also like to thank the CM-DTC management, particularly Mrs Christine Edwards, Dr Julie Massey and Dr Chris Hooley.

Outside work there are many people I would like to thank for their support. My friends David Moody, David Meehan, James Carroll, Philip McAllister, Will Lynch, Rory Collins, Maeve Bambury, Brendan Reynolds, David Bruce, Jon Reid, Andrew Wildgoose and Lee McDonald. Everyone involved in Boroughmuir RFC, where I have spent many happy days and nights during the course of this PhD. In particular Derick Gunn MacLeod and Andy Hood for their lifts to and from training, the Sunday night quiz team and the Bears group. Most of all I would like to thank my parents Gerard and Sadie who have helped and supported me throughout, my brother Gareth and sisters Michelle and Joanne.

Contents

List of Figures

List of Tables

Chapter 1

Introduction

This chapter introduces the recently discovered states known as topological insulators. First the idea of Berry phases and topology is discussed in relation to Bloch bands. This is followed by examples of topological insulators such as Bi_2Te_3. The new class of materials known as crystalline topological insulators is then considered, of which SnTe is an example. A literature review of SnTe is given along with a brief introduction to the theory behind the observed structural transition in this material. Fermi surface measurements are also discussed via quantum oscillations.

1.1 The Berry Phase and Topological Insulators

Traditionally transport phenomena in crystals are treated within the semiclassical formalism. Macroscopic crystals are defined by their periodic unit cell, that contains all of the structural and symmetry information. Electronic states are then described in terms of crystal momentum $\mathbf{k}$, where the unit cell in momentum space is called the Brillouin zone. The conduction electrons are treated as being in a periodic potential $u(\mathbf{r})$ and are described by Bloch waves $\psi_{n\mathbf{k}}(\mathbf{r})$ of the form

$$\psi_{n\mathbf{k}}(\mathbf{r}) = \mathrm{e}^{\mathbf{ik}\cdot\mathbf{r}} u_{n\mathbf{k}}(\mathbf{r}) \tag{1.1}$$

where n is known as the band index, since many Bloch waves exist at each value of $\mathbf{k}$. Due to the periodicity

$$u_{n\mathbf{k}}(\mathbf{r}+\mathbf{R}) = u_{n\mathbf{k}}(\mathbf{r}) \tag{1.2}$$

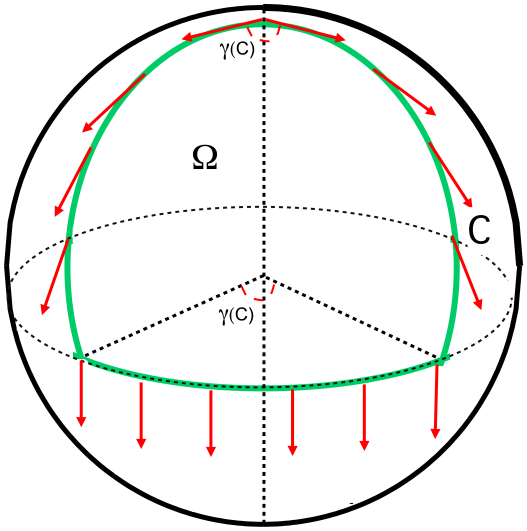

Figure 1.1: *An example of parallel transport around a closed path C. A tangent vector shown as the red arrow begins at the North pole and moves along the surface of the sphere. During its travel it does not rotate perpendicularly to the surface. Upon completion of C, shown as the green line, the vector has now gained a geometrical angle $\gamma(C)$.*

where $\mathbf{R}$ is any reciprocal lattice vector, all distinct Bloch waves occur within the first Brillouin zone. Each $\psi_{n\mathbf{k}}(\mathbf{r})$ defined and in the Brillouin zone are eigenstates of the Hamiltonian $H_{\mathbf{k}}$ with energy eigenvalues $\varepsilon_{n\mathbf{k}}$. The set of electronic levels specifed by $\varepsilon_n(\mathbf{k})$ define the energy band structure of the solid. The Fermi surface is then made up of partially filled bands. An electron within a band, n, when placed in an external electric field has a group velocity

$$v_n(\mathbf{k}) = \frac{1}{\hbar}\nabla_{\mathbf{k}}\varepsilon_n(\mathbf{k}) \tag{1.3}$$

which is of fundamental importance in describing the transport properties in the solid.

However it has now been widely acknowledged that equation (1.3) is not totally complete, but that an extra velocity term arises due to the Berry phase. The Berry phase belongs to the field of holonomy and is a geometrical phase angle caused by parallel transport [1]. An example of parallel transport is shown in Figure 1.1. A particle with a tangent vector begins on the north pole. As

it moves along the surface of the sphere, following the green path, it does not rotate about an axis perpendicular to the surface. When the particle returns to the North pole it is not at its initial direction but at an angle $\gamma(C)$.

Berry [2] showed a quantum state will acquire such a geometrical phase $\gamma(C)$, during an adiabatic evolution of the system. The state is described by a time dependent Hamiltonian and set of parameters given by $\mathbf{R} = (R_1, R_2, ...)$. Then

$$H = H(\mathbf{R}), \quad \mathbf{R} = \mathbf{R}(t) \tag{1.4}$$

and $\mathbf{R}(t)$ moves slowly along a closed path C in parameter space. The original state $|n, \mathbf{R}(0)\rangle$ will have evolved to $|n, \mathbf{R}(t)\rangle$ and the eigenstate $|\psi\rangle$ gained a geometric phase component γ_n. This angle, γ_n, is called the Berry phase. For a closed path C in the adiabatic regime $\mathbf{R}(t) = \mathbf{R}(0)$ and $|\psi(t)\rangle$ must satisfy the time-dependent Schrödinger equation (TDSE). Then from the TDSE the Berry phase, γ_n, is obtained

$$\gamma_n = i \oint_C d\mathbf{R} \cdot \langle n, \mathbf{R} | \nabla_R | n, \mathbf{R} \rangle \tag{1.5}$$

usually written

$$\gamma_n = \oint_C d\mathbf{R} \cdot \mathbf{A_n}(\mathbf{R}) \tag{1.6}$$

where $\mathbf{A}(\mathbf{R}) = i\langle n, \mathbf{R} | \nabla_R | n, \mathbf{R} \rangle$ is a vector valued function known as the Berry potential or Berry connection which is gauge-dependent. The Berry potential can then be described as a gauge field tensor using Stokes theorem, described in Xiao *et al*. [3], where

$$\mathbf{\Omega_n}(\mathbf{R}) = \nabla_\mathbf{R} \times \mathbf{A_n}(\mathbf{R}) \tag{1.7}$$

$$\gamma_n = \int_S d\mathbf{S} \cdot \mathbf{\Omega}_n(\mathbf{R}) \tag{1.8}$$

and $\mathbf{\Omega_n}(\mathbf{R})$ is the Berry curvature, which is gauge invariant.

The Berry curvature can also be written as a sum over all eigenstates, the simplest case being a 2 level system. Xiao *et al*. [3] describe a 2-level system with a Hamiltonian of the form

$$H = \mathbf{h}(\mathbf{R}) \cdot \sigma \tag{1.9}$$

where σ are the Pauli matrices. The direction of $\mathbf{h}(\mathbf{R})$ in space is the control parameter of the Hamiltonian with azimuthal angle θ and polar angle ϕ, on a

sphere S^2. The two eigenstates with energies $\pm h$ are then

$$\mid u_- \rangle = \begin{pmatrix} \sin\frac{\theta}{2}e^{-i\phi} \\ -\cos\frac{\theta}{2} \end{pmatrix}, \mid u_+ \rangle = \begin{pmatrix} \cos\frac{\theta}{2}e^{-i\phi} \\ \sin\frac{\theta}{2} \end{pmatrix} \tag{1.10}$$

and an arbitrary phase could be added if needed. The Berry connection for the lower energy level is then

$$A_\theta = \langle u \mid i\partial_\theta u \rangle = 0 \tag{1.11}$$

$$A_\phi = \langle u \mid i\partial_\phi u \rangle = \sin^2\frac{\theta}{2} \tag{1.12}$$

and the Berry curvature

$$\Omega_{\theta\phi} = \partial_\theta A_\phi - \partial_\phi A_\theta = \frac{1}{2}\sin\theta. \tag{1.13}$$

If a new gauge is chosen by multiplying $\mid u_- \rangle$ by $e^{i\phi}$, the Berry connections are $A_\theta = 0$ and $A_\phi = -\cos^2\frac{\theta}{2}$ while $\Omega_{\theta\phi}$ remains the same. In this case, the Berry phase corresponding to any given path on the sphere S^2 is just half the solid angle of the path. The integral of the Berry curvature over the sphere is then

$$\int_{S^2} d\theta d\phi \Omega_{\theta\phi} = 2\pi \tag{1.14}$$

i.e. is quantised in units of $2m\pi$ where m, in this case equal to 1, is known as the Chern number.

Bloch bands can also be imagined to form a closed surface like the surface at fixed $\mathbf{h}$ in the two level model above. Consider an external electric field applied to a Bloch electron. The electrostatic potential $\phi(\mathbf{r})$ due to the uniform electric field $\mathbf{E}$ would grow linearly in space because $\phi(\mathbf{r}) = -\mathbf{E}\cdot\mathbf{r}$ breaking the periodicity so Bloch's theorem could not be applied. To get around this let the electric field come from a time dependent vector potential $\mathbf{A}(t)$ then the Hamiltonian is

$$H = \frac{1}{2m}(\mathbf{p} - e\mathbf{A}(t))^2 + V(\mathbf{r}) \tag{1.15}$$

where V is the potential of the ions and for a constant electric field $\mathbf{A}(t) = -\mathbf{E}t$. Transforming to the $\mathbf{k}$ space

$$H(\mathbf{k}, t) = H(\mathbf{k} + \frac{e}{\hbar}\mathbf{A}(t)) \tag{1.16}$$

giving $\mathbf{k}(t) = \mathbf{k}_0 - e\mathbf{E}t/\hbar$. Then $\mathbf{k}$'s equation of motion is

$$\dot{\mathbf{k}} = -\frac{e}{\hbar}\mathbf{E} \tag{1.17}$$

so the group velocity of the electrons in an applied electric field, is given by

$$v_n(\mathbf{k}) = \frac{1}{\hbar}\nabla_{\mathbf{k}}\varepsilon_n(\mathbf{k}) - \frac{e}{\hbar}\mathbf{E} \times \mathbf{\Omega}_n(\mathbf{k}) \tag{1.18}$$

where $\mathbf{\Omega}_n(\mathbf{k})$ is the berry curvature of the Bloch band

$$\mathbf{\Omega}_{(\mathbf{k})} = \nabla_{\mathbf{k}} \times \langle u_n(\mathbf{k})|i\nabla_{\mathbf{k}}|u_n(\mathbf{k})\rangle \tag{1.19}$$

in $\mathbf{k}$ space [3]. So by letting $\mathbf{k}$ play the role of the parameter $\mathbf{R}$ in the previous 2 level example a Berry curvature is defined $\mathbf{\Omega}_{(\mathbf{k})}$, which alters the response of the electron from that of equation (1.3). This extra velocity term $\frac{e}{\hbar}\mathbf{E} \times \mathbf{\Omega}_n(\mathbf{k})$ acting perpendicularly to the applied field is of fundamental importance in describing phenomenon such as the anomalous Hall effect (AHE) in ferromagnets discussed in Chapter 5 or the integer quantum hall effect discussed here.

However there are many cases where the original velocity formula describes the electron velocity well without the need for the anomalous Berry term. This is understood by symmetry considerations [3]. In the case of time reversal symmetry, T,

$$\mathbf{\Omega}_n(-\mathbf{k}) = -\mathbf{\Omega}_n(\mathbf{k}) \tag{1.20}$$

where $v_n(\mathbf{k})$ and $\mathbf{k}$ have changed sign but $\mathbf{E}$ doesn't. For inversion symmetry, P,

$$\mathbf{\Omega}_n(-\mathbf{k}) = \mathbf{\Omega}_n(\mathbf{k}) \tag{1.21}$$

where $v_n(\mathbf{k})$, $\mathbf{k}$ and E have changed sign. If a system contains both these symmetry operations then the Berry curvature of the Bloch bands will be zero. Therefore either T or P must be broken for Berry phase effects to be observable.

As already mentioned the (AHE) in ferromagnets where T is broken contains an anomalous velocity $\frac{e}{\hbar}\mathbf{E} \times \mathbf{\Omega}_n(\mathbf{k})$. Another example of broken T and observable Berry effects is the integer quantum Hall effect (IQHE) in a 2 dimensional gas of electrons. In a normal current carrying 3D metal when a magnetic field, $\mathbf{B}$, is applied perpendicular to the current direction, the electrons experience the

Lorentz force, giving them a cyclotron motion of frequency $\omega_c = eB/m^*$ for carriers with charge e and effective mass m^*. This results in a voltage appearing across the sample which will be proportional to $\mathbf{B}$, known as the normal Hall effect. In the case of an electron gas confined to 2 dimensions for an applied magnetic field the band structure is made up of equally spaced Landau levels [4] (see section 1.2.3 for description of Landau levels). If the Fermi level lies between the levels then its just a 2 dimensional band insulator.

For a non-zero value of $\Omega_{k_x k_y}$ the Hall conductivity will then come from summing up all the velocities of all occupied bands

$$\sigma_{xy} = \frac{e^2}{\hbar} \int \frac{d^2k}{(2\pi)^2} \Omega_{k_x k_y}. \tag{1.22}$$

If this integral is carried out for the whole of the Brillouin zone which is a closed surface then it must be equal to an integer. Thus for a full Brillouin zone the Hall conductivity is quantised in units of $\frac{e^2}{\hbar}$ i.e.

$$\sigma_{xy} = \frac{ne^2}{h} \tag{1.23}$$

where n is an integer. The Chern number for each filled band gives the number of units it contributes.

A more complete discussion shows how a periodic lattice is constructed and why the Chern number for each band is non-zero [5]. Since the bulk is an insulator the Hall current is carried around the edge of the specimen and the gap is required to close there. The edge currents are chiral where all electrons move in the same direction as shown in Figure 1.2 (a). They are also robust against scattering since there are no availble states to back scatter into.

In 2005, Kane and Mele [6] predicted the existence of the quantum spin Hall effect in 2 dimensions by considering the effect of the spin-orbit interaction (SOI) between the electrons spin and orbital momentum. The SOI splits the bands. Pairs of spin-split bands can cross resulting in pairs of filled bands with equal and opposite Chern numbers so overall T is conserved and no external magnetic field is required. The edge states then consist of up spins going round the sample in one direction while the down spins travel in the opposite direction as shown in Figure 1.2 (b). Even though electrons move forward and backward at the same edge, backscattering is forbidden because an electron needs to flip its spin which

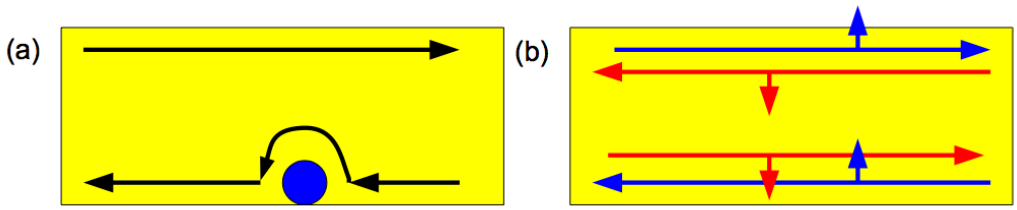

Figure 1.2: (a) *The chiral edge states in the integer quantum Hall state. On meeting an impurity there are no states to backscatter into and the current continues around.* (b) *The quantum spin insulator, there are now counterpropagating channels of up (blue) and down (red) spins. This state is also topological and but now protected by time reversal symmetry.*

requires the breaking of T. They are then topologically protected and can be thought of as two copies of integer quantum Hall effect. Two metallic edge states of opposite spins then cross the band gap while the bulk remains insulating.

Although Kane and Mele discussed graphene in their paper its SOI is actually quite weak. This pointed towards heavier elements with a larger SOI. König *et al.* [7] carried out experiments on semiconductor HgTe/CdTe quantum wells where HgTe was sandwiched between CdTe layers. CdTe is a semiconductor with a s-type conduction band and a p-type valence band. However in HgTe for thick enough samples (thicker than 6.3 nm) the band structure is inverted so the p bands rise above the s bands caused by the SOI. König *et al.* measured the resistance of samples thin enough where SOI was not able to cause the band inversion and they were highly resistive. For samples thicker than 6.3 nm where band inversion occured, resistance along the sample descreased dramatically caused by the quantum spin insulator state. This experiment proved the existence of the quantum spin insulator, where the conductance is entirely due to the edge states crossing the energy gap while the bulk of the sample is insulating or in this case semi-conducting. The strong SOI band inversion is then a requirement for the quantum spin insulator in HgTe, also known as a 2D topological insulator.

The transition from 2D to 3D topological insulator no longer just causes edge states but entire surface states, where T is again conserved. There are two classes of 3D topological insulators, strong and weak. A weak 3D topological insulator is caused by stacking layers of 2D topological insulator to cause a surface state. However for the case of strong topological insulators unique surface states are

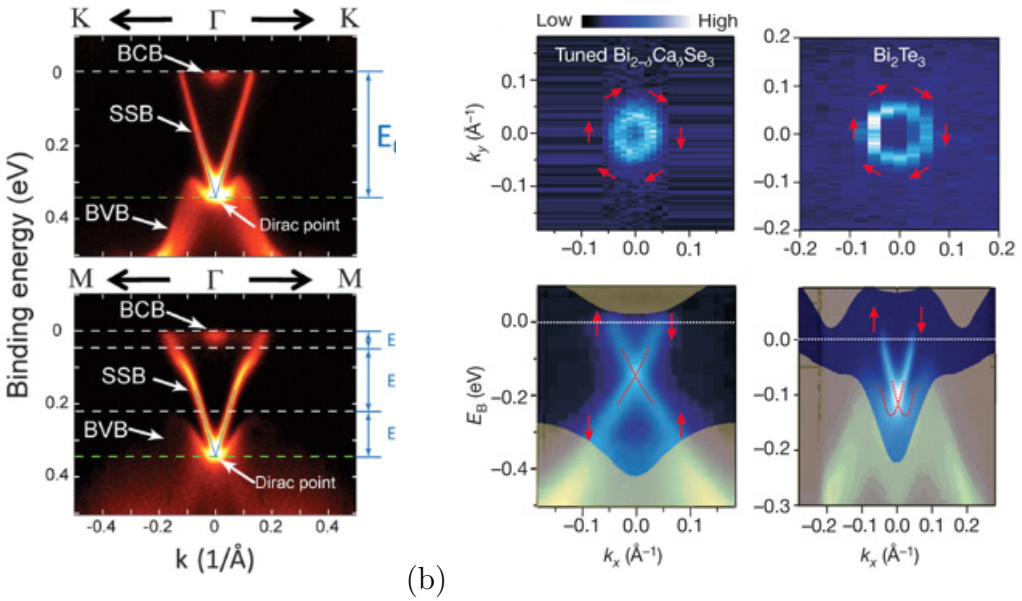

Figure 1.3: (a) *The ARPES results of Chen et al. [8] showing the Dirac band at the* Γ *point along both the* K - Γ *and* M - Γ *directions respectively, in the Brillouin zone of* Bi_2Te_3 (b) *ARPES measurements on* Bi_2Te_3 *and* $Bi_{2-\delta}Ca_\delta Se_3$ *carried out by Hsieh et al. [9] around* Γ *where electron spin has also now been resolved indicated by the red arrows*

possible, even in bulk samples, caused by an electronic band structure with the shape of the Dirac cone just as in graphene [4]. The bulk of the material is again insulating and the Dirac cone shape bands cross the bandgap to produce metal surface states just as the edge states did. Around the Dirac cone there is spin-momentum locking preventing back scattering and hence T is preserved just as in the 2D case.

The original materials predicted to be 3D topological insulator materials were actually widely studied semiconductors such as bismuth based tellurides and selenides. These materials exhibit a strong SOI and inverted band structures at certain points in the Brillouin zone, such as the Γ point in Bi_2Te_3 and Bi_2Se_3. The main problem in measuring the conductivity of such states is the separation between the surface and bulk. While they are semiconductors the bulk carrier concentration is high and not easily lowered. However the surface states are detectable using angle resolved photoemission spectroscopy (ARPES) which can separate bulk and surface state bandstructures with great effect.

ARPES experiments carried out on Bi_2Te_3 by Chen *et al.* [8] measured the

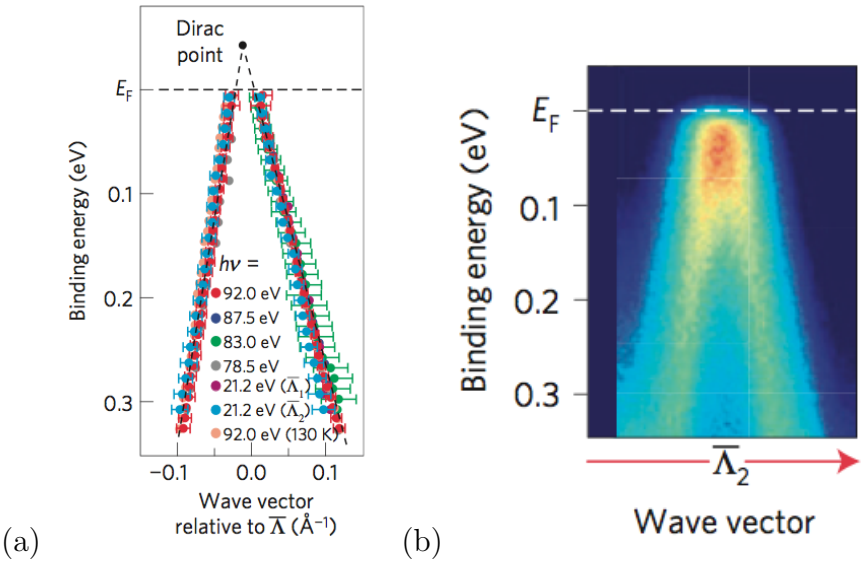

Figure 1.4: (a) *The ARPES results of Tanaka et al. [10] on SnTe using a range of incident energies a Dirac band dispersion is plotted out just away from the X point labelled* $\overline{\Lambda}$ (b) *The band dispersion at* $\overline{\Lambda}$ *using an energy of 21.2eV near the Fermi energy*

Dirac band crossing the bandgap at Γ, where the band inversion occured, as shown in Figure 1.3 (a). They were able to clearly separate the bulk valence band (BVB) and conduction band (BCB) from the surface state band (SSB). D. Hsieh *et al.* [9] also carried out ARPES on Bi_2Te_3 and Ca doped Bi_2Se_3 to tune the Fermi energy in the band gap. Their results are shown in Figure 1.4 (b) for both materials. D. Hsieh *et al.* were able to resolve the spin in their experiment indicated by the red arrows, showing the spin-momentum locking protected by T.

In 2D and 3D topological insulators it is the overall conservation and protection of T that gives rise to the edge and surface states. However there are also now examples of what are known as crystalline topological insulators where space group symmetries of the crystal structure replace the role of T. T. Hsieh *et al.* [11] considered the fcc semiconductor material SnTe. Using the plane of any two L points in the [1,1,1] direction along with the zone centre Γ point to form a momentum space mirror plane which is invariant about the (1,1,0) axis, T. Hsieh *et al.* [11] then considered eigenstates reflected in this mirror plane. The reflection lead to what are called mirror Chern numbers that cause gapless modes when projected onto other symmetry lines. For the plane of two L points

and the Γ point a projection onto the symmetry line ΓX, where X is along the [1,0,0] direction, cause two gapless Dirac cones along the $X - \Gamma - X$ line. At applied magnetic fields T. Hsieh *et al.* predict the surface states to be quantum Hall like.

In SnTe a band inversion occurs at the L point when compared to a very similiar fcc material PbTe. T. Hsieh *et al.* [11] predicted that SnTe will then be a crystalline topological insulator by reflection about the $L - \Gamma - L$ plane while PbTe will not, because of this inversion. Shortly after the prediction, Tanaka *et al.* [10] carried out an ARPES experiment and found Dirac like bands just below the Fermi energy in SnTe just slightly away from the X point, shown in Figure 1.4. ARPES was also carried out on PbTe which showed no such bands. In the material $Pb_{1-x}Sn_xTe$ going from $x = 0$ to $x = 1$ the gap closes (at $x \approx 0.37$) and reopens again inverted as shall be discussed in section 1.2. Therefore $Pb_{1-x}Sn_xTe$ will also be a crystalline topological insulator for the correct values of x . At a value of x= 0.4 and 0.6 Xu *et al.* [12] measured Dirac like bands in $Pb_{1-x}Sn_xTe$ using ARPES and were able to resolve the spin to show the spin-momentum locking still existed in these surface states, now protected by the crystal symmetry rather than T.

The properties of SnTe shall now be discussed further. Particular focus will be on a structural transition which removes a centre of symmetry and hence would have a destructive effect on the mirror symmetry protected topological state. However as T. Hsieh *et al.* [11] point out some surface states are still possible even in the rhombohedral phase. It's high carrier concentration is also discussed, which makes the surface states difficult to detect in transport measurements.

1.2 Properties of SnTe

1.2.1 Introduction and Bandstructure

As grown SnTe has the fcc rocksalt structure with space group $Fm\overline{3}m$ at 300 K. However the solid crystals are found to always lay off stoichiometry in the Te rich side, giving a correct formula of $Sn_{1-x}Te$. This excess of Te is accommodated in the lattice by the presence of Sn vacancies. These vacancies give rise to a high concentration of hole type carriers, n, that do not freeze out at any temperature. Brebrick [13] investigated the liquidus line of SnTe for several compositions,

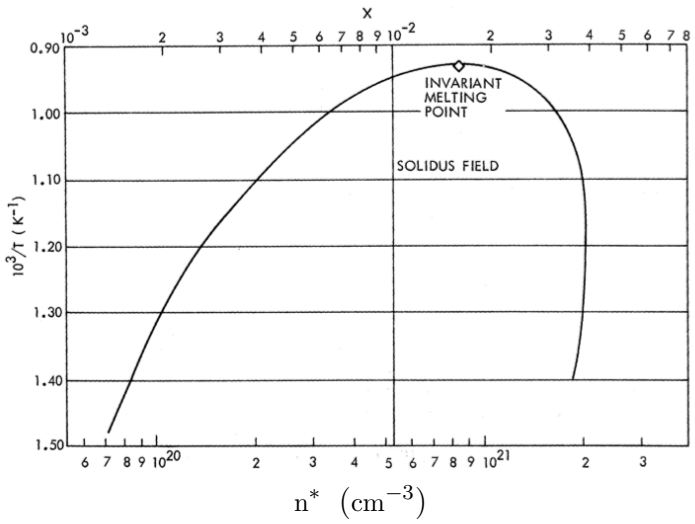

Figure 1.5: *The phase diagram of SnTe taken from Savage et al. [14]. The top axis shows the value of tin deficiency while the bottom shows the corresponding nominal carrier concentration, where $n = rn^*$. The invariant meting point of* 806 °C *is shown along with the line representing the solidification denoted the solidus field. The curve to the left of solidus field represents the solubility limit of Sn.*

finding a maximum melting temperature of 806 °C for $x = 0.01$. The grown crystals were also saturated in enviroments of Sn and Te at high temperatures near the melting point. Using this saturation method Brebrick [13] was able to successfully vary the carrier concentration by varying x. A phase diagram for SnTe from the paper by Savage *et al.* [14] is shown in Figure 1.5. The relation between this nominal carrier concentration n^* of Savage *et al.* [14] in Figure 1.5 and the actual value is simply a scaling constant, r, where $n = rn^*$. Savage *et al.* [14] found a value of $r = 0.6$. The invariant melting point of 806 °C is shown along with a line for the solidification which Savage *et al.* [14] denote the solidus field. The curve boundary to the left of this solidifcation line represents the saturation limit of Sn.

The value of carrier concentration has a profound effect on many of the properties of SnTe. Bis and Dixon [15] measured the variation of lattice parameters with respect to n. For the highest values of $n = 9.5 \times 10^{20}$ cm^{-3} a lattice constant of $a = b = c = 6.312$ Å was measured, which increased linearly to 6.327 Å at $n = 0.2 \times 10^{20}$cm^{-3}, giving the relationship

$$a = -1.7 \times 10^{-23} n + 6.327. \tag{1.24}$$

Several band structure calculations have been carried out for SnTe, by various groups. All suggest it is a small gap semi-conductor with the narrowest gap occuring at the L point of ≈ 0.3 eV [16, 17, 18, 19]. Throughout the rest of the Brillouin zone a much larger gap of 2 eV exists. The very similar material PbTe and alloy $Pb_{1-x}Sn_xTe$ are also widely studied small gap semiconductors with the rocksalt structure and often used for comparison with SnTe, as already mentioned. The character of the bands at the L point is a particularly interesting point of the band structure in these materials. Dimmock *et al.* [20] investigated the bandgap in $Pb_{1-x}Sn_xTe$ using photoluminescence spectroscopy. Their measured results were then compared with those of previous experiments. Dimmock *et al.* concluded upon going from PbTe to SnTe a band inversion at the L point had taken place. Tung and Cohen [16] carried out band structure calculations on SnTe and PbTe, which include spin-orbit coupling. Their theoretical work also show a change in ordering of the bands at the L-point going from PbTe to SnTe. The valence band maximum is denoted L_6^+ in PbTe while L_6^- in SnTe, and vice versa for the conduction bands. The band L_6^+ is then mainly contributed by Pb/Sn s electrons plus Te p electrons i.e. is a s-type band. Then L_6^- is mainly Pb/Sn p electrons plus Te s electrons hence is a p-type band.

So in going from PbTe to SnTe the L_6^+ valence band rises above the bandgap to become the conduction band in SnTe. At the same time the L_6^- moves down to become the valence band and the band inversion is complete. Hence at some value of x in the alloy $Pb_{1-x}Sn_xTe$ the bandgap should close. Dimmock *et al.* found at a value of x≈ 0.37, the bandgap becomes zero [20].

1.2.2 Soft Phonon Structural Phase Transition

Upon cooling SnTe is known to undergo a structural transition from rocksalt to a low temperature distorted rhombohedral phase. The transition is brought about by the lattice being unstable due to its dynamics. A detailed introduction to the field of lattice dynamics is given by the text of Dove [21]. The main points needed to understand the situation in SnTe are summarised here.

Classically one can imagine chains of atoms in a solid being connected by springs. Assuming the displacement associated with the atoms in these chains is small compared to the lattice constants, their energy can be expanded in a Taylor series. Considering only the quadratic term of the expansion, known as

the harmonic approximation, the energy of the lattice is then the same as a set of harmonic oscillators. The introduction of quantum mechanics allows not only a description of the vibrations as a wave but also as particles called phonons. In the case of a diatomic chain of atoms with masses M and m an equation of motion of the form

$$\begin{pmatrix} E \\ e \end{pmatrix} \omega_k^2 = \mathbf{D}(\mathbf{k}) \begin{pmatrix} E \\ e \end{pmatrix} \tag{1.25}$$

is considered. Here E and e are the amplitudes of displacement of the atoms with masses M and m respectively, while ω_k is the frequency associated with the displacement in momentum space [21]. The matrix $\mathbf{D}(\mathbf{k})$ is known as the dynamical matrix and is Hermitian, meaning its eigenvalues are real. For a particular phonon branch, n, the values of ω_k^2 are then the eigenvalues while the energies of displacement are the eigenvectors. All the information that determines both the frequencies and displacements is therefore contained within the dynamical matrix. Hence when calculating phonon dispersion curves one would be concerned with the nature of $\mathbf{D}(\mathbf{k})$.

However ω_k^2 contains no dependence on temperature and while they are real eigenvalues they can also be negative. Temperature dependence is found by inclusion of higher order terms of the Taylor expansion known as anharmonic terms. Their main effect is a change in frequencies from the harmonic values, ω_k^2, to renormalised frequencies $\tilde{\omega}^2$ with the anharmonic interactions in what is known as the pseudo-harmonic approximation. Temperature dependence can be included via the anharmonic terms and $\tilde{\omega}^2$ is expressed as

$$\tilde{\omega}^2 = \omega_0^2 + \alpha T \tag{1.26}$$

where ω_0^2 is the harmonic frequency, T is temperature and α a constant that is generally positive.

If at 0 K the crystal has a harmonic frequency that is negative the lattice is unstable. The lattice will then be distorted to a phase of lower symmetry. This distortion corresponds to the higher symmetry phase with a frozen in co-ordinate at wavevector $\mathbf{k}$ belonging to the negative eigenvalue. Upon heating the anharmonic term increases until $\tilde{\omega}^2$ becomes positive and a transition to the high

symmetry phase occurs, at a temperature

$$T_c = \frac{-\omega_0^2}{\alpha} \tag{1.27}$$

Alternatively one can think of the transition on cooling. Upon cooling the frequency of the mode decreases, which is called softening, and T_c occurs for the point at which the frequency becomes zero. The **k** point at which the softening takes place is generally a point of high symmetry within the Brillouin zone.

The loss of a centre of symmtery associated with this phase transition below T_c, causes a dipole moment to occur within the unit cell. This is known as a ferroelectric transition. Alignment of the dipoles will then give a very measurable dielectric polarisation, P, in the crystal, analogous to the magnetic moments in a ferromagnet.

The macroscopic theory usually used in describing ferroelectrics is the Landau general theory of phase transitions, called Landau-Devonshire theory (Devonshire independently developed it explicitly for ferroelectrics). Chandra and Littlewood [22] give a very good introduction to the application of Landau theory to ferroelectrics. In basic Landau-Devonshire theory the Helmholtz free energy is expanded in a power series of the order parameter of the system. In the case of ferroelectrics the order parameter is the polarisation, P, and the free energy F_P is

$$F_P = \frac{1}{2}aP^2 + \frac{1}{4}bP^4 + \frac{1}{6}cP^6 - EP \tag{1.28}$$

where E is an electric field and a, b and c are coefficients. The thermal equilibrium configuration is found by determining the minimum of F_P. The linear dielectric susceptibility, χ, is defined as

$$\chi = \frac{P}{E} = \frac{1}{a} \tag{1.29}$$

where for $T \approx T_c$

$$a = a_c(T - T_c) \tag{1.30}$$

which captures the Curie-Weiss behaviour seen in ferroelectrics above T_c. The dielectric stiffness, κ is defined as

$$\kappa = \frac{1}{\chi} = a_c(T - T_c). \tag{1.31}$$

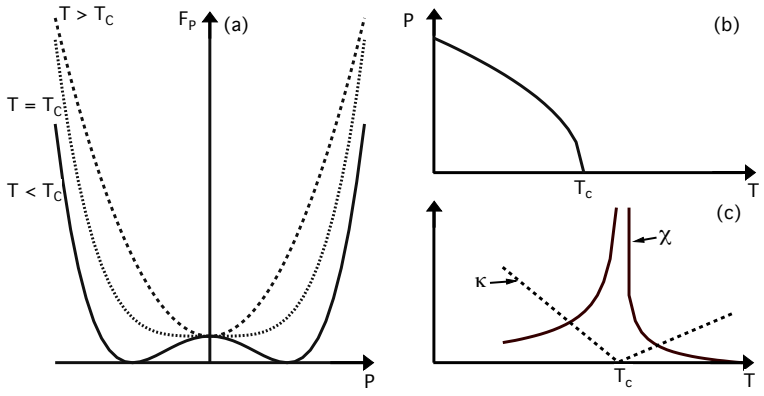

Figure 1.6: *(a) The shape of the free energy F_P against polarisation P for a 2^{nd} order phase transition. Above T_c there is a single minimum at the origin. Cooling through T_c a continuous transformation to minima at finite polarisation occurs. (b) Polarisation as a function of temperature growing below T_c. (c) The dielectric susceptibilty χ showing divergence at T_c. The dielectric stiffness κ is also plotted with a gradient ratio of 2:1 either side of T_c*

For a, b and c all positive the free energy has a minima at the origin. However as T is lowered below T_c, a becomes negative while b and c remain positive. F_P then evolves continuously to have a minimum at finite polarisation as shown in Figure 1.6 (a). This is known as a 2^{nd} order phase transition. The polarisation is given by

$$P_0 = \frac{a_c}{b}(T_c - T)^{\frac{1}{2}} \tag{1.32}$$

for temperatures below T_c as shown in Figure 1.6 (b). The dielectric stiffness below T_c determined for a 2^{nd} order transition is then

$$\kappa = \frac{1}{\chi} = 2a_0(T - T_c). \tag{1.33}$$

as shown by the slope of the lines in Figure 1.6 (c).

If we are considering a soft phonon above T_c the lattice remains in its high symmetry state with zero polarisation. Upon cooling through T_c a displacive transition occurs with a frozen in co-ordinate. A centre of symmetry is lost and polarisation occurs. The size of the polarisation is proportional to the size of the displacement and the frequency of the phonon varies as

$$\omega^2 \propto \frac{1}{\chi} \propto \kappa \tag{1.34}$$

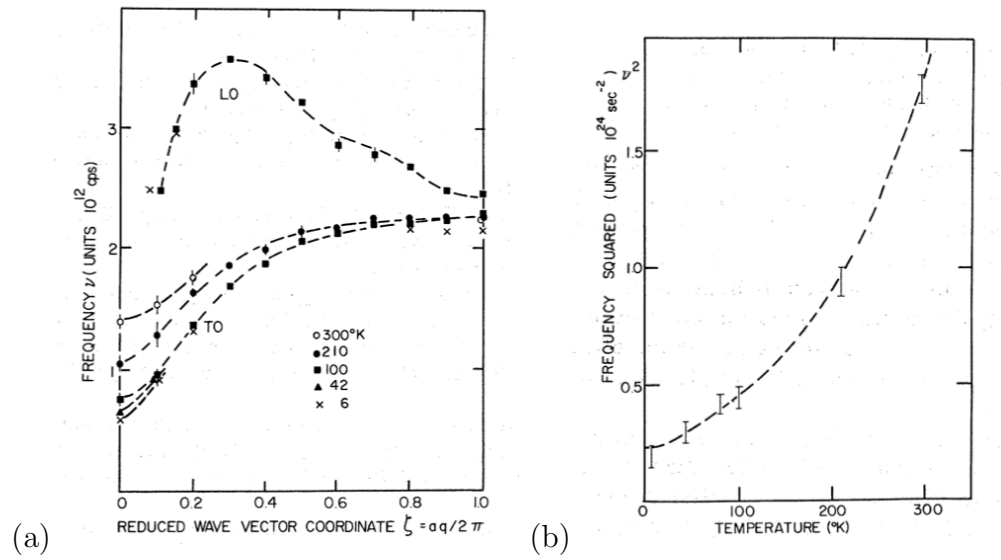

(a) (b)

Figure 1.7: *The inelastic neutron results of Pawley et al. [25]. (a) Shows the temperature dependence of the transverse optic (TO) phonon. A softening is seen on cooling. The longitudinal optic (LO) is also shown. (b) A graph of TO phonon frequency squared at the zone centre verus temperature*

The frequency of the soft phonon squared will then decrease to zero linearly at T_c and recover in the distorted phase below T_c linearly with twice the gradient. This is the case for 2^{nd} order transitions. Most well studied ferroelectric materials are perovskites such as $SrTiO_3$ or $PbTiO_3$. An example of a 2^{nd} order phase transition from a soft transverse acoustic phonon at the zone edge is seen in $SrTiO_3$ [23]. Although the frequency of the phonon does not go complelety to zero the linear recovery is still indictive of a 2^{nd} order transition. Many ferroelectric transitions turn out to be more 1^{st} order in nature, where the polarisation increase is discontinuous at T_c. The soft phonon decreases linearly to a finite frequency such as in $PbTiO_3$ at the zone centre [24]. Upon recovery of the phonon there will then be a discontinuous jump in the frequency squared. Often first order transitions such as this are caused by for example coupling to crystal strains or disorder which were not considered in the foregone discussion.

Phonon dispersion curves can be measured in experiments in which the lattice vibrations exchange energy with an external probe. The most revealing probes are neutron beams where one can view the energy lost or gained by a neutron while interacting with the crystal as being due to the emission or absorption of phonons. Measuring such energy transfers gives direct information on the phonon

spectrum. The probe used can also be X-rays. A discussion of inelastic neutron and X-ray scattering to measure phonon dispersion curves is given in Chapter 3.

Pawley *et al.* [25] measured the phonon dispersion curves in SnTe using inelastic neutron scattering. Their results are shown in Figure 1.7. The transverse optic branch is strongly temperature-dependent, however never reaches zero, as shown in Figure 1.7 (a). This lead Pawley *et al.* [25] to suggest that their sample was approaching a ferroelectric transition but remains cubic throughout. The variation of the frequency squared at the zone centre is shown in Figure 1.7 (b) as a function of temperature. Alperin *et al.* [26] measured the TO-phonon in PbTe from 293 K to 4 K using inelastic scattering and also saw some softening. However the softening was much less pronounced.

Cowley, Darby and Pawley [27] measured the phonon dispersion curves along all the high symmetry directions in cubic SnTe at 100°C and fitted them to various models. Their fits to the experimental data showed that the frequency of the soft TO phonon was particularly sensitive to electron-phonon Umklapp processes. This would suggest a dependence of lattice stability on the carrier concentration.

Muldawer [28] carried out powder X-ray diffraction on samples with various carrier concentrations. In samples of sufficiently low n, Muldawer saw splittling in diffraction peaks consistent with a transformation to a rhombohedral phase. The transition corresponds to the cubic phase being distorted along the (111) direction leading to an elongation of the unit cell. The angle change associated with this shear is estimated to be from 90° in the cubic to 89.895° in the rhombohedral phases respectively [28]. The distortion angle increases as a function of temperature below T_c as measured by Muldawer. However for samples of significantly high values of n no peak splitting was observed suggesting no transition had taken place. It was most likely the case in the sample measured by Pawley *et al.*, n was large enough such that it never passed through the distortion.

Other indications of a phase transition have been seen in the Raman scattering experiments of Brillson *et al.* [31]. The phase transition caused a change in the Raman selection rules to allow phonon scattering in the rhombohedral phase that was forbidden in the cubic phase. Iizumi *et al.* [30] carried out neutron diffraction where a change in Bragg reflection intensity indicated a structural transition had taken place caused by the 2 fcc sublattices shifting to the rhombohedral

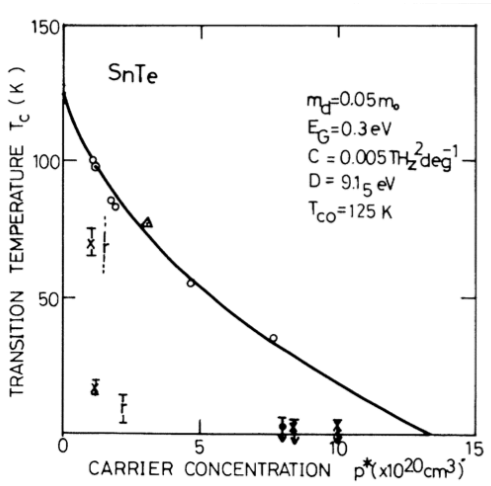

Figure 1.8: *The resistivity results of Kobayashi et al. [29] as open cirlces showing the transition temperature T_c verus carrier concentration. Also included are the neutron bragg reflection results of Iizumi et al. [30] as circles with dots and the inelastic neutron data of Pawley et al. [25] as the solid circle. The X-ray results of Muldawer [28] are represented by the crosses and the Raman results of Brillson et al. [31] the r. The solid curve represents the results from the theoretical model using the TO-phonon-electron interaction.*

distortion. Iizumi *et al.* [30] estimated the shift of the two sublattices to be ≈ 50 pm.

As well as the evidence seen in scattering techniques an anomalous increase in resistivity also exists at T_c [32, 29]. Kobayashi *et al.* [29] measured this anomaly as a function of carrier concentration which showed the same features as previous experiments. For higher carrier concentrations the value of T_c decreases until no transition is detected at all. The results of Kobayashi *et al.* [29] are shown in Figure 1.8 which includes points from the previous experiments. To explain this carrier concentration dependence of T_c, Kobayashi *et al.* [29] employed an electron-TO-phonon interaction model. By renormalising the TO phonon frequency with an electron-TO-phonon interaction a carrier concentration dependence was calculated and is shown as the solid curve in Figure 1.8. From the results of Kobayashi *et al.* [29] the TO phonon frequency is reduced by the electron-TO-phonon interaction making the lattice unstable. At high enough carrier concentrations this interactions becomes smaller reducing T_c. Katayama and Mills [33] carried out a very thorough theoretical investigation of the resistivity anomaly in SnTe. They also concluded the anomalous increase in

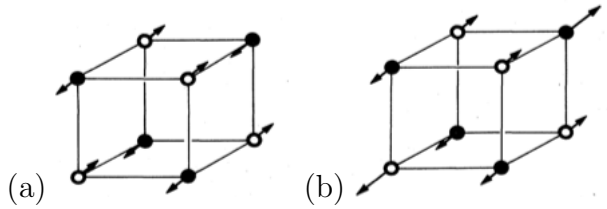

Figure 1.9: *A schematic of the structural distortion in SnTe from the paper of Rabe and Joannopoulos [17]. (a) The two fcc sublattices displace indicated by the equal sized black arrows. (b) The associated rhombohedral shear angle from* 60° *to* $\approx 59.878°$ *along the (1,1,1) indicated by the larger black arrows.*

the resistivity was caused by increased TO-phonon scattering associated with the structural transition. They also suggested a small contribution from scattering with the transverse acoustic (TA) phonon.

Heat is conducted in solids not only via electrons but also the phonons. A measurement of the specific heat, C, will then provide information of the samples phonon dispersion and anharmonicity as well as phonon-softening, phonon-phonon interactions or phase transitions. In 2^{nd} order transitions a discontinuity in C is evident while the latent heat of 1^{st} order transitions makes them identifiable. Bevolo *et al.* [34] measured the specific heat of SnTe from 0.9 to 60 K on a sample with $n = 8 \times 10^{20}\text{cm}^{-3}$, which would suggest a $T_c \approx 25K$ from the results of Kobayashi *et al.*. No anomalies corresponding to phonon softening or a phase transition were detected by Bevolo *et al.*. Hatta and Kobayashi [35] measured the heat capacity in SnTe in a sample with $n = 1.8 \times 10^{20}\text{cm}^{-3}$. An anomaly of 89 K was evident in the resistivity while a jump in specifc heat was seen between 89 and 92 K strongly suggestive of a 2^{nd} order transition.

The structural distortion then happens by two symmetry reductions as discussed by Salje *et al.* [36]. The cubic phase reduces to the rhombohedral phase with angle $\approx 59.878°$ via an elastic strain along the cube diagonal. This would not destroy the centre of inversion, however the second reduction is the displacement of the two fcc sublattices by ≈ 50 pm giving the polar displacement, destroying the centre of inversion. This would then make the transition ferroelectric. The 2 reductions are shown in Figure 1.9 taken from the paper by Rabe and Joannopoulos [17]. When describing the ferroelectric transition then one must also consider the free energy associated with the elastic strain as well as the polarisation. These strain-dependent terms can also be expanded in a Landau

theory approach, as explained by Chandra and Littlewood [22], of the form

$$F_s = \frac{1}{2}Ks^2 + dsP^2 + ... \tag{1.35}$$

where s is a component of the strain field. The quadratic term in the expansion is equal to Hooke's law, with an elastic energy stored in a solid quadratically dependent on distortion, then K is one of the elastic constants. The second linear term is a coupling between the strain and the polarisation. Consequences of such behaviour are the formation of domains and an explicit temperature dependence of the one or more elastic constants near T_c. Salje *et al.* [36] discuss the structural distortion in SnTe in terms of a Landau expansion of the free energy both in polarisation and strain.

In particular they point out the C_{44} elastic constant should show a temperature dependence near T_c for a diagonal distortion (elastic constants are discussed more in Chapter 3). Salje *et al.* [36] carried out a measurement of the C_{44} elastic constant using resonant ultrasound spectroscopy. Their sample had $n = 3.9 \times 10^{19}\text{cm}^{-3}$ and an anomaly in the resistivity at 98 K which they found difficult to reproduce on heating and cooling. Specific heat measurements showed no anomaly at all corresponding to a transition. The C_{44} elastic constant was found to have a very small temperature dependence and increased for decreasing temperature. However the value of C_{44} showed a slight kink at ≈ 100 K possibly corresponding to T_c. This behaviour is rather unusual and could point towards a lack of domain formation. Salje *et al.* [36] also attempted ferroelectric switching in SnTe by applying electric fields. The high carrier concentrations however short circuited any applied field and no ferroelectricity could be detected. So while the transition would seem to be ferroelectric there is limited experimental evidence it actually is, other than it goes through a phase transition.

The carrier concentration dependence of the properties in SnTe is a particularly interesting point, hence knowledge of the Fermi surface is particularly useful. One method of Fermi surface determination in SnTe was measurements of quantum oscillations in magnetoresistance known as Shubnikov de Haas (SdH) oscillations by Burke *et al.* [37] and in magnetisation known as de Haas van Alphen (dHvA) oscillations by Savage *et al.* [14]. The text of Shoenberg [38] contains all the information needed to describe quantum oscillations. A brief summary of the points required to understand the situation in SnTe that shall

be used further in Chapters 2 and 4 are given in the following section.

1.2.3 Fermi Surface of SnTe via Quantum Oscillations

As already mentioned when a current-carrying conductor is placed in a magnetic field the charge carriers are deflected via the Lorentz force to one side of the conductor in what is known as the normal Hall effect. The carriers with electron charge e in an applied field B move with a cyclotron motion ω_c

$$\omega_c = \frac{eB}{m^*} \tag{1.36}$$

where m^* is the effective mass. To understand oscillatory phenonmena such as the SdH and dHvA effects one must introduce quantum mechanics leading to Landau tubes and the Onsager relation as discussed in Shoenberg [38]. Quantum mechanics leads to a quantisation of the orbital motion of the charged particles in high fields of the form

$$E = (n + \frac{1}{2})\hbar\omega_c + \frac{\hbar^2 k_z^2}{2m^*} \tag{1.37}$$

for a field $\mathbf{B}$ applied along z. Allowed orbits in the x-y plane perpendicular to the magnetic field are now on a series of constant energy surfaces in $\mathbf{k}$ space known as Landau tubes. The electrons moving parallel to the field in z will then remain unaffected in the above relation.

As the field increases the Landau tubes pass through the Fermi surface leading to oscillations in the density of states at the Fermi level. Such oscillations are then detectable in any property of the solid dependent on the density of states such as magnetoresistance, the normal Hall effect or magnetisation. The period of the oscillation, T, has been described by Onsager for an applied field B

$$T = \Delta\frac{1}{B} = \frac{2\pi e}{\hbar}\frac{1}{S} \tag{1.38}$$

where S is the extremal cross-section of the Fermi surface normal to the direction of the field. The oscillatory frequency F is given by

$$F = \frac{\hbar}{2\pi e}S \tag{1.39}$$

at each value of S. However high fields are not the only requirement to detect quantum oscillations. Features such as finite temperature T, finite electron relaxation time τ, electron spin and sample inhomogenity can be introduced as particular examples of phase smearing of the oscillations. Such phase smearing acts to reduce the amplitude of the oscillations and can be described in what is known as the Lifshitz-Kosevich formula. The formula is written as

$$A \propto B^{\frac{1}{2}} \left| \frac{\partial^2 S}{\partial k_z^2} \right|^{-\frac{1}{2}} R_T R_D R_S \tag{1.40}$$

where A is the amplitude of the oscillations. $\left|\frac{\partial^2 S}{\partial k_z^2}\right|$ is small for cylindrical Fermi surfaces giving large oscillations and large for flatter Fermi surfaces giving small oscillations. The factor R_T, known as the temperature damping factor, is caused by the electrons being thermally excited to higher Landau levels. It is described by the formula

$$R_T = \frac{\alpha m^* T/B}{\sinh(\alpha m^* T/B)} \tag{1.41}$$

where

$$\alpha = \frac{2\pi^2 k_B}{e\hbar} \approx 14.69\ \mathrm{T/K} \tag{1.42}$$

and is the only reduction factor involving temperature. Using this temperature dependence one can accurately calculate the effective mass of carriers as shall be discussed further in Chapter 2. Since real crystals include a lot of scattering centres such as impurities or lattice defects, the orbiting electrons are scattered by these and lose phase coherrence. This scattering effectively broadens the Landau levels according to the uncertainty principle and is described by the Dingle damping factor, R_D given by

$$R_D = \exp(-\alpha m^* T_D/B) \tag{1.43}$$

where T_D is the Dingle temperature, given by

$$T_D = \frac{\hbar}{2\pi k_B} \frac{1}{\tau} \tag{1.44}$$

dependent on the scattering rate τ. The Dingle factor is only dependent on τ and one can deduce the Dingle temperature by a change in oscillation amplitude

as a function of field to give the scattering rate, τ. Hence very pure crystals are a requirement to see oscillatory phenomenon. In magnetic fields, the Landau levels are split into spin-up and spin-down levels known as Zeeman splitting. The energy of such splittings is determined by $g\mu_B sB$, where g is known as the Lande g-factor, μ_B the Bohr magneton, and s the spin. Each spin state leads to oscillations with the same frequency but phase shifted leading to an overall reduction in amplitude. The reduction is governed by the field independent spin reduction factor R_s, where

$$R_s = \cos(\pi g r m_s/2) \tag{1.45}$$

and m_s is the spin mass from electron-electron interactions, r is the harmonic number and g the Lande g-factor which can be determined from R_s. For the case of diamagnetic SnTe in the results reported in chapters 2 and 4 we are mostly interested in R_T and R_D since they will be the main contribution to phase smearing and amplitude reduction.

Previous measurements carried out by Burke *et al.* [37] measured SdH oscillations in a SnTe sample with $n = 5 \times 10^{20}\text{cm}^{-3}$ up to 15.5 T which consisted of 2 frequencies possibly from 2 hole pockets. However for $n = 2.3 \times 10^{20}\text{cm}^{-3}$ 3 frequencies were detected that most likely belonged to the same pocket. The lowest frequencies were along the (111) direction leading Burke *etal.* [37]to suggest the Fermi surface consisted of ellipsoids elongated along this direction.

Savage *et al.* [14] carried out a much more thorough investigation using the dHvA effect on the diamagnetism in SnTe on a range of samples with various values of n. With $n \leq 3.5 \times 10^{20}\text{cm}^{-3}$ the data had from 3-5 frequencies describing one pocket at the L point of the Brillouin zone as shown in Figure 1.10 (a) for $n = 3.5 \times 10^{20}\text{cm}^{-3}$ consisting of 4 frequencies. With $n \geq 6.1 \times 10^{20}\text{cm}^{-3}$ only a single frequency was then detected for the single pocket at L, however a second pocket was also detected as shown in Figure 1.10 (b) for $n = 8.0 \times 10^{20}\text{cm}^{-3}$. The effective mass and Dingle temperature were calculated for the sample with high $n = 8.0 \times 10^{20}\text{cm}^{-3}$. For the 1^{st} pocket was $m^* = 0.125 \pm 0.012$ and $T_D = 21.6 \pm 2K$ while the second pocket had $m^* = 0.094 \pm 0.009$ and $T_D = 17.3 \pm 1.7K$. Savage *et al.* [14]were unable to give an explanation to as why the first pocket was made up of 3-5 frequencies at low n, other than a possible consequence of the structural transition or sample inhomogenity. Samples with high n however contained only

a single frequency from the pocket at the L point and may not have gone through the phase transition.

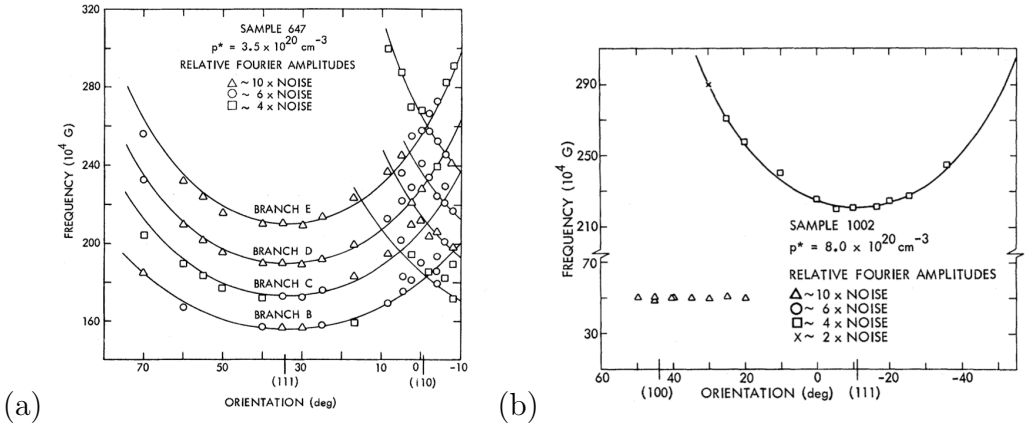

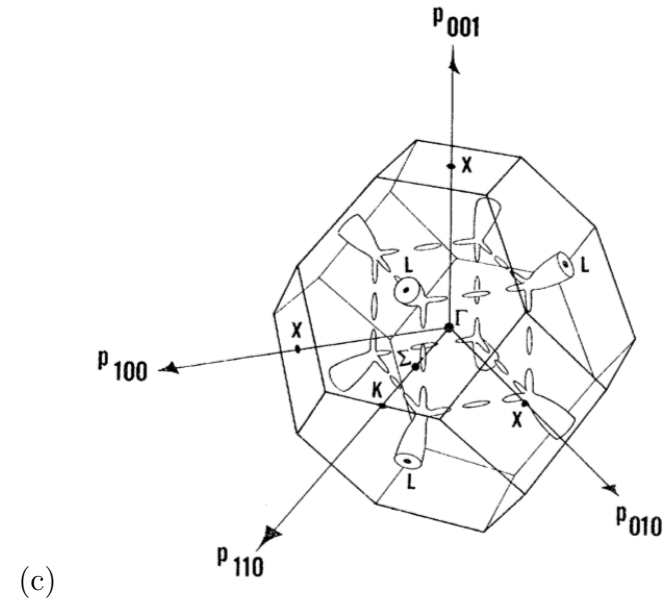

Figure 1.10: *(a) The experimental results of Savage et al. [14] on a sample with* $n \leq 3.5 \times 10^{20} cm^{-3}$ *showing 4 frequencies belonging to a hole pocket elongated along L. (b) As n is increased to* $8.0 \times 10^{20} cm^{-3}$ *the 4 frequencies now become a single frequency belonging to the pocket at the L-point. However a second smaller pocket also now occurs which is elongated along the (100) according to Allgaier and Houston [39]. The Fermi surface suggested by Allgaier and Houston [39] in SnTe with high carrier concentrations is shown as (c).*

Allgaier and Houston [39] considered the results of Savage *et al.* [14] along with previously carried out bandstructure calculations to determine a Fermi surface shown in Figure 1.10 (c). The suggested Fermi surface consists of the elongated shaped pockets at the L point as Savage *et al.*'s [14] data suggested. As the carrier concentration increases extra pockets along the (100) direction begin to form also seen by Savage *et al.* [14]. At the lower carrier concentrations these (100) pockets don't exist.

1.3 Summary

Topologically protected states known as topological insulators exist where the bulk of the material is an insulator with the surface being metallic. In practice however most known materials exhibiting such a state are semi-conductors with significant bulk carrier concentrations. SnTe in its fcc state was predicted theoretically and measured experimentally to be a new class of topological insulator protected by crystal symmetry. However SnTe also undergoes a carrier concentration dependent structural transition to a rhombohedral phase. Such a transition would result in a lowering of crystal symmetry, destroying some of the surface states. The ARPES experiment of Tanaka *et al.* [10] was carried out above the T_c of their samples when they detected the surface states.

The carrier concentration in SnTe is quite high making it almost impossible to distinguish between bulk and surface states in a transport experiment. By lowering the number of carriers one would increase T_c also making the surface states difficult to detect. In the following chapters growth and characterisation of SnTe is discussed along with a comparison of the Fermi surface to the results of Savage *et al.* [14]. The structural transition is detected using inelastic X-ray scattering to measure phonon dispersion curves and discussed. A comparison of the measured data to theoretical calculations carried out by Andreas Hermann is also included. Following on from this a high pressure study is described. The application of pressure allows the structural transition to be suppressed for a fixed carrier concentration.

Chapter 2

Tin Telluride Growth and Characterisation

This chapter discusses the various growths of SnTe and the techniques used to characterise single crystals, such as Laue X-ray diffraction and resistivity. Normal Hall effect measurements were then used to deduce the carrier concentration in single crystals. The extremal area of the Fermi surface was measured at various crystallographic positions using quantum oscillations. These results are compared to the previously published data of Savage *et al.* [14] .

2.1 Techniques

2.1.1 X-Ray Laue Diffraction

The X-ray Laue diffraction set-up in CSEC, Edinburgh, is used to determine whether samples are single crystals and their orientation. Mounted on a 3-axis (xyz) goniometer, the samples were exposed for ~ 30 minutes to a 3kW Mo tube white X-ray source operated at 35kV and 35mA. Backwards diffracted beams, then make a pattern of hyperbola shaped curves of diffraction spots, satisfying the Bragg condition, on a photographic film as shown in Figure 2.1. Spots laying on each curve belong to planes within one Brillouin zone. The software package Orient Express was used to analyse the measured diffraction patterns by choosing specific Bragg spots. Along with the crystal lattice parameters, space group and sample distance from the photographic film, Orient Express calculated a number

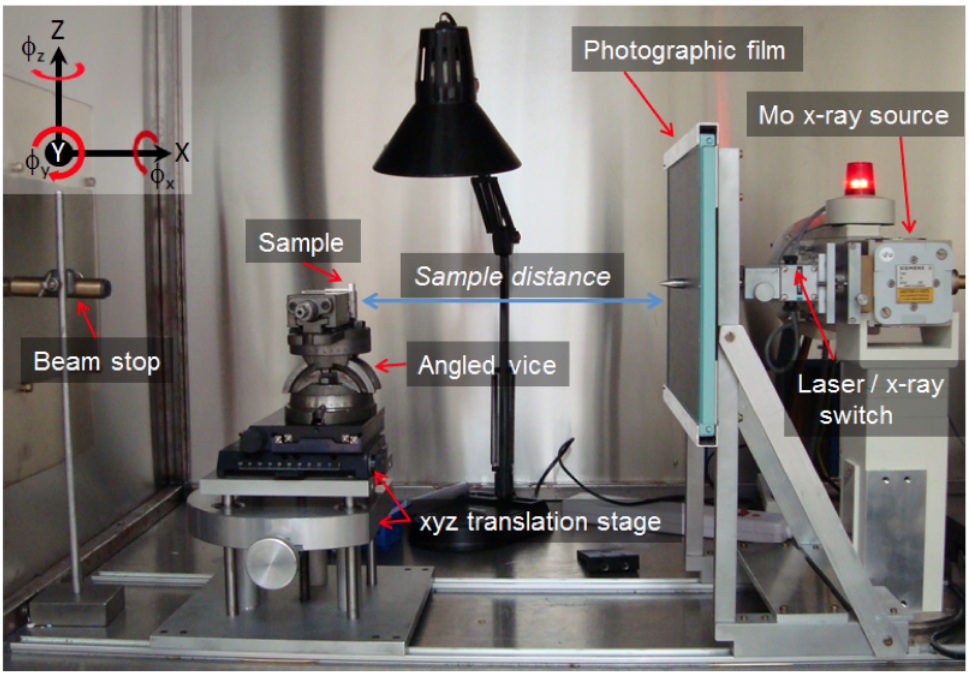

Figure 2.1: *Picture of the Laue set-up in CSEC, Edinburgh. Picture taken from ref [40]*

of suggested Laue patterns. When very close agreement between the calculated and measured patterns was made, orientation is determined. To discover whether a sample was a single crystal, many Laue images were taken along its surfaces to make sure only one grain exists.

2.1.2 Resistivity and Hall Effect Measurements

After single crystals were extracted they were cut or cleaved to the desired shape using a razor blade. For resistivity measurements the samples were cut into long thin matchstick samples to ensure an equal distribution of the current. Wider samples were required for Hall effect measurements so contacts can be attached as close to the edge as possible. Geometric factors could then be calculated accurately.

Gold wires of either 25 μm or 10 μm were then attached to the sample using spot welding. The sample was placed on a conducting platform that is connected to one terminal of a power supply and the other terminal to a sharp Tungsten needle. Under the microscope a set of micromanipulators brought the gold wire

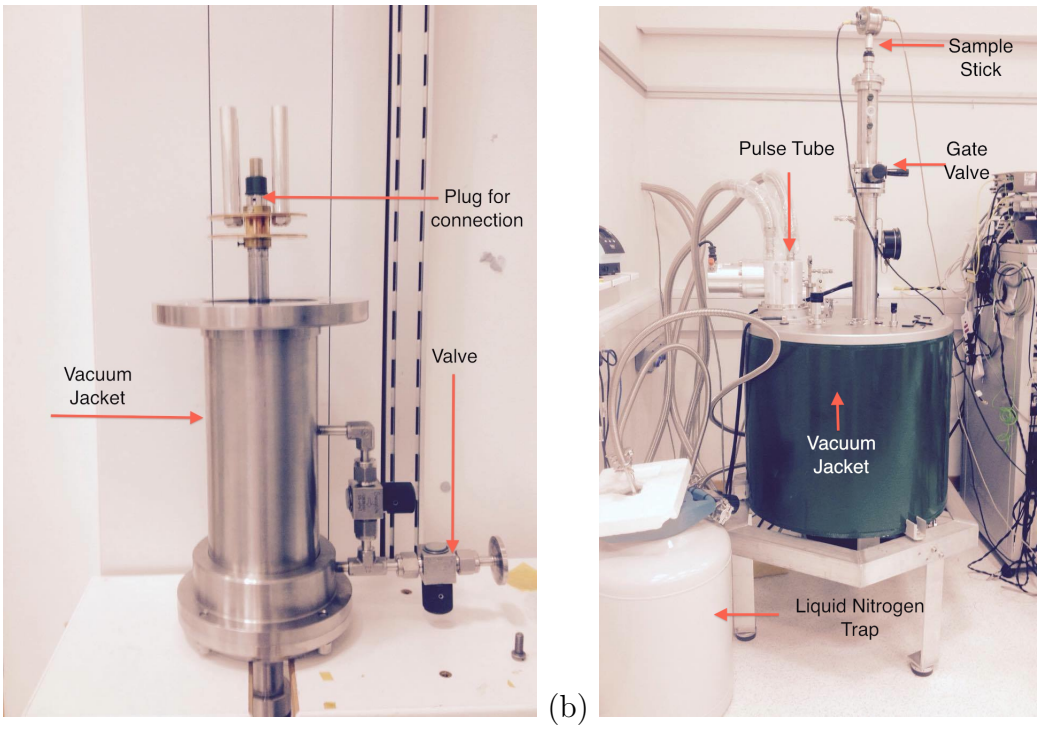

(a) (b)

Figure 2.2: *Picture of the end of the sample stick which holds the copper block containing the sample. The stick is then inserted inside the cryostat shown in (b).*

into contact with the sample. The tungsten needle was used to then press the wire onto the sample completing the electrical circuit. A current was passed through the tip of the tungsten needle for a time constant, t. Heating was then concentrated within this spot. The minimum current was selected that would attach the contacts, so as not to damage any of the surrounding material. Samples were mounted on a large oxygen-free high thermal conductivity (OFHC) copper block after spot welding. Small strips of thin (10μm) kapton foil insulated the sample electrically from the OFHC. GE varnish was used to hold the kapton and sample in place. Since the thickness is small and the contact area is large, a good thermal connection is achieved. A calibrated Cernox thermometer was added to the OFHC block, in close proximity to the sample. It was held firmly in place using a sprung copper rod, ensuring good thermal contact. The OFHC block was then attached to the end of a variable temperature insert stick shown in Figure 2.2 (a). The stick contains a vacuum jacket for evacuation and a plug to make connection with the spot welded contacts via sets of twisted pair copper wires

that passed along the probe to a Fischer plug at the end.

Resistivity measurements from 300 K to 1.8 K were carried out in the cryogen-free magnet and integrated variable temperature insert system from Cryogenic Ltd. shown in Figure 2.2 (b). The magnet cryostat uses a single two stage pulse tube cryocooler from Sumitomo Ltd.. The 2nd stage is connected directly to the magnet with a base temperature of < 4.2 K and surrounded by a large super insulated vacuum jacket. The variable temperature insert consists of a separate helium circuit that enters the cryostat through a liquid nitrogen trap that I added in the course of the thesis. After the trap the helium gas passes through a system of heat exchangers to the helium pot, through a needle valve into the base of the sample column. A gate valve at the top of the system allows entry to the sample column of the sample probe as shown in Figure 2.2 (b). The gas temperature was then varied between 300 K and 1.8 K and the pressure of the needle valve monitored. Slow rates of cooling and heating were used when measuring resistivity curves of 0.2 K per minute. This is to allow for good thermalisation of the OFCH block and sample with the exchange gas.

Current was applied to the sample and voltage measured via the Fischer plug using a SR830 Stanford research lock-in amplifier. Currents of 10 to 300 μA were achieved by passing the output voltage of the lock-in through a 10 kΩ resistor. The typical frequency used was $23-37$ Hz. Output signal was amplified through a SR554 Stanford research preamplifier giving a gain of 500. The gain of the preamplifier is fairly flat over the region of $\leq 10\,\Omega$ and ≤ 100 Hz according to the user manual. SnTe samples measured in this chapter are well within these contours, so we can safely assume a constant flat gain of 500.

The magnet is a 9 T NbTi solenoid with the field direction parallel to the insert direction. A current was applied and the calibrated voltage from the magnet supply was measured to record the field. The field at the centre of the solenoid is accurately known to within 10 G and resolution of 1 G. The field was ramped slowly at rates of 0.04 T per minute throughout all measurements using this set-up in this chapter. Both the Hall effect and magnetoresistance could be measured simultaneously using two coupled lock-in amplifiers. Corrections for the magnetoresistance of the thermometer were made for an accurate determination of temperature throughout the field ramp. All data was recorded using a program written in Labview software.

2.2 Crystal Growth

As discussed in Chapter 1 SnTe grows slightly off stoichiometry with a deficit of Sn. Hence has a large number of Sn vacancies with a correct formula of $Sn_{1-X}Te$. A phase diagram for SnTe from the paper by Savage *et al.* [14] is shown in Figure 1.5. The curve boundary to the left of the solidifcation line represents the solubility limit of Sn. While we would like to grow crystals of high quality and low carrier concentration, one must be aware of the position of the solidification line. Other authors have reported the more insulating SnTe becomes the more glassy and non crystalline it becomes [19, 36].

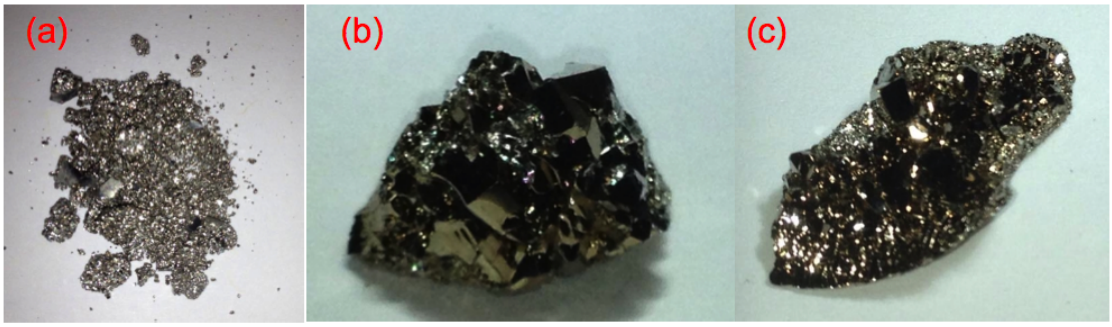

Figure 2.3: *Images of the grown material. (a) Growth number 1 quenched from* 760 °C *with equal molar weights of Sn and Te. (b) Growth number 2 quenched from* 770 °C *with equal molar weights of Sn and Te. (c) Growth number 3 quenched from* 770 °C *with molar weights of Sn and Te of the ratio 51:49.*

All growths carried out in this chapter were done with the help of Dmitry Sokolov. The first attempted growth used equal molar weights of high purity elements Sn (99.99 %) and Te (99.99 %). The Sn was etched in HCl (37 %) for over an hour to remove surface impurities, before being washed clean in an ultrasound bath of acetone. The elements were wrapped in a thin sheet of molybdenum foil to form a sealed packet and placed in a quartz tube (tantalum is not used since it forms a eutectic with Sn in the temperature ranges used). Using a turbo pump the quartz was evacuated to a pressure of 10^{-5}mbar and sealed by heating with a handtorch.

The quartz tube was set in an alumina boat and carefully placed within the centre of a tube furnace. The furnace was heated to a temperature of 850 °C over a period of 4 hours, well above the melting point. After being held at 850 °C for 3 hours the furnace was then cooled slowly to 760 °C over 48 hours. The point of

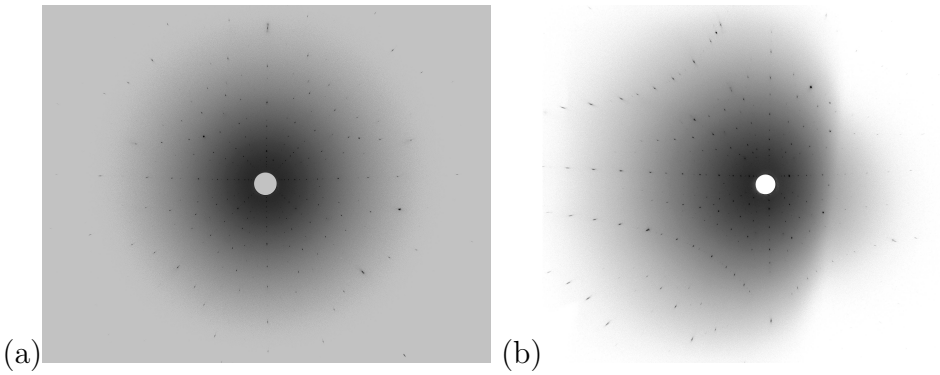

(a) (b)

Figure 2.4: *(a) A Laue image of a SnTe single crystal along the (1,0,0) direction. (b) A Laue image of the same crystal now orientated along the (1,1,0) direction.*

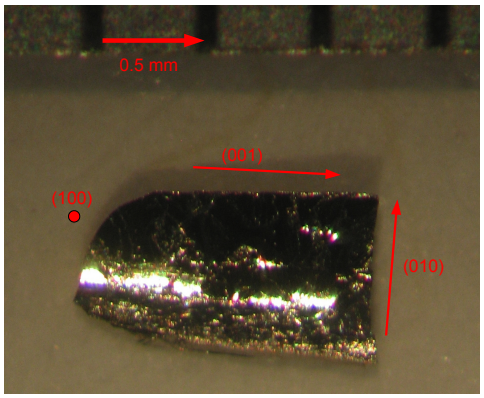

Figure 2.5: *Sample S21 after cleaving with a razor blade. The red arrow indicates the scale of 0.5 mm. The crystallographic axes are also indicated with the (1,0,0) facing into the page and the other cubic directions along the edges.*

760 °C denotes the limit of the solidification line in Figure 1.5 taken from Savage *et al.* [14]. For the next 24 hours the furnace was held at 760 °C. Following this the quartz tube was removed from the furnace and quickly quenched in a bucket of room temperature water. A picture of the grown material is shown in Figure 2.3 (a), denoted as growth 1. While it consists of many pieces of material that would suggest single crystallites, on close inspection they are very grainy and glass like. Laue diffraction was carried out on a large number of the crystals but all measured patterns indicated extremely poor crystallinity.

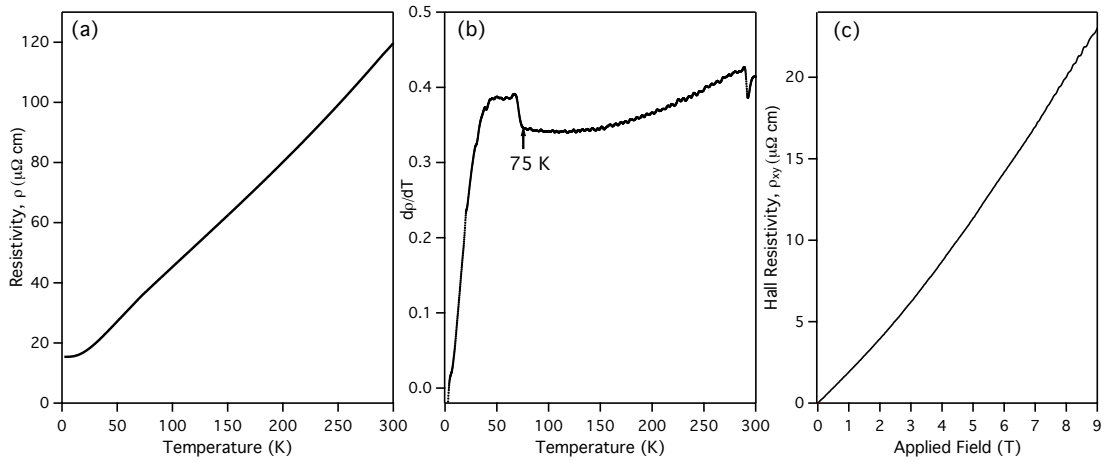

Figure 2.6: *(a) The resistivity curve of sample S21 from growth 2 50:50 SnTe. (b) The resistivity differentiated with respect to temperature to deduce a transition temperature of 75 K. (c) The Hall resistivity measured across the sample up to 9T*

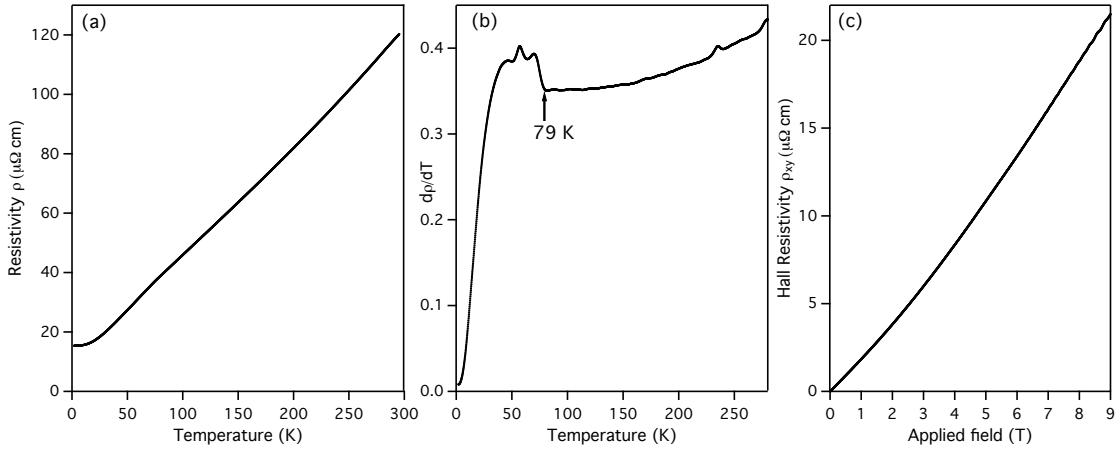

Figure 2.7: *(a) The resistivity curve of sample S22 from growth 2 50:50 SnTe. (b) The resistivity differentiated with respect to temperature to deduce a transition temperature of 79 K. (c) The Hall resistivity measured across the sample up to 9T*

The growth was repeated in an attempt to produce crystals of much higher quality. Again equal molar weights of Sn and Te were measured and the same procedure followed to 850 °C. The furnace was cooled this time to 770 °C slightly away from the solidification line in Figure 1.5. Again after a further 24 hours the quartz was quenched in a bucket of room temperature water. The grown material

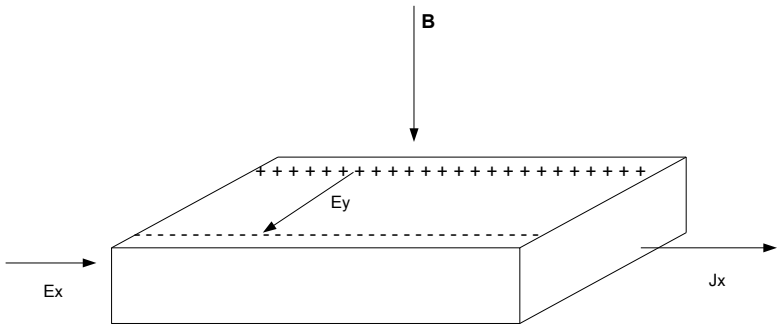

Figure 2.8: *A schematic of a typical hall bar measurement. A current with density J_x applied along the length of the sample has a perpendicular field* **B** *applied. The charge carriers are deflected via the Lorentz force to build up a Hall voltage E_y across the sample. The magnitude of the signal will be proportional to the number of carriers and its sign will depend on the carrier type.*

is shown as Figure 2.3 (b), denoted as growth 2. The physical appearance of the crystals is markedly different between the 2 growths. The large lump of material in Figure 2.3 (b) contains dozens of grains of crystals with volumes on the scale of 1-2 cubic millimeters. Several of these crystals were removed and Laue X-ray diffraction carried out. Examples of Laue diffraction patterns for the (1,0,0) and (1,1,0) directions are shown in Figure 2.4. The crystals tend to grow into cuboids with a large (1,0,0) flat shiny faces and sides of either (1,0,0) or (1,1,0). After an extensive range of Laue patterns, several single crystals were isolated for transport measurements. An example of an isolated crystal, S21, after cleaving is shown in Figure 2.5. The resistivity curve for sample S21 is shown in Figures 2.6 (a). Another single crystal sample from growth 2, denoted S22, resistivity curve is shown in Figure 2.7 (a). The resistivity was measured using a 100 μA current with frequency 37 Hz. In order to detect the change in slope of resistivity associated with the structural transition both curves were differentiated with respect to temperature and shown in Figure 2.6 (b) and Figure 2.7 (b). Clear breaks in slope are at 75 K and 79 K respectively, corresponding to T_c.

The carrier concentration, n, for these samples was deduced from adding Hall contacts across the sample. As mentioned in Chapter 1 when a magnetic field, **B**, is applied perpendicularly to a current carrying conductor, the charge carriers are deflected by the Lorentz force. If the current density, J_x, is applied along the

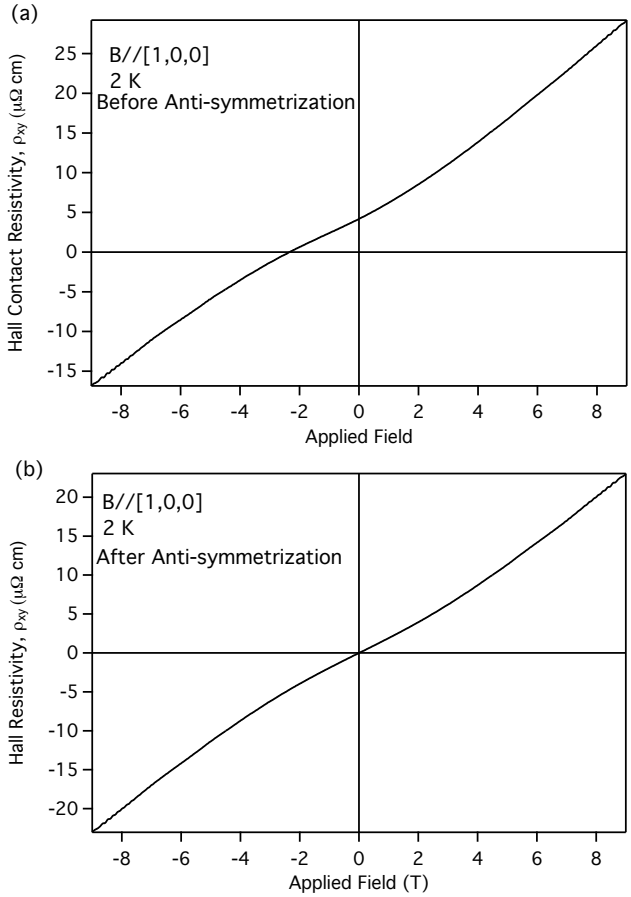

Figure 2.9: *(a) The raw Hall resistivity measured from the Hall contacts across sample S21 where misaligned has occured. (b) The Hall resistivity for S21 after anti-symmetrization according to equation (2.3) was done.*

length of the sample as shown in Figure 2.8, when **B** is applied perpendicularly an electric field, E_y, denoted the Hall field builds up to balance this Lorentz force. In the steady state the Hall field and observable Hall voltage is proportional to the overall charge carrier density. Changing the direction of **B** will also change the direction of the Hall contribution. When all directions are considered the sign of the Hall voltage will then be indicative to the type of carriers i.e. holes or electrons. The Hall resisitivity across the sample is denoted ρ_{xy}. The longitudinal resistivity along the sample, known as the magnetoresistance, is then called ρ_{xx}. These labels are more easily understood when one considers the resistivity tensor for the material in a magnetic field.

The resistivity tensor for field along the z direction in a cubic material such

Sample	Transition Temp (K)	n $\times 10^{20}$cm^{-3}	n* $\times 10^{20}$cm^{-3}
S21	75	3.23 ± 0.12	5.38 ± 0.2
S22	79	3.09 ± 0.14	5.15± 0.23
S23	75	3.30 ± 0.14	5.50 ± 0.23
S24	72	3.55 ± 0.19	5.92 ± 0.32

Table 2.1: A table of various different single crystal samples from growth 2. Shown are their transition temperatures along with measured carrier concentrations, n. The nominal carrier concentration n^* is also included.

as SnTe, is written as

$$\rho = \begin{pmatrix} \rho_{xx} & \rho_{xy} & 0 \\ \rho_{yx} & \rho_{yy} & 0 \\ 0 & 0 & \rho_{zz} \end{pmatrix} = \begin{pmatrix} \rho_{xx} & \rho_{xy} & 0 \\ -\rho_{xy} & \rho_{xx} & 0 \\ 0 & 0 & \rho_{zz} \end{pmatrix}. \tag{2.1}$$

In a very isotropic material such as SnTe transverse-longitudinal coupling is small and the ρ_{zz} is ignored. Due to unavoidable misalignment of the contacts there is always a Hall contribution to the magnetoresistance contacts and vice versa. Because of the symmetric form of ρ_{xx} and anti-symmetric form of ρ_{xy} as shown in equation 2.1, by changing the direction of the applied $\mathbf{B}$, these misaligment contributions can be eliminated using the equations

$$\rho_{xx} = \frac{1}{2}(\rho^+_{xx} + \rho^-_{xx}) \tag{2.2}$$

and

$$\rho_{xy} = \frac{1}{2}(\rho^+_{xy} - \rho^-_{xy}) \tag{2.3}$$

where the superscript indicates the direction of $\mathbf{B}$ (either positive or negative).

If we consider the case of the Hall contacts on sample S21 the raw Hall resistivity is shown in Figure 2.9 (a) for both positive and negative field directions. The contact misalignment causes the zero Hall resistivity to be almost -2.2 T from from zero applied field. Anti-symmetrisation of the form described by equation (2.3) is then done to give the Hall resistivity in Figure 2.9 (b) where now the zero Hall resistivity occurs at 0 T (the positive field part is now the same curve as that shown in figure 2.6 (c)). In the normal Hall effect the Hall coefficient is

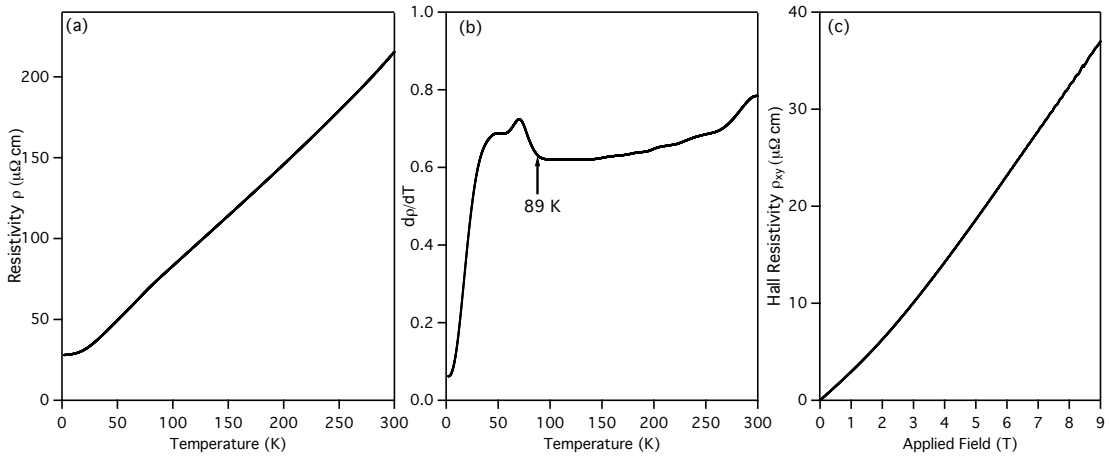

Figure 2.10: *(a) The resistivity curve of sample S31 from growth 3 51:49 SnTe. (b) The resistivity differentiated with respect to temperature to deduce a transition temperature of 89 K. (c) The Hall resistivity measured across the sample up to 9T*

Sample	Transition Temp (K)	n $\times 10^{20}$cm^{-3}	n* $\times 10^{20}$cm^{-3}
S31	89	2.00 ± 0.11	3.33 ± 0.18
S32	83	2.20 ± 0.15	3.66± 0.25
S33	79	2.82 ± 0.25	4.70 ± 0.42

Table 2.2: A table of various different single crystal samples from growth 3. Shown are their transition temperatures along with measured carrier concentrations, n. The nominal carrier concentration n^* is also included.

defined as

$$R_H = \frac{\rho_{xy}}{B} = -\frac{1}{ne} \tag{2.4}$$

allowing determination of the carrier concentration n. The carrier concentration is deduced by taking the gradient of the Hall curve between 0 - 2 T in Figure 2.6 (c) and 2.7 (c). The sign of the signal showed the carriers were holes. Samples S21 and S22 had hole carriers with $n = 3.23 \pm 0.12 \times 10^{20}\text{cm}^{-3}$ and $3.09 \pm 0.14 \times 10^{20}\text{cm}^{-3}$ respectively. Several other samples were measured as well as S21 and S22, all results are shown in Table 2.1.

The table includes the nominal carrier concentration, n^* where $n = 0.6\, n^*$ as decribed by Savage *et al.* [14], so direct comparison can be made with their phase diagram in Figure 1.5. From Figure 1.5 taken from Savage *et al.*, where the sample was quenched at 770 °C a value of n^* between 5 - 6 $\times 10^{20}\text{cm}^{-3}$ would be

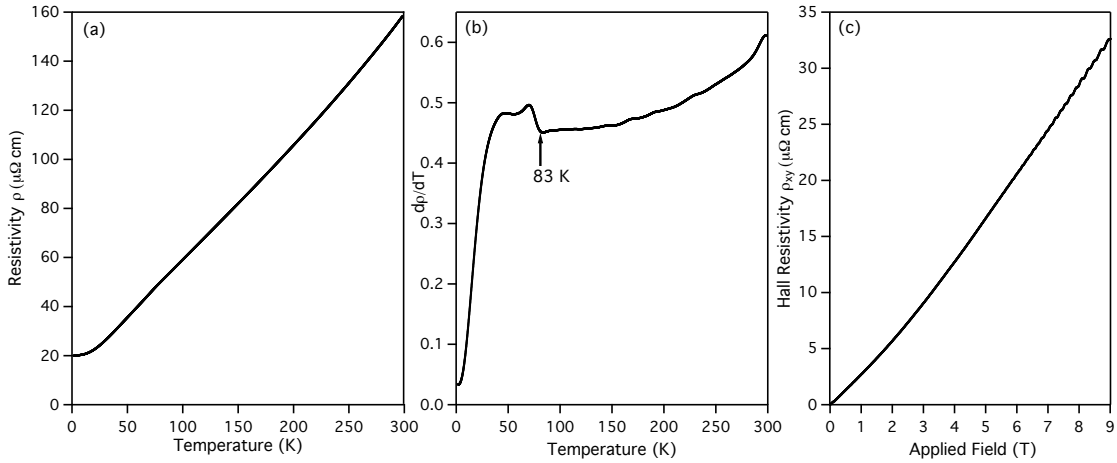

Figure 2.11: *(a) The resistivity curve of sample S32 from growth 3 51:49 SnTe. (b) The resistivity differentiated with respect to temperature to deduce a transition temperature of 83 K. (c) The Hall resistivity measured across the sample up to 9T*

expected. All measured samples fall within this range as shown in Table 2.1. The transition temperatures of the samples varies between $\sim$ 70-80K where those with lower carrier concentrations have correspondingly higher T_c's. These T_c results are consistent with the those expected for such values of n in Kobayashi *et al.* [29].

A further growth was carried out with a Sn:Te molar ratio of 51:49 in an attempt to diffuse more Sn into the samples. The same temperature profile was used as in growth 2. The resulting material from growth 3 is shown in Figure 2.1 (c). Again the lump of material in Figure 2.3 (c) contains dozens of grains of crystals with volumes on the scale of a 1-2 cubic millimeters. Several of these crystals were removed and Laue X-ray diffraction carried out. From the Laue patterns the samples again have very good crystallinity and grown with similiar orientations as before in growth 2. Resistivity and Hall effect measurements were then carried out on several samples as shown in Figures 2.10 and 2.11. Again each figure contains the resistivity (a), the differentiated resistivity (b) and the Hall resistivity after anti-symmetrization(c). The results of these samples and another S33 are shown in Table 2.2. The transition temperatures of the samples now varies between $\sim$ 79 - 89 K with lower carrier concentrations as would be expected. Again these values of T_c are consistent with the those in the literature [29].

2.3 Quantum Oscillations

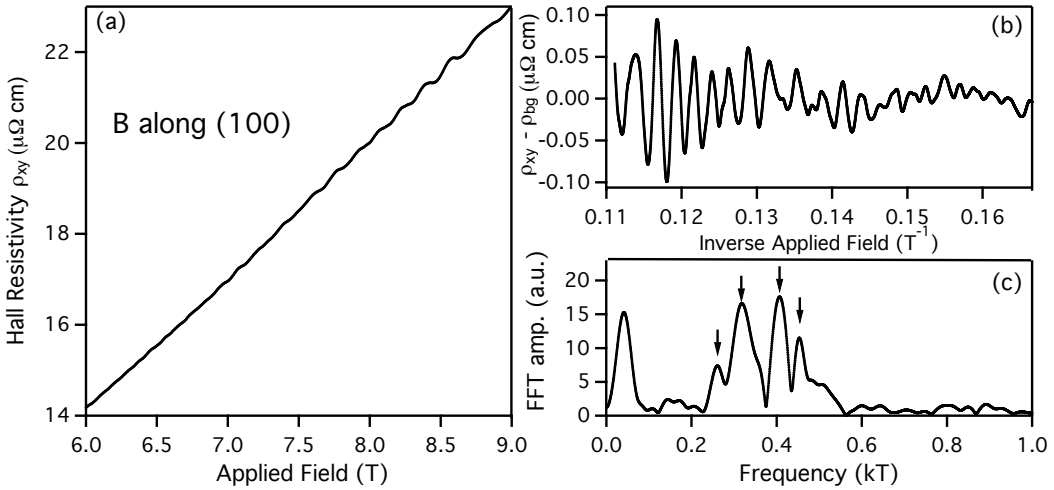

Figure 2.12: *(a) The Hall resistivity, ρ_{xy}, in sample S21 from 6 to 9 T, with the field applied along the (1,0,0) direction. A 5th order polynomial was fiitted to the curve as a background. (b) A graph of ρ_{xy} minus the background polynomial to reveal the oscillations against the inverse field. The graph is an interpolation of 5000 points (c) A FFT of the data in (b) padded with 100,000 zeros after a Hanning window was applied .*

As can be seen in the Hall signal of Figures 2.6 (c) oscillations exist at higher values of field and are also seen in magnetoresistance. To analyse the data first the high field region where the oscillations exist was interpolated with the field as shown in Figure 2.12 (a) for sample S21. The field had been applied along the (1,0,0) direction while the current was also applied along an equivalent cubic axis (0,1,0). To extract the osillations a 5th order polynomial was fitted to the data as a smoothly varying background. This background, ρ_{bg}, was subtracted from the data ρ_{xy} leaving oscillations about zero. The oscillations were then interpolated with their inverse field as shown in Figure 2.12 (b). According to the Onsager relation the period of the oscillations, T, is given by

$$T = \Delta\frac{1}{B} = \frac{2\pi e}{\hbar}\frac{1}{S} \tag{2.5}$$

as discussed in Chapter 1. Therefore the oscillations are periodic in inverse field. In Figure 2.12 (b) the oscillations are periodic but clearly more than one oscillation frequency is present. To obtain the frequencies of the oscillations a

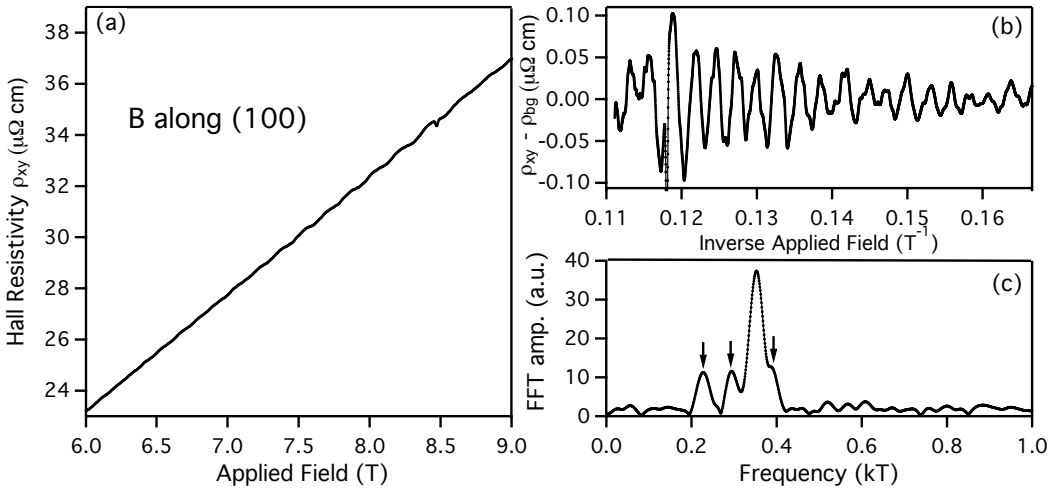

Figure 2.13: *(a) The Hall resistivity, ρ_{xy}, in sample S31 from 6 to 9 T, with the field applied along the (1,0,0) direction. A 5th order polynomial was fiitted to the curve as a background. (b) A graph of ρ_{xy} minus the background polynomial to reveal the oscillations against the inverse field. The graph is an interpolation of 5000 points (c) A FFT of the data in (b) padded with 100,000 zeros after a Hanning window was applied .*

fast Fourier transform (FFT) was carried out . The lecture course by Sheikin [41], which uses the text of Shoenberg [38], describes carrying out the FFT.

If x_n is a sequence of length N a discrete Fourier transform (DFT) is then

$$F_k = \sum_{n=0}^{N-1} x_n \exp\left(-\frac{2\pi i}{N} kn\right) \qquad k = 0, ..., N-1 \tag{2.6}$$

for data collected at an equal time interval t. Then the indexes can be easily converted into time $t = n\Delta t$ and frequency $f_k = \frac{k}{N\Delta t}$. The frequency resolution will be

$$\Delta f = \frac{1}{N\Delta t} \tag{2.7}$$

and the maximum frequency

$$f_{max} = \frac{1}{2\Delta t} \tag{2.8}$$

The same can be applied for a magnetic field range (B_{min}, B_{max}) interpolated into N_{int} points, now

$$\Delta t \to \Delta\left(\frac{1}{B}\right) = \frac{1}{N_{int}-1}\left(\frac{1}{B_{min}} - \frac{1}{B_{max}}\right) = \frac{1}{N_{int}-1}\frac{B_{max}-B_{min}}{B_{max}B_{min}} \tag{2.9}$$

[1,0,0] freq (T)	[1,1,0] freq (T)	[1,1,0] freq (T) from Savage *et al.*
257	184	180
316	210	210
408	235	230
452	267	260

Table 2.3: A table showing quantum oscillation frequencies for sample S21 with field applied along (1,0,0) direction in 1^{st} column. The quantum oscillation frequencies for field along the (1,1,0) in sample S24 are shown in the 2^{nd} column to be compared with the frequencies measured by Savage *et al.* [14] along (1,1,0) on a sample with similiar n.

Then the frequency resolution will be

$$\Delta F = \frac{N_{int} - 1}{N_{int}} \frac{B_{max} B_{min}}{B_{max} - B_{min}} \tag{2.10}$$

with maximum frequency

$$F_{max} = \frac{N_{int} - 1}{2} \frac{B_{max} B_{min}}{B_{max} - B_{min}} \tag{2.11}$$

The frequency resolution is improved by padding the interpolated data with zeros up to a total number of points N_{tot}. This works by increasing the sampling rate in what is known as a fast Fourier transform.

Figure 2.12 (c) shows the FFT of the data in Figure 2.12 (b) where $N_{int} = 5000$ for the range $B_{min} = 6$ T to $B_{max} = 9$ T, padded with 100,000 zeros. To reduce any spectral leakage in the FFT a correction window is applied to the data. The window that gives best results is that of the Hanning window,

$$w(n) = \frac{1}{2}\left[1 - \cos\left(\frac{2\pi n}{N-1}\right)\right] \tag{2.12}$$

which sharpens the frequency peaks and throws out the high frequency peaks belonging to discontinuities.

From Figure 2.12 (c) 4 frequencies exist along the (1,0,0) direction within a short range indicated by the black arrows and are given in table 2.3. The same 4 frequencies exist in magnetoresistance where oscillations also have the same phase. This is similiar to the results of Savage *et al.* shown in Figure 1.10 (a) on a sample with similiar n where 4 frequencies were evident along the (1,1,0)

direction and are also given in Table 2.3. There is also peak at very low frequency that may belong to a second pocket of carriers or is a consequence of the spectral leakage. The sample S31 also displays quantum oscillations for the field applied along (1,0,0), the results are shown in Figure 2.13. The same method of anaylsis is used as already discussed. Clearly in Figure 2.13 (c) still more than one frequency exists with 3 distinct peaks and a shoulder indicating a possible 4th, as shown by the black arrows. The carrier concentration in sample S31 is smaller than that of S21 so the decrease in the value of the peak frequencies is as to be expected.

In order to resolve these oscillations and their frequencies better, lower temperatures and higher fields were desirable. However beforehand optimisation of oscillation amplitude via the set-up electronics was carried out on the CCR in Edinburgh. An investigation of how the oscillation amplitude and frequency varied with applied current frequency was done at 17Hz, 27Hz, 37 Hz, 63 Hz and 77Hz. No significant changes were seen in oscillation amplitude or frequency at all current frequencies measured. However at larger current frequencies out of phase components at high field became large prompting measurements to be carried out at either 37 or 23 Hz. Currents of 100 μA were chosen to minimise sample heating that would damp the oscillations and maximise the signal to noise ratios. After optimisation of the electronics a sample was then prepared to be measured in the dilution fridge set-up from Oxford instruments Ltd. at the University of St. Andrews.

The method of dilution refridgeration uses a mixture of He^3 and He^4 to achieve mK temperatures. The set-up also contains a 15 T magnet with the field direction along the length of the insert probe of the fridge. The loading of the sample and data collection was done with the help of Calum Lithgow and Jean-Philippe Reid. A sample was chosen from growth 2 denoted as S24 with a $T_c = 72$ K and $n = 3.55 \pm 0.12 \times 10^{20}\text{cm}^{-3}$ (see Table 2.1). The sample is carefully cut so the (1,0,0) axis was along its thickness, the (0,1,0) along its length and (0,0,1) along its width, just as in sample S21 shown in Figure 2.3.

Four contacts were attached along its length so magnetoresistance could be measured. The sample was again mounted on a OFHC copper block. The block was placed on a 1-axis rotator designed and made by Jack Barraclough (University of St. Andrews) shown in Figure 2.14 (a) so the axis of rotation was along the (0,1,0) of the sample. The rotator was then attached to the Dilution refridgerator

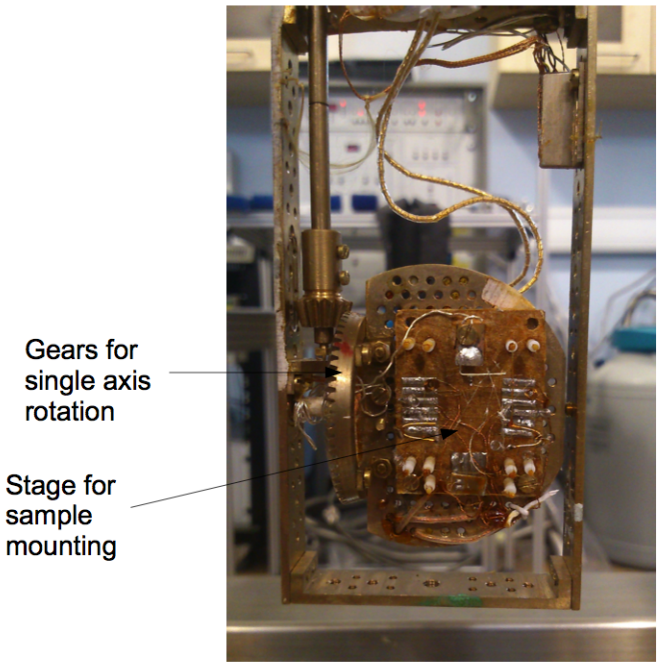

(a)

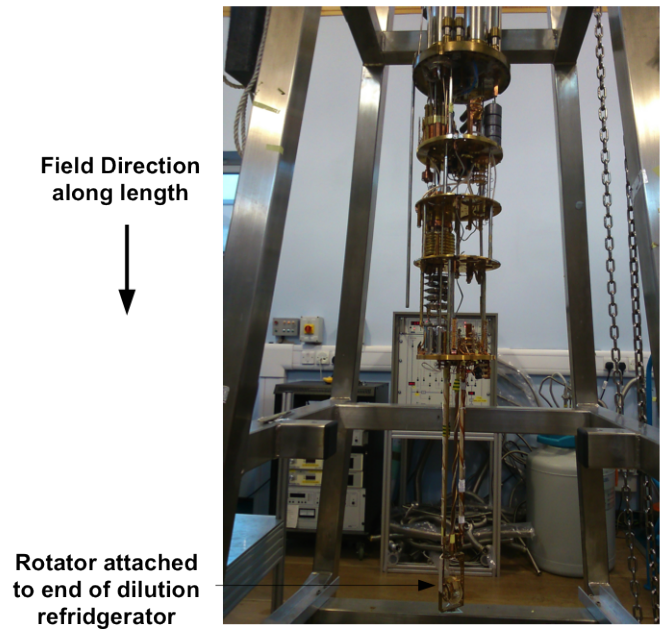

(b)

Figure 2.14: *(a) A picture of the 1-axis rotator designed by Jack Barraclough. (b) The rotator attached to the dilution refridgerator showing the field direction at which about rotation takes place.*

as shown in Figure 2.14 (b) so the sample could be rotated with respect to the field from the magnet. The field direction on the sample could then be determined using a Hall sensing probe. Then at a 45° rotation the field was along the (1,1,0) direction and at 90° along the (001). The magnetoresistance was preferred to measuring the Hall effect since as the angle of rotation reached 90° the Hall voltage would also decrease to zero.

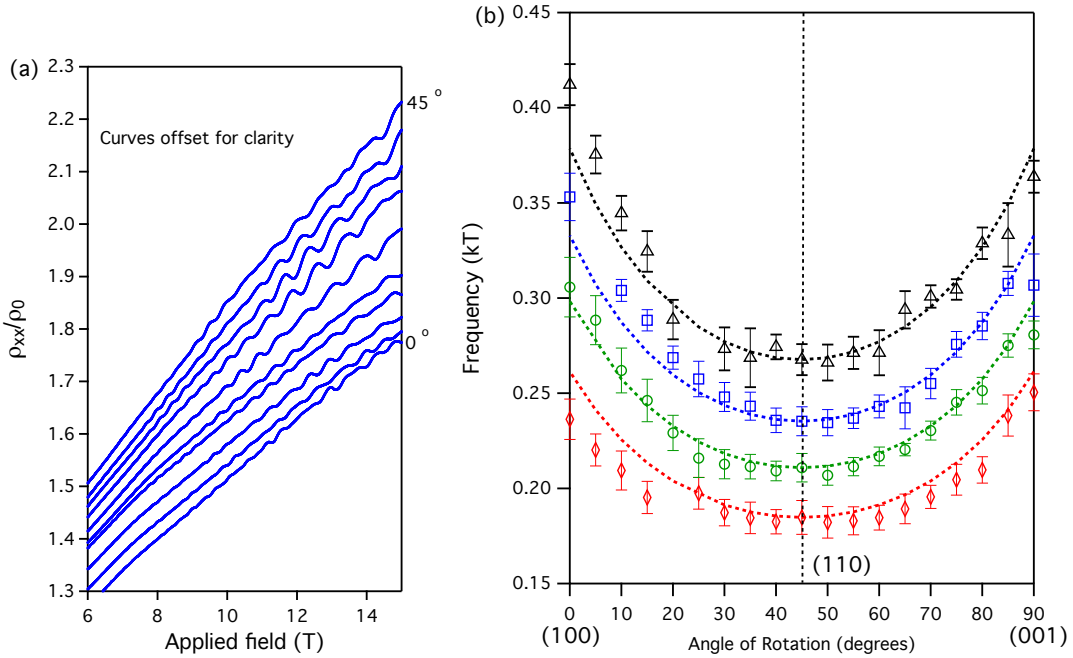

Figure 2.15: *(a) The measured magnetoresistance at various angles of rotation. The curves go from* 0° *to* 45° *in* 5° *increment steps and are offset for clarity. Clear oscillations are evident in the data. The oscillations have a background subtracted and interpolated against inverse field before a FFT was carried out. The FFT displays 4 frequencies at each angle of rotation. The frequencies against angle are plotted in (b) where the (1,0,0), (001) and (1,1,0) are indicated. The dashed coloured curves are equal to* $F_0/\cos\theta$ *where* $\theta = 0$ *at* 45° *and* F_0 *te frequency at the (1,1,0) along the (1,1,0).*

The sample was cooled to 20 mK and the magnet ramped to 15 T at 0.05 T/min. Data was first collected with the rotator at 0° and the field applied along (1,0,0). Rotation was then carried out from 0° to 90° in 5° increment steps. At each increment the field was ramped between 4 - 15 T at 0.05 T/min. The data between 6 - 15 T is shown in Figure 2.15 (a) going from the (1,0,0) at 0° to the (1,1,0) at 45° in 5° increment steps. The curves are offset for clarity. The same

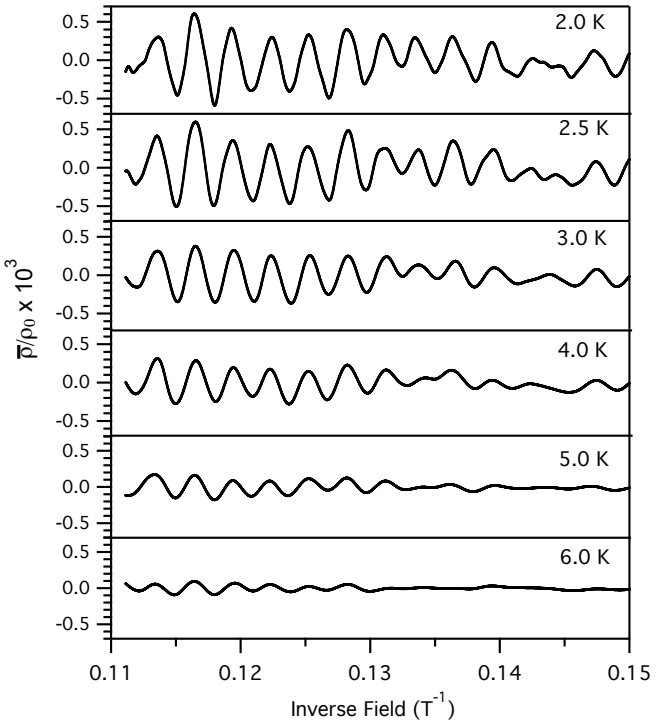

Figure 2.16: *The oscillations $\overline{\rho}$ after the background polynomial has been subtracted normlised to ρ_0 against inverse applied field for various temperatures. The field has been applied along the (1,0,0).*

procedure of smooth background subtraction and interpolation with inverse field was carried out on each sweep.

A FFT with 100,000 padding zeros was carried out again with a Hanning window applied to the data. At each angle of rotation 4 clear frequency peaks are evident in the FFT, all within quite close range to each other. The 4 peaks are plotted along against angle of rotation in Figure 2.15 (b). The minimum frequencies occur along the (1,1,0) direction as indicated by the dashed black line where frequencies are given in table 2.3. This almost exact agreement with the measurements of Savage *et al.* [14] along the (1,1,0) direction on a sample with similiar n of at as shown in Figure 1.10 (a) and also given in Table 2.3. The slight differences could be attributed to sample quality and small changes in n. The 4 dashed coloured curves are equal to $F_0/\cos\theta$ where $\theta = 0$ at 45° along the (1,1,0) and F_0 is then the frequency at the (1,1,0). These curves and their significance will be discussed further in section 2.4.

To determine the effective mass field sweeps were carried out between 2-6 K

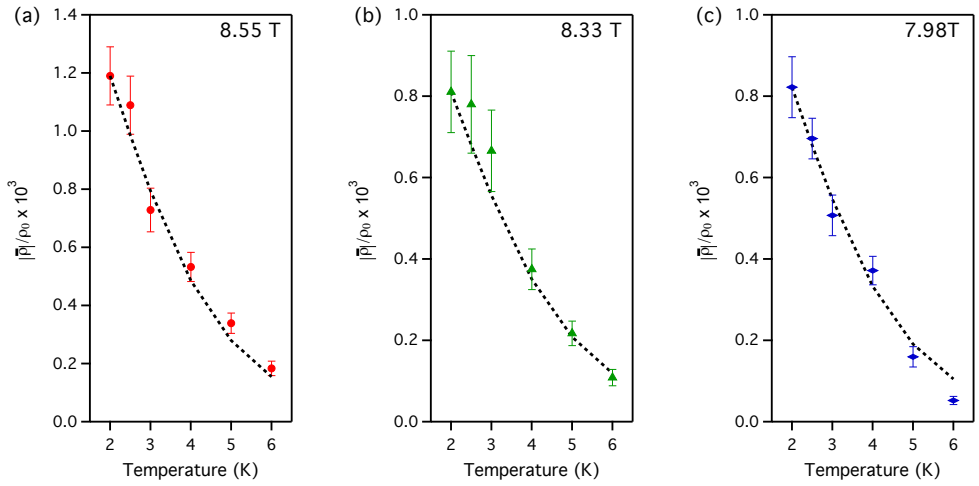

Figure 2.17: *The magnitude of oscillations* $|\,\overline{\rho}\,|$ *normalised to zero field resistivity* ρ_0 *against temperature for various fields. The dashed lines are then fits to the Lifshitz-Kosevich temperature damping factor,* R_T*. The value of* m^* *is varied to obtain the best fits, with all fits shown for* $m^* = 0.45\ m_e$*.*

up to 9 T in the variable temperature insert system in Edinburgh. Oscillations were evident between 6-9 T in this set-up for the field applied along the (1,0,0). The amplitude of the oscillations after the background polynomial has been subtracted, $\overline{\rho}$, normalised to the zero field resistivity ρ_0 are shown in Figure 2.16 from 2 - 6 K. The decrease in amplitude is clear going to higher temperatures. As mentioned in the introduction there is a temperature damping factor, R_T, associated with quantum oscillations given by

$$\frac{|\,\overline{\rho}\,|}{\rho_0} \propto R_T \propto \frac{\alpha m^* T/B}{\sinh(\alpha m^* T/B)} \tag{2.13}$$

where $\alpha \approx 14.69$ T/K for S.I. units. To determine the effective mass the magnitude of the amplitude of several of the oscillations, $|\,\overline{\rho}\,|$, was extracted from the curves in Figure 2.16. These amplitudes were plotted against temperature in Figure 2.17 for various fields. The fields are the mean value of actual field where the oscillation occurs. The dashed curves are then fits to equation 2.13 with a value of $m^* = 0.45$. This allows an estimation of the effective mass to be $m^* = 0.45 \pm 0.03\ m_e$ electron masses.

Also mentioned in Chapter 1 is the dependence of oscillation amplitude on applied field, decribed by a field damping factor R_D. For the case of the Shubnikov

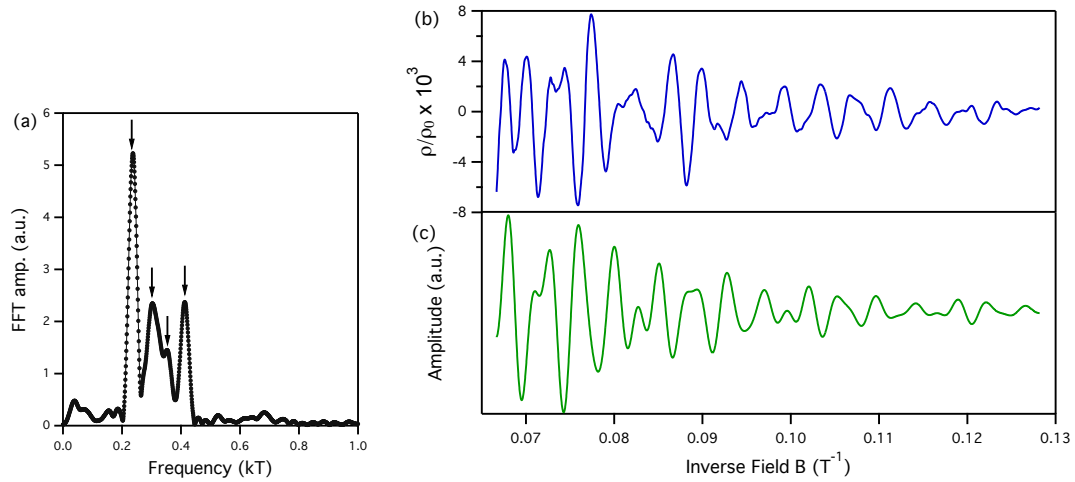

Figure 2.18: *(a) The FFT for oscillations with the field applied along the (1,0,0) direction at 20 mK. There are 4 clear peaks in the frequency. (b) The oscillations after a smoothly varying background has been subtracted plotted against inverse field. The oscillations have been normalised to the zero field resistivity. (c) A summation of 4 cosine waves with frequencies deduced from the FFT damped by the Dingle factor R_D with $T_D = 8\ K$*

de Haas oscillations

$$\frac{|\,\overline{\rho}\,|}{\rho_0} \propto R_D \propto \frac{1}{B^2}\exp\left(\frac{-\alpha m^* T_D}{B}\right) \tag{2.14}$$

where T_D is the Dingle temperature. Due to the existence of several frequencies occuring over the same field range it is difficult to obtain an amplitude dependence on field. The oscillations against inverse field for **B** applied along the (1,0,0) at 20 mK are shown in Figure 2.17 (b), where the field dependence on amplitude is clear. The FFT of the data is shown in Figure 2.17 (a) with 4 clearly distinct frequencies as already discussed, indicated by the black arrows. To try and replicate this field dependence, 4 cosine waves were summed to produce a wave of amplitude, A, given by

$$A = \sum_n \cos(2\pi A_n^{rel} F_n B + \phi) \tag{2.15}$$

where F_n are the frequencies deduced from the FFT and ϕ is just a phase correction were considered. The relative amplitude, A_n^{rel}, of each frequency is also deduced fom the FFT.

The summation of the 4 waves and the resulting beating formation is shown

[1,0,0] freq (T)	Scattering length (Å)
236	330
302	377
352	407
412	441

Table 2.4: A table showing quantum oscillation frequencies for sample S24 with field applied along (1,0,0) direction in 1^{st} column. The scattering length for each frequency is then shown in the 2^{nd} column.

in Figure 2.18 (c). Although the frequency profiles of the oscillations do not exactly match between Figure 2.18 (b) and (c) the amplitude profiles show relative agreement. The curve in Figure 2.18 (c) was for $T_D = 8$ K and used the earlier deduced $m^* = 0.45$. We can then assume a Dingle temperature of ≈ 8 K. Using this Dingle temperature an estimation for the scattering length can be made since

$$T_D = \frac{\hbar}{2\pi k_B}\frac{1}{\tau} \tag{2.16}$$

as discussed in Chapter 1. Then the scattering length l is given by

$$l = \frac{\hbar^2 k_F}{2\pi k_B m^* T_D} \tag{2.17}$$

where k_F is the Fermi wavevector and the the extremal surface area $S = \pi k_F^2 = \frac{2\pi e}{\hbar}F$. If the same Dingle temperature and effective mass is assumed for the various frequencies in the FFT then values of scattering length could be calculated and are shown in Table 2.4. Of course it may not be the case each frequency belongs to a part of the Fermi surface with the same m^* and T_D.

2.4 Discussion

Two growths of SnTe have produced single crystals of high quality. The resistivity curves show clearly the samples pass through the structural transition giving an accurate determination of T_c. Growth 3 with a Sn:Te molar ratio of 51:49 produced crystals with lower carrier concentrations and higher T_c's than the growth 2 with 50:50 ratio. This extra molar weight of Sn has then replaced some of the Sn vacancies in the lattice lowering n. Other groups have successfully

diffused more Sn into the sample by vacuum annealing in the presence of Sn ingots [13]. However an extensive search of the literature proves stoichiometric SnTe has not be thus far achieved. Annealing in the presence of elemental Sn may not give an even diffusion into the samples etc., possibly lowering overall sample quality. Some attempts were made to vary the carrier concentration by annealing, which proved unsuccessful. The as-grown material was instead used for all experiments in the thesis even though n is still relatively high.

The vast majority of previous experiments have used single crystals grown by Czochralski or Bridgman techniques. These provide crystals of much larger sizes than our currently grown samples that can be used in neutron experiments such as those by Pawley *et al.* [25] . However crystals of such large sizes will most likely not have a very even distribution of Sn vacancies throughout the entire crystal. The material itself is also very brittle and cracks form easily. Large crystals would then contain many cracks and other dislocations etc.. So our grown crystals may be rather small in comparison but their size and method of preparation should hopefully mean a more even distribution of vacancies.

The quantum oscillation data in all samples measured showed 4 clear similar frequencies. Sample S24 showed the 4 frequencies following the same shape rotating from (1,0,0) to (0,1,0) via the (1,1,0) as shown in Figure 2.15 (b). The frequency minimum F_0 occurs at the (1,1,0) point. Figure 2.15 (b) also contains curves of $F_0/\cos(\theta)$ as discussed in the text. Quantum oscillation frequencies following such a $1/\cos(\theta)$ shape would be caused by a Fermi surface with the shape of a long cylinder. Savage *et al.*'s [14] quantum oscillation data on a sample with a very similar n to S24 is shown in Figure 1.10 (a) also containing 4 frequencies. The values of F along the (1,1,0) in Figure 1.10 (a) agree very closely with those measured here on S24 as already discussed. Savage *et al.* [14] did not measure quantum oscillations along the (1,0,0) direction due to a possible increase in scattering or effective mass. However as shown we clearly can measure along the (1,0,0) and can deduce the shape of the Fermi surface further.

Using the results of Savage *et al.* [14] which indicate the minimum frequency occurs at the L-point then the Fermi surface is made up of 4 pockets that are elongated cylinder shapes along L. Why there are 4 frequencies is a matter of interpretation. The structural distortion elongates the Brillouin zone along the (1,1,1) direction. So this elongation could change the Fermi surface in that

direction and one would then expect 2 different quantum oscillation frequencies. Further to this the shape of the pockets may also be modified leading to a further doubling in the number of frequencies. Quantum oscillations are measured under high pressure in Chapter 4. Pressure was seen to suppress the structural transition. When suppressed the 4 measured oscillation frequencies became a single frequency, clearly indicating the 4 frequencies are a cause of the distortion. However a direct comparison with theory is needed to see how the distortion affects the Fermi surface so that 4 frequencies are detected.

Along the (1,1,1) direction Savage *et al.* [14] measured $m^* = 0.125 \pm 0.012\ m_e$. For the (1,0,0) direction results here, a value of $m^* = 0.45 \pm 0.05\ m_e$ was deduced. This increase in effective mass would be one reason Savage *et al.* [14] did not measure oscillations along (1,0,0) as they pointed out. Savage *et al.* [14] also measure a value of $T_D = 17.3 \pm 1.7$K along the (1,1,1) direction whilst these results produce a value of $T_D \approx 8 \pm 2$K along the (1,0,0). Also suggesting an increase in scattering rates along this direction. However Savage *et al.* [14] were able to make a much more accurate determinations of m^* and T_D because they were calculated from a sample of very high carrier concentration that displayed only one frequency belonging to the pockets at L. In determining T_D we have assumed m^* is the same for each frequency which may not be the case. One should also note the value of m^* and T_D will most likely be very sample and n dependent. Therefore a direct comparison between samples may not be valid. Measurements for m^* and T_D on the same sample with and without the transition suppressed by pressure is discussed in Chapter 4.

Also seen in the sample of Savage *et al.* [14] with high n is the formation of another small pocket of holes. Allgaier and Houston [39] suggest this second pocket is elongated along the (1,0,0) directions. There may be some indications of this second pocket within some of our samples such as in S21 in Figure 2.12 (c) where a frequency of very low value in the FFT transform is seen. It is however absent in the FFT in Figure 2.13 (c) belonging to sample S31 with a smaller n. The filling of this second pocket may then be possible even in the distorted phase. The next chapter will now discuss the detection of the structural transition in SnTe using inelastic X-ray scattering to measure its phonon dispersion curves.

Chapter 3

Inelastic X-Ray Scattering in SnTe

This Chapter discusses inelastic X-ray scattering on a single crystal of SnTe from growth 2. A brief introduction to the technique is given as well as a description of the experiment. Measured phonon dispersion curves at various **q** vectors throughout the Brillouin zone are then discussed. Upon cooling, transverse optic phonon softening and recovering was seen corresponding to the structural transition. These measured results are also compared with calculated phonon dispersion curves carried out by Andreas Hermann.

3.1 Technique and Sample set-up

As mentioned in Chapter 1 phonon dispersion curves can be measured in experiments in which the lattice vibrations exchange energy with an external probe. Traditionally the inelastic scattering of neutron beams was the technique of choice, to accurately measure the dispersion curves, via the nuclear motion of the atoms. However the use of inelastic X-ray scattering to measure the coherent motion of electronic clouds around the atoms is now possible. The equivalence of the two is then based on the adiabatic approximation that the electrons move with the nuclei [42]. Phonons have an energy on the scale of meV similiar to that of thermal neutrons while X-rays have energies on the scale of keV. But by using a high resolution monochromator the bandwidth of the incident X-rays can be reduced to the meV level. The scattered beams pass through analysers with

similiar resolution allowing for measurement of phonon dispersion curves. The main advantages for using X-rays is the reduction in size of the samples. Due to the low flux of neutron sources samples with volumes of cm^3 are required. But current synchrotron light sources allow for extremely small samples to be studied, such as the single crystals of SnTe discussed in the previous chapter. An inelastic X-ray experiment was carried out on a sample of SnTe at the European Synchrotron Radiation Facility's (ESRF) ID28 inelastic X-ray scattering beamline to measure its phonon dispersion.

For any scattering experiment the laws of energy and momentum conservation apply

$$\mathbf{Q} = \mathbf{k}_f - \mathbf{k}_i \tag{3.1}$$

$$\mid \mathbf{Q} \mid = k_i^2 + k_f^2 - 2k_i k_f \cos\theta_S \tag{3.2}$$

$$\hbar\omega = E_i - E_f \tag{3.3}$$

where in equation (3.1) the scattering vector $\mathbf{Q}$ is the difference between the incoming and outgoing wavevectors $\mathbf{k}_i$ and $\mathbf{k}_f$ respectively. This then represents the momentum conservation. Equation (3.3) then represents the energy conservation where $\hbar\omega$ is the energy transferred to the sample which is the difference between the incoming and outgoing energies E_i and E_f respectively.

For elastic scattering, $\mid \mathbf{k}_i \mid = \mid \mathbf{k}_f \mid$, so for $\mathbf{Q}$ equal to $\mathbf{G}$, a reciprocal lattice vector, the Bragg condition

$$\mathbf{Q} = \mathbf{G} = \mathbf{k}_f - \mathbf{k}_i \tag{3.4}$$

will be satisfied, as is the case in the diffracted spots in the Laue diffraction technique discussed in the previous chapter. Inelastic scattering is much more complicated. Now $\mid \mathbf{k}_i \mid \neq \mid \mathbf{k}_f \mid$, since energy has been transferred between the photon and the sample. Two situations can then arise

1. $k_i > k_f$ and $\hbar\omega > 0$ so energy is transferred from the incident wave to the sample and an excitation is created

2. $k_i < k_f$ and $\hbar\omega < 0$ so the sample gives up a quantum of energy to the incident beam and an excitation annilhilated

Chapter 2 of the text by Shirane *et al.* [43] contains the formulas describing inelastic scattering and shall not be repeated here. The term we are interested in is

the dynamical structure factor $S(\mathbf{Q},\omega)$, associated with the inelastic scattering of the phonon excitations with incident photons as a function of $\mathbf{Q}$ and ω, where ω is the frequency. It describes the correlations of the electron density in the material with which the photon interacts. This is the quantity measured experimentally in a scattering experiment. An important feature of $S(\mathbf{Q},\omega)$ is the phonon creation and annilhilation energies are not independent but obey detailed balance such that

$$S(-\mathbf{Q},-\omega) = e^{-\hbar\omega/k_BT}S(\mathbf{Q},\omega) \tag{3.5}$$

where k_B is the Boltzmann constant and T the temperature. The principle of detailed balance is a general property of a sample in thermal equilibrium, where there is a balance between any two pairs of states. Thus the probability of a transition in the sample will be lower for phonon annihilation than for creation.

Detailed balance and thermal equilibrium allow $S(\mathbf{Q},\omega)$ to be described by the fluctuation-dissipation theorem discussed in Chapter 7 of the text by Chaikin and Lubensky [44] and given in equation 3.6 below. The fluctuation-dissipation theorem relates $S(\mathbf{Q},\omega)$ the response of the system (the fluctuation) to be described by the dynamical susceptibility $\chi(\mathbf{q},\omega)$ associated with the phonons. $S(\mathbf{Q},\omega)$ is then related to the imaginary part, or dissipative part of $\chi(\mathbf{q}\omega)$ (written $\chi^{''}$) as

$$S(\mathbf{Q},\omega) = \pi^{-1}[n(\omega)+1]\chi^{''}(\mathbf{q},\omega) \tag{3.6}$$

where $n(\omega) = 1/(e^{\hbar\omega/k_BT}-1)$ is the Bose factor. The principle of detailed balance then requires $\chi^{''}$ to be an odd function of ω so $S(\mathbf{Q},\omega)$ is always positive.

For the case where incident X-rays create or annilhilate completely harmonic phonons then $\chi^{''}$ will be written in terms of Delta functions. However as already discussed in Chapter 1 we must also consider higher order anharmonic terms. The consequence of these anharmonic terms is not only a renormalisation but also a linewidth of the frequencies. The linewidth is caused by electron-phonon, phonon-phonon interactions etc.. So then $\chi^{''}$ is described more accurately by a damped harmonic oscillator written as

$$\chi''(\mathbf{q},\omega) = \frac{A}{[\Gamma(\omega)^2+(\hbar\omega-\hbar\omega_o(\mathbf{q}))^2]} - \frac{A}{[\Gamma(\omega)^2+(\hbar\omega+\hbar\omega_o(\mathbf{q}))^2]} \tag{3.7}$$

where $\omega_o(\mathbf{q})$ is the undamped harmonic phonon frequency at wavevector $\mathbf{q}$, $\Gamma(\omega)$ is the frequency dependent half-width-at- half-maximum (HWHM) caused by the

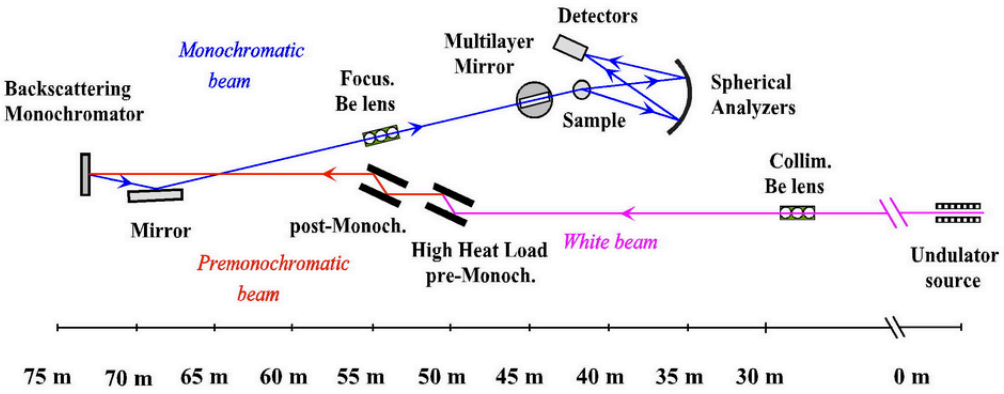

Figure 3.1: *A schematic of beamline ID28 taken from the ESRF website [45].*

damping and A is the amplitude. Equation (3.7) is then of the form an anti-symmetrised function composed of two Lorentzians and is an odd function of ω (see paper by Stock *et al.* [46]). $S(\mathbf{Q},\omega)$ is measured experimentally by varying the energy transfer of the scattering process in the meV range, while keeping the momentum transfer constant as shall be described below.

The principle of inelastic X-ray scattering is described by the review article by Burkel [47] but the points needed to understand the ID28 beamline shall be mentioned here. A schematic of the beamline ID28 at the ESRF is shown in Figure 3.1 taken from the ESRF website. The white beam enters from the undulator source and passes through some pre-monochromators. The beam then reaches a backscattering monochromator made up of flat perfect crystals of Silicon. The monochromator works by making use of Bragg (n,n,n) reflections from the Silicon to produce a beam of well defined energy E_i and wavevector $\mathbf{k}_i$. For this experiment the (999) reflection was used to produce a monochromatic beam of 17.794 keV. The beam passes through a focussing lens and is incident on the single crystal sample where the scattering takes place. The scattered beam is then analysed for energy E_f and wavevector $\mathbf{k}_f$ by elastic scattering from concave analysers of singular crystal silicon onto a detector. This defines the momentum transfer and energy transfer in the scattering process.

The variation of the amount of energy transferred is acheived by varying the temperature of the monochromator where 2.20 meV= 48 mK. An energy scan with constant scattering angle 2Θ keeps the momentum transfer fixed and is

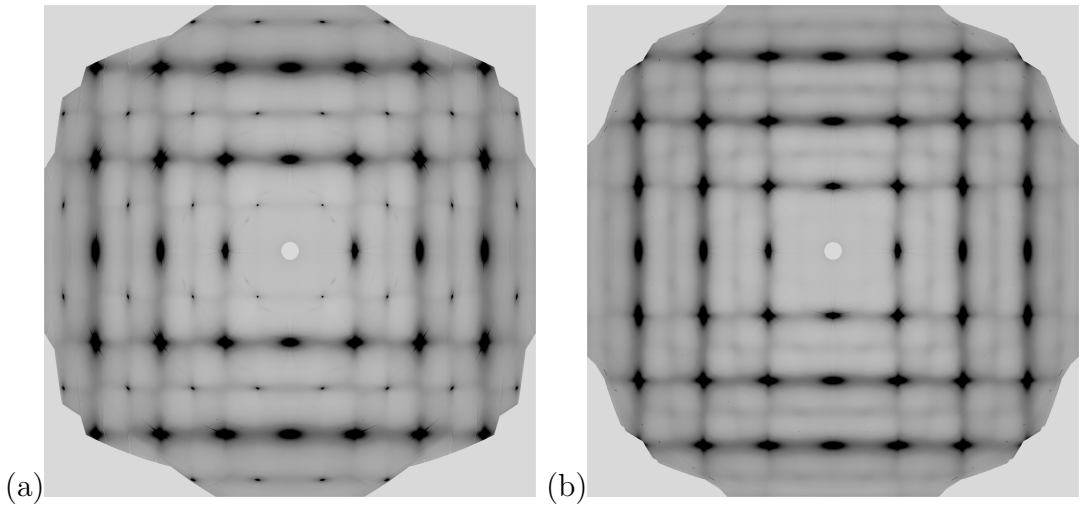

Figure 3.2: *Thermal diffuse scattering patterns on the sample of SnTe used for inelastic scattering on ID28. Both images were taken at 300 K by Alexei Bossak on ID23 at the ESRF. (a) is for an incident beam along the [1,1,1] direction of the crystal while (b) has the incident beam along the [1, $\overline{1}$,0] direction.*

known as a constant **Q** scan. In ID28 there are 9 analyser-detector pairs allowing 9 constant Q-scans to be measured at once. In this experiment the energy was scanned in 0.68 meV increments from 19.82 to -19.82 meV, the energy range one would expect to see phonon excitation and annihilation in SnTe [27]. The resulting spectrum of measured intensity vs energy transferred to the sample scan is directly proportional to $S(\mathbf{Q}, \omega)$ [42]. For an incident energy of 17.794 keV the energy resolution in the measured spectrums is 3 meV. Unlike inelastic neutron scattering however the energy resolution is independent of the energy transfer and remains 3 meV for all scans measured.

A crystal of SnTe with $T_c = 75$K from growth 2 was sent to the beamline scientist, Alexei Bossak, for preparation for inelastic X-ray scattering. The crystal was cut into a needle with the $[1, \overline{1}, 0]$ direction along its length then polished. After polishing it was etched in a mixture of nitric and hydrochloric acid with ratio 4:1 at room temperature. Thermal diffuse X-ray scattering was carried out on beamline ID23 at the ESRF by Alexei Bossak prior to the experiment taking place on ID28. This experiment was done as a preparation for the main experiment showing the phonons in the samples could be detected with X-rays and the long range order and crystal quality was good. Two diffuse scattering intensity patterns measured in a transmisson mode, with an image plate positioned behind

Q [1,0,0] direction	**Q** [1,1,0] direction	**Q** [1,1,1] direction	phonon
$(0,0,4) \rightarrow (0,0,5)$	$(4,4,0) \rightarrow (3,3,0)$	$(2,2,2) \rightarrow (3,3,3)$	Longitudinal
$(1,1,5) \rightarrow (1,1,4)$	$(3,3,1) \rightarrow (4,4,1)$	-	Longitudinal
$(4,4,0) \rightarrow (4,4,1)$	$(0,0,4) \rightarrow (1,1,4)$	$(2,2,4) \rightarrow (1,1,5)$	Transverse
$(3,3,1) \rightarrow (3,3,0)$	$(1,1,5) \rightarrow (0,0,5)$	-	Transverse

Table 3.1: A table of selected **Q** vectors along each high symmetry direction

the sample, are shown in Figure 3.2 (a) and (b) for 300 K for the [1,1,1] and [1, $\bar{1}$,0] directions respectively. The incident monocromatic beam has a wavelength selected such that the Bragg condition is never satisfied over the entire area of detection. Thus none of the spots in Figure 3.2 are caused by crystal diffraction but instead correspond to a planar projection of a unique momentum transfer **q** on the Ewald sphere [48] (**q** is the **Q** vector reduced to the 1^{st} Brillouin zone by reciprocal lattice vector **G**, see below). The scattering is therefore inelastic and the bright spots in each picture are points on the Ewald sphere that are closest to neighbouring reciprocal lattice points, where the acoustic phonon population is high. Other optic phonon modes will also contribute to the measured intensity.

The sample was mounted on the ID28 beamline to be investigated by inelastic X-ray scattering. The **Q** vectors to be measured were then decided by considering the propagation direction of the various phonon modes i.e. tranverse or longitudinal. The general requirement for a non-zero intensity spectrum at a fixed **Q** vector is the phonon mode must have some component of atomic motions parallel to **Q** (see review article by Baron [42]). The measured intensity also scales as $\mathbf{Q}^2$ (see Chapter 4 Shirane *et al.*), however at very large values of **Q** other terms such as the Debye-Waller factor can begin to reduce intensity again. Using the reciprocal lattice vector **G** each value of **Q** can then be reduced to **q** within the first Brillouin zone. For the fcc lattice the Bragg condition is fulfilled when hkl are all even or all odd. Close to the Bragg condition (i.e. near $\mathbf{q} = 0$) the intensity of acoustic modes scales with the intensity of the nearby Bragg reflection, as already discussed for the diffuse scattering. Whereas the optic mode intensities where atoms move out of phase with each other scale inversely with nearby Bragg peaks [42].

For fcc SnTe the unit cell contains 2 atoms that lead to 6 phonon branches, 3 optic and 3 acoustic. We are mainly interested in the **Q** vectors along

high directions of symmetry, namely the [1,0,0], [1,1,0] and [1,1,1] directions. Away from the high symmetry directions the atomic motion become much more complex. The **Q** vector directions chosen are shown in Table 3.1 for each high symmtery direction. The fourth column in the table indicates whether the **Q** vectors are either longitudinal or transverse in nature. Longitudinal modes have **q** parallel to **G** while transverse modes have **q** perpendicular to **G**. For any value of **Q** where the Bragg condition is met or almost met only elastic scattering will be evident on the intensity vs energy spectrum.

3.2 Phonon Dispersion Results

Intensity vs energy transfer spectra were measured between -19.82 meV to 19.82 meV. Examples of 3 raw measured spectra at 300 K are shown in Figure 3.3 for various constant **Q** scans along the (4,4,1) to (3,3,1) direction, as the markers. There are 3 peaks in each spectra corresponding to phonon annhilation and phonon creation at positive and negative energy transfers respectively as well as a peak at zero energy transfer causes by an elastic contribution. In Figure 3.3 it is the longitudinal acoustic phonon branch causing the peaks at positive and negative energy transfers. It is clear the phonon peak position changes as **Q** is varied and hence allows determination of the shape of each phonon branch. The elastic contribution also decreases with intensity as one moves further from the Bragg condition, as would be expected. Some constant **Q** scans may also contain 5 peaks caused by 2 different phonons. The intensity vs energy scans were fitted to equation 3.7 convoluted with the resolution function of the instrument. The resolution function was experimentally measured and provided to us by the beam line scientist Alexei Bossak. It is Lorentzian in shape with a full width half maximum of 3meV. After convolution the best fit to the experimental data was selected to provide accurate values of the phonon energy. Examples of the fits are shown as the solid lines in Figure 3.3.

Spectra in all the **Q** directions given in Table 3.1 were measured and analysed using the same fitting method to determine the peak positions and hence phonon energy. All measured points at 300 K for phonon creation are shown as markers against reduced zone vector **q** in Figure 3.4. The error bars shown in Figure 3.4 are equal to 5 times the error of the calculated fit. The factor of 5 was chosen to

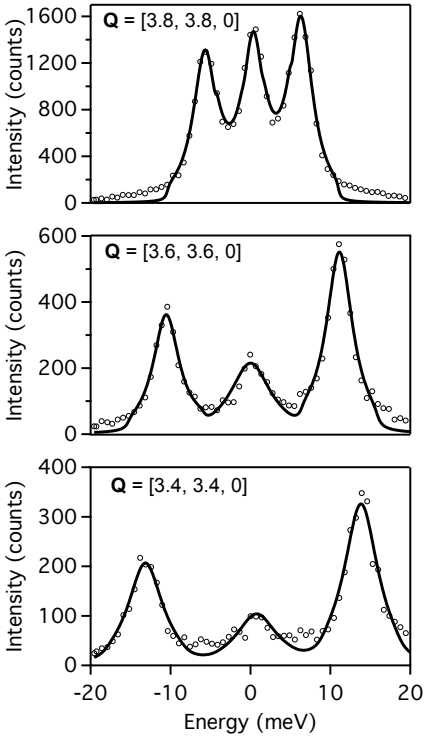

Figure 3.3: *Measured intensity vs energy transfer spectra at various values of* $\mathbf{Q}$. *The peaks at positive and negative energy transfer are caused by the longitudinal acoustic phonon. The peak at zero energy is then an elastic contribution.*

give a more generous and realistic value for the error due to any departure from the pure Lorentzian peak profiles.

The points labelled X, K and L in Figure 3.4 are the high symmetry points along the [1,0,0], [1,1,0] and [1,1,1] at the edge of the Brillouin zone. The phonon branches are denoted using their group symmtery notation in Figure 3.4 as well as their more common notation TA-phonon etc.. Figure 3.4 also includes scalar-relativistic density functional theory calculations at finite temperature 300 K for fcc SnTe carried out by Andreas Hermann shown as the dashed lines (Ground state 0 K calculations were also carried out for the rhombohedral phase, see Figure 3.13) . The scalar-relativistic density functional theory calculations used the VASP package, [49, 50, 51], a plane wave basis with cutoff energy $E_c = 200$eV, and k-point sampling with a linear density of $30/\text{Å}^{-1}$. Ground state and finite temperature phonon calculations [52, 53] used the finite displacement method in 128-atom super cells of the rhombohedral and cubic phase of SnTe, respectively.

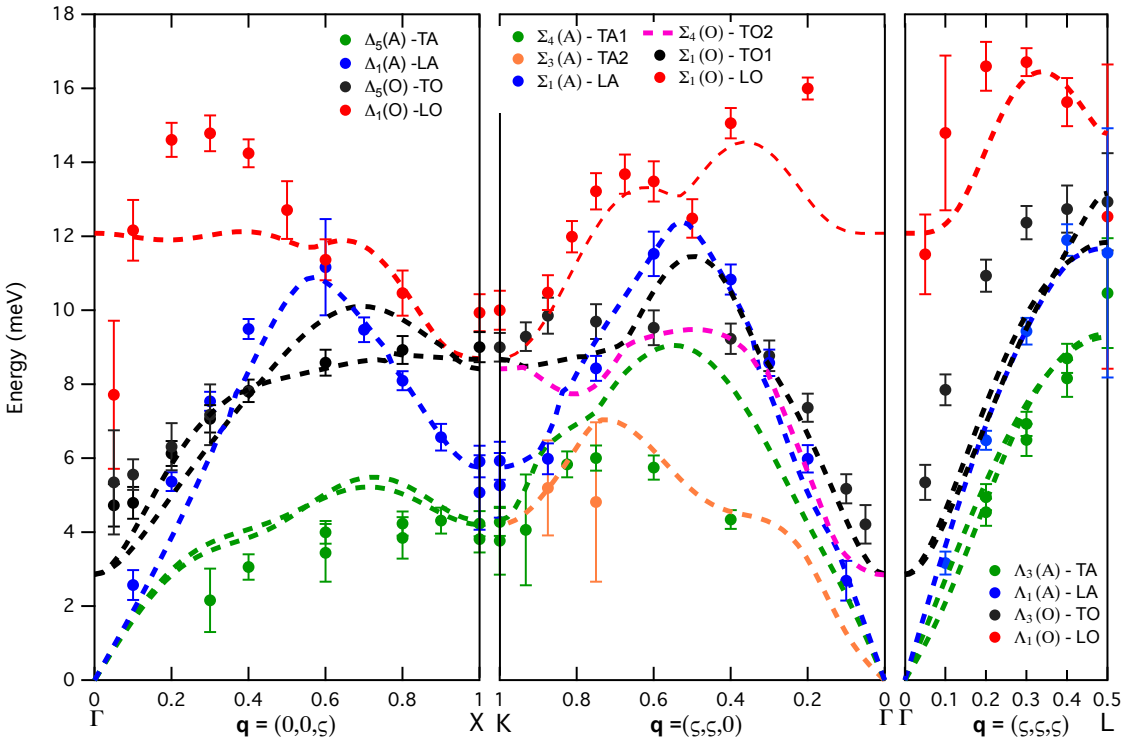

Figure 3.4: *Phonon dispersion curve energies for SnTe at 300 K in the reduced Brillouin zone with wavevector* **q** *along the 3 directions of high symmetry. The markers are measured experimental points from the phonon creation energy transfer in the intensity vs energy spectra carried out at constant* **Q**. *The dashed lines are calculated phonon dispersion curves for fcc SnTe at 300 K carried out by Andreas Hermann.*

As already mentioned for *fcc* SnTe with 2 atoms per unit cell, one would expect 6 phonon branches. Of the 6 branches 3 would be acoustic being made up of 1 longitudinal and 2 transverse modes. Similarly there would be 3 optic branches again made up of 1 longitudinal and 2 transverse modes. However due to symmetry considerations along the [1,0,0] direction the 2 transverse acoustic modes are degenerate as are the 2 transverse optic modes. This is indicated in Figure 3.4 by the presence of only 4 different measured branches along the [1,0,0].

The DFT calculations of phonon dispersion curves however show 6 branches caused by the method of calculation at finite temperature. The 6 modes are then seen as 2 non-degenerate TA and TO branches along the [1,0,0] and [1,1,1] directions as is clearly seen in Figure 3.4 and is not a loss of symmetry but an artefact of the calculation. A best estimate of the calculated phonon branch is

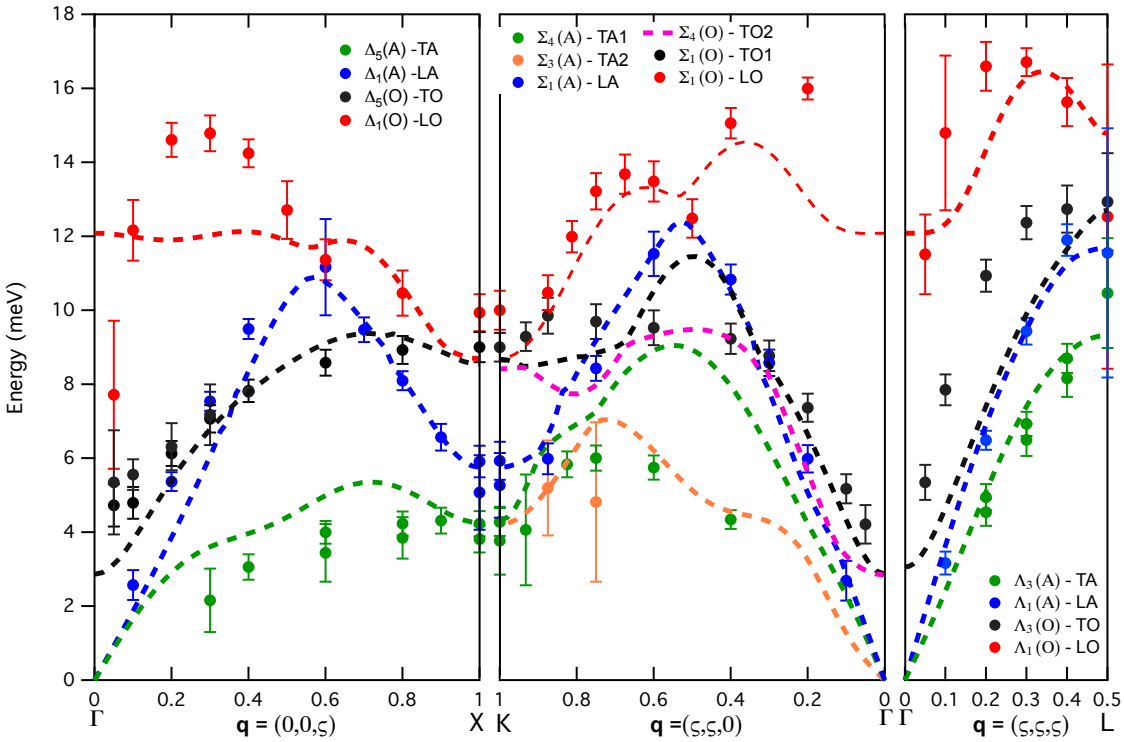

Figure 3.5: *The phonon dispersion curve energies for SnTe at 300 K in the reduced Brillouin zone with wavevector* **q** *along the 3 directions of high symmetry as already shown in Figure 3.4. The markers are again measured experimental points from the phonon creation energy transfer. The dashed lines are calculated phonon dispersion curves for fcc SnTe at 300 K carried out by Andreas Hermann. The previously 2 non-degenerate TA and TO phonon calculation branches along the [1,0,0] and [1,1,1] are now plotted as single dashed curves which are the average of the 2.*

achieved by taking the average as shown in Figure 3.5. The [1,1,0] direction does not contain the same symmetry and degeneracy however, so 6 modes are always present. Experimentally the 2 non-degenerate TA phonons can be resolved along [1,1,0] and only 1 phonon is detected for the 2 TO modes.

The sample was then cooled in a closed cycle cryostat and more constant **Q** scans carried out to measure the softening of the TO phonon as previously seen by Pawley *et al.* using neutrons. In the [1,0,0] direction the TO-phonon is seen along a **Q** propagation direction of $(3,3,1) \rightarrow (3,3,0)$. The TO phonon energy along [1,0,0] is shown in Figure 3.6 (a) for 300 K and 75 K against **q**. The markers in Figure 3.6 (a) are experimental points and the dashed lines guides for the eye.

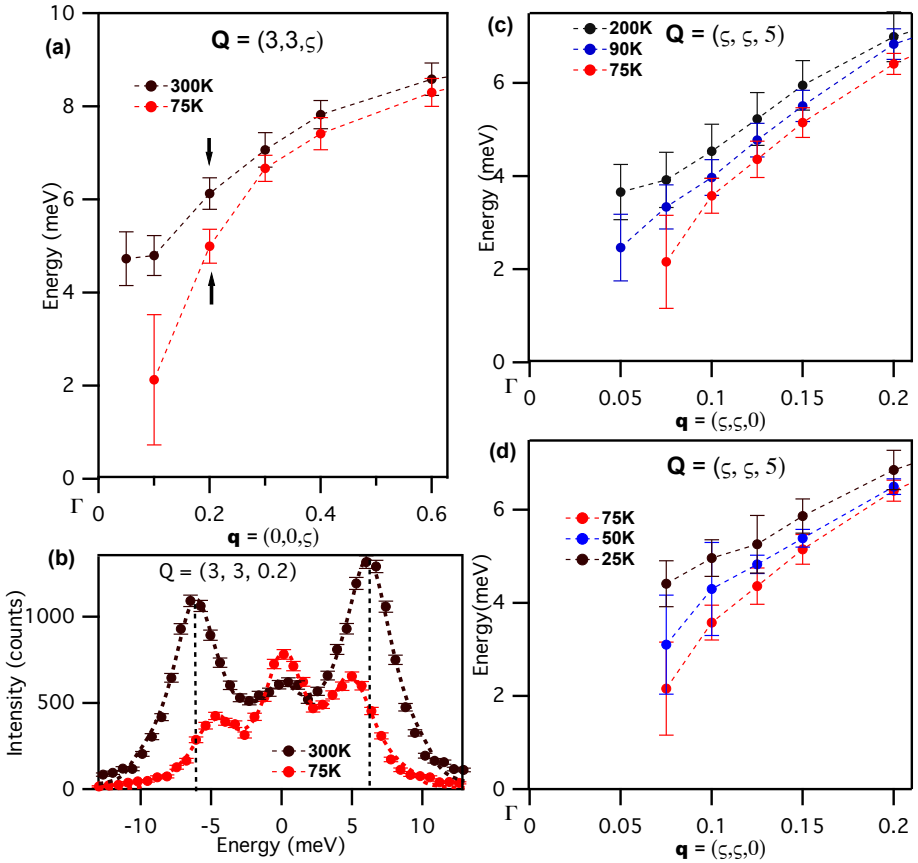

Figure 3.6: *(a) The TO phonon branch energy along [1,0,0] detected at a* $\mathbf{Q}$ *vector propagation of* $(3,3,1) \rightarrow (3,3,0)$ *plotted against reduced wave vector* $\mathbf{q}$ *at 300 K and 75 K. (b) The intensity vs energy spectra for the TO phonon at* $\mathbf{Q} = (3,3,0.2)$ *which are the data points indicated by the black arrows in (a). (c) and (d) The TO phonon along the [1,1,0] detected at a* $\mathbf{Q}$ *vector propagation of* $(1,1,5) \rightarrow (0,0,5)$ *at a range of temperatures.*

Clearly seen is a softening of the phonon upon cooling. The measured intensity vs energy spectra at 300 K and 75 K are shown as the markers in Figure 3.6 (b) for $\mathbf{Q} = (3,3,0.2)$. The $\mathbf{Q} = (3,3,0.2)$ points at 300 K and 75 K are indicated by the black arrows in Figure 3.5 (a). In the spectra shown in Figure 3.6 (b) the 3 intensity peaks already discussed are evident. The dashed lines in Figure 3.6 (b) are the calculated fits of equation 3.17 convoluted with the resolution function.

The TO-phonon energy along the [1,1,0] direction at 200 K, 90 K and 75 K is also shown in Figure 3.6 (c) where it has been seen along a $\mathbf{Q}$ propagation direction of $(1,1,5) \rightarrow (0,0,5)$. Again strong softening towards the zone centre

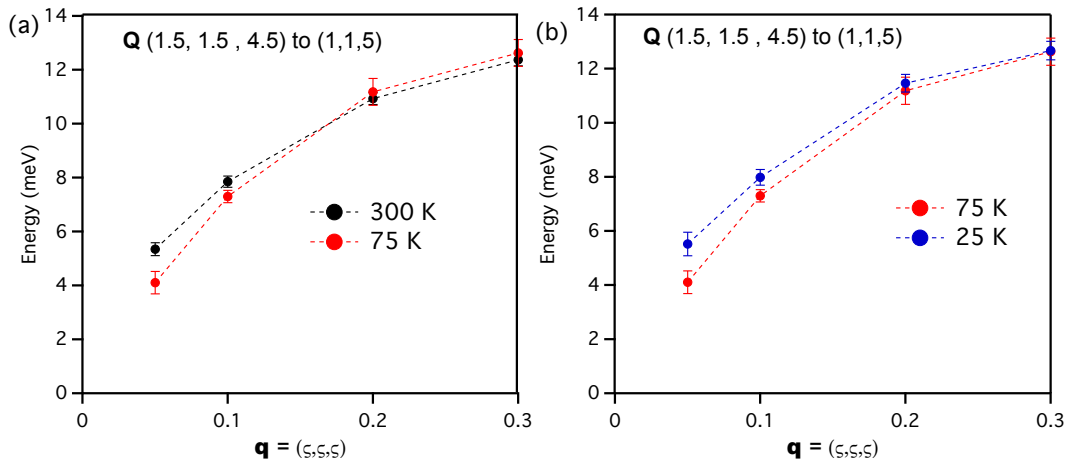

Figure 3.7: *(a) The TO phonon branch energy along [1,1,1] detected at a* $\mathbf{Q}$ *vector propagation of* $(1.5, 1.5, 4.5) \rightarrow (1, 1, 5)$ *plotted against reduced wave vector* $\mathbf{q}$ *at 300 K and 75 K. (b) The TO phonon along [1,1,1] at* T_c *= 75 K and at 25 K well below* T_c*.*

is evident. Upon further cooling below 75 K, the measured T_c by resistivity, the TO-phonon energy is seen to recover to higher values as shown in Figure 3.6 (d) for 50 K and 25 K. Figure 3.7 shows the TO phonon along the [1,1,1] direction where the $\mathbf{Q}$ propagation direction was $(1.5, 1.5, 4.5) \rightarrow (1, 1, 5)$. Figure 3.7 (a) is the measured phonon energy shown as markers against $\mathbf{q}$ for 300 K and 75 K where again softening is evident. Upon further cooling to 25 K the TO phonon is again seen to recover as shown in Figure 3.7 (b).

As well as the TO phonon measured along the [1,1,1] direction the TA phonon was also measured where the $\mathbf{Q}$ propagation direction was $(2, 2, 4) \rightarrow (1.5, 1.5, 4.5)$ for comparison. This is the direction the TA phonon is seen closest to the zone centre Γ. No change in phonon energy was seen at all temperatures measured for the TA phonon as shown in Figure 3.8. Figure 3.9 shows the measured intensity vs energy spectra as markers and calculated fits as dashed lines at $\mathbf{Q} = (0.1, 0.1, 5)$ and $\mathbf{Q} = (1.8, 1.8, 4.2)$ for the TO phonon along the [1,1,0] and the TA phonon along the [1,1,1] directions respectively. Again the 3 peaks in the spectra correspond to phonon creation, annhilation and an elastic contibution at zero energy transfer. For the TO phonon in Figure 3.9 (a) and (b) the softening is clearly seen going from 300 K to 75 K. Then at 25 K Figure 3.9 (c) phonon recovery is also clear, the vertical dashed lines are guides to the eye. The TA

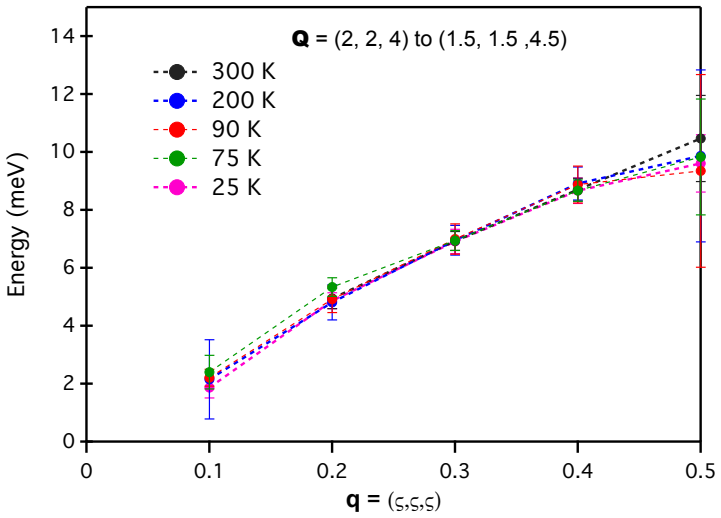

Figure 3.8: *The TA phonon branch energy along [1,1,1] detected at a* **Q** *vector propagation of* $(2, 2, 4) \rightarrow (1.5, 1.5, 4.5)$ *plotted against reduced wave vector* **q** *at* 300 K *and* 75 K. *for a wide range of temperatures.*

phonon is shown as Figure 3.9 (d) and (e) for 300 K and 75 K respectively where no change in phonon energy is detected.

As discussed in Chapter 1 approaching T_c

$$E^2 = \hbar^2\omega^2 \propto (T - T_c) \tag{3.8}$$

and below T_c

$$E^2 = \hbar^2\omega^2 \propto 2(T - T_c) \tag{3.9}$$

for a 2^{nd} order ferroelectric phase transition. Since the phonon softens towards the zone centre Γ, then ω^2 at Γ should decrease linearly to zero at T_c. After passing through the structural distortion ω^2 should then recover linearly with twice the gradient. To determine ω^2 at Γ graphs of E^2 vs $\mathbf{q}^2$ shown in Figure 3.10 were plotted since $\omega^2 \propto \mathbf{q}^2$ at low **q**. Figure 3.10 (a) shows measured points as markers for E^2 vs $\mathbf{q}^2$ at 300 K, 200 K and 90 K above T_c as well as 75 K at T_c. To deduce E^2 at Γ a line of best fit was plotted for each temperature that was extrapolated to Γ. Each fit had the gradient held constant and the intercept gave E^2 at Γ. Figure 3.10 (b) then shows the measured points as markers for temperatures below T_c. Again lines of best fit were made with a slightly lower fixed gradients than in (a) and the intercepts at Γ deduced. A graph of E^2 at

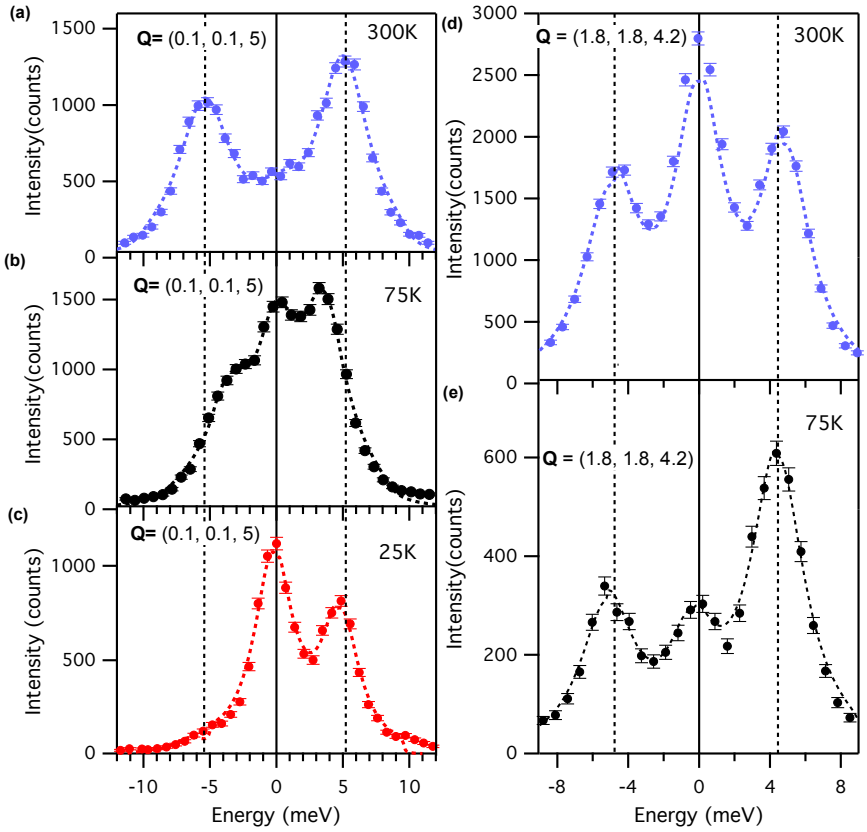

Figure 3.9: *(a)-(c) Measured intensity vs energy transfer spectra at various temperatures shown as markers at* $\mathbf{Q} = (0.1, 0.1, 5)$ *for the TO phonon propagating in the [1,1,0] direction. The dashed lines are calculated fits from a convolution of the resolution function with equation (3.7). (d)-(e) Measured intensity vs energy transfer spectra at 300 K and 75 K respectively shown as markers at* $\mathbf{Q} = (1.8, 1.8, 4.2)$ *for the TA propagating in the [1,1,1] direction. The vertical dashed lines are guides to the eye.*

Γ is shown in Figure 3.11 (a) as a function of temperature. According to Figure 3.11 (a) ω^2 decreases linearly to zero at $T_c = 75$ K as indicated by the dashed line. Below T_c there is also a linear increase of ω^2. The ratio of the gradients of the lines of best fit in Figure 3.11 (a) above and below T_c is between 1:4.8 and 1:5.

As well as the value of phonon energy $\hbar\omega$ the frequency dependent half-width at half-maximum $\Gamma(\omega)$ linewidth can be found by fitting the measured spectra according to equation 3.7. This linewidth is an indication to phonon-electron, phonon-phonon interactions etc. as already mentioned. The phonon linewidth

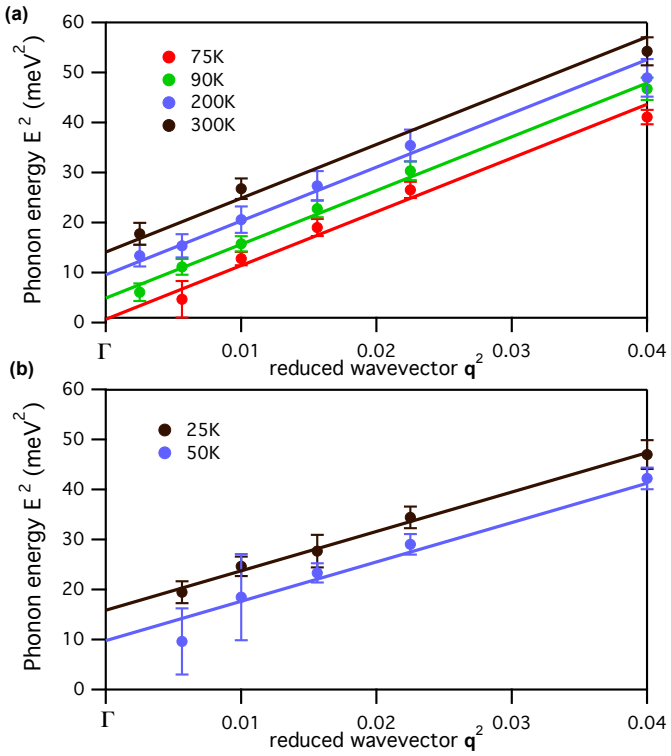

Figure 3.10: *(a) A graph of the phonon energy squared vs the* **q** *wavevector squared at various temperatures above and including* T_c *shown as markers. Lines of best are also plotted and extrapolated to* Γ*. (b) Is also a graph of the phonon energy squared vs the* **q** *wavevector squared for temperatures below* T_c *along with lines of best fit.*

for the TO phonon at $\mathbf{Q} = (0.1, 0.1, 5)$ and $\mathbf{Q} = (0.125, 0.125, 5)$ close to the zone centre is shown in Figure 3.11 (b) as a function of temperature. For comparison the phonon linewidth for the TA phonon at $\mathbf{Q} = (0.2, 0.2, 0.2)$ is also plotted in Figure 3.11 (c). T_c is indicated by the dashed vertical. A sharp drop in phonon linewidth is measured for temperature below T_c. How the linewidth changes with **q** is shown in Figure 3.12 for various temperatures. Figure 3.12 (a) and (b) show the linewidth increasing almost linearly going from the zone edge to the zone centre along the [1,1,0] direction at 300 K and 75 K respectively. At 25 K the linewidth stays almost constant at all **q** measured shown in Figure 3.12 (c).

Various phonon branches not just the TO and TA were also measured at T_c = 75 K to detect any other possible anomalies occuring upon entering the rhombohedral phase. The data is shown as the markers in Figure 3.13. Scalar-relativistic density functional theory calculations for the ground state 0 K

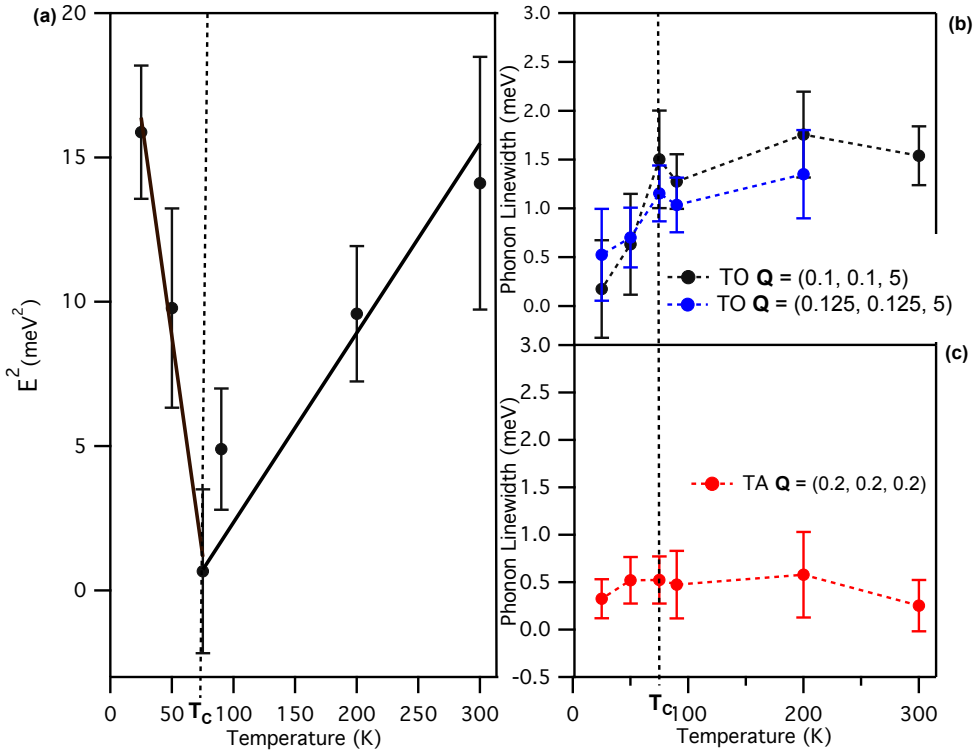

Figure 3.11: *(a) A graph of the estimated energy squared (E^2) at the zone centre* Γ *as against temperature. The solid lines are lines of best fit with a gradient ratio of 1:5 above and below* T_c*. (b) The variation of the TO phonon linewidth with temperature at* $\mathbf{Q} = (0.1, 0.1, 5)$ *and* $\mathbf{Q} = (0.125, 0.125, 5)$*. (c) The variation of TA phonon linewidth with temperature at* $\mathbf{Q} = (0.2, 0.2, 0.2)$*.*

rhombohedral phase carried out by Andreas Hermann are also included as the dashed lines for comparsion. In the rhombohedral phase the high symmetry degeneracy would be lifted from the transverse modes in the [1,0,0] direction and all 6 phonon branches would occur at different energies. The calculations for the rhombohedral phase show all 6 branches however not enough data was collected in the experiment to measure all branches.

Connection can be made between the long wavelength acoustic phonons, where the wavelength is much larger than the size of the unit cell, and the macroscopic elastic properties of the crystal. By considering the motion of the atoms associated with the acoustic phonon branch one can then picture the compressional or shear strain it causes the crystal structure. For example in a longitudinal acoustic mode in a cubic crystal with wave vector along [1,0,0], each

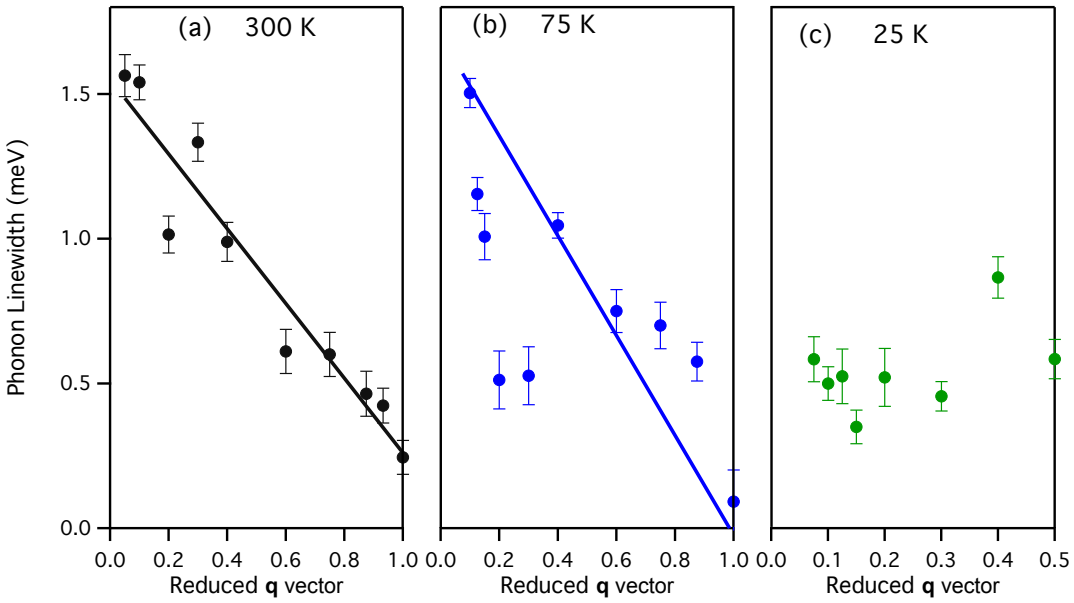

Figure 3.12: *(a)-(c) Phonon linewidths widths determined from the fits to intensity vs energy spectra against reduced wavevector* $\mathbf{q}$ *for various temperatures. The lines of best fit are just guides to the eye.*

Temperature (K)	C_{11} (kbar)	C_{12} (kbar)	C_{44} (kbar)	B (kbar)	ν
300 - Experiment	992 ± 34	75 ± 10	93 ± 9	380	0.386
300 - Calculation	838 ± 17	110 ± 09	150 ± 5	353	0.313
75 - Experiment	1042 ± 48	62 ± 10	90 ± 15	389	0.392

Table 3.2: A table of elastic constants derived from both experiment and calculations. Also included is the Bulk modulus, B, and Poisson's ratio ν.

(1,0,0) plane is displaced in the x direction by a constant amount relative to its neighbouring planes. Therefore the displacement u_x of each plane is proportional to its position x. This corresponds to a uniform compressional strain of the crystal as explained in Chapter 7 of the text by Dove [21].

When all symmetry is considered each acoustic mode frequency ω relates to the displacement by

$$\rho\omega^2\tilde{\mathbf{u}} = \mathbf{M}\cdot\tilde{\mathbf{u}} \tag{3.10}$$

where ρ is the density of the material, $\mathbf{M}$ is a dynamical matrix and the acoustic modes propagate as $\mathbf{u}(t) = \tilde{\mathbf{u}}\exp(i[\mathbf{k}\cdot\mathbf{r} - \omega t])$. Then $\rho\omega^2$ are eigenvalues of the dynamical matrix and the eigenvectors give the corresponding motions. The

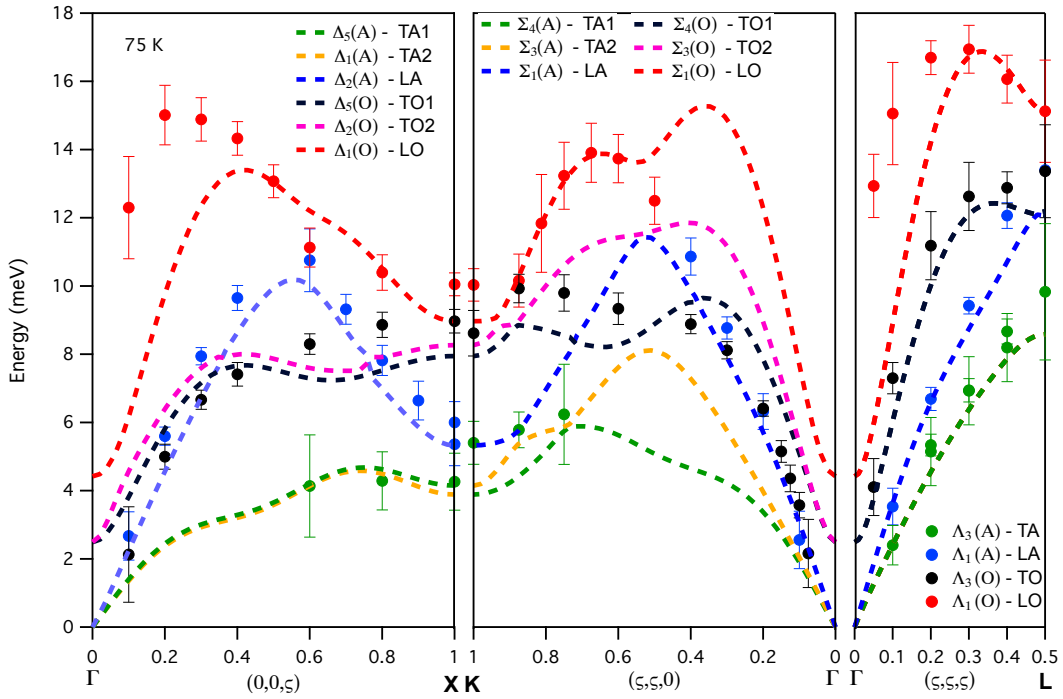

Figure 3.13: *Phonon dispersion curve energies for SnTe at 75 K in the reduced Brillouin zone with wavevector* **q** *along the 3 directions of high symmetry. The markers are measured experimental points from the phonon creation energy transfer in the intensity vs energy spectra carried out at constant* **Q**. *The dashed lines are calculated phonon dispersion curves for rhombohedral SnTe at 0 K carried out by Andreas Hermann.*

dynamical matrix is of the form

$$M_{ik} = \sum_{i,j} C_{ijkl} k_j k_l \tag{3.11}$$

and hence the elastic constants, C, which are 4^{th} rank tensors, can be calculated. Symmetry cancels a lot of components and the symmetrical dynamical matrix for a cubic material has 3 different components C_{11}, C_{12} and C_{44}. The constant C_{11} is an axial compression such as the longitudinal acoustic uniform compression example given above. The C_{44} is a shear stress such as a shear in the [1,0,0] direction caused by a transverse phonon in the [0,1,0] direction. The C_{12} is the modulus for dilation on compression, such as an axial stress in one direction causing a strain in a perpendicular axis. A table of each acoustic modes atomic motion and the corresponding combination of elastic constants is also shown in

Branch	v [1,0,0] m/s	v [1,1,0] m/s	v [1,1,1] m/s
Longitudinal 300 K	3931	4419	4861
Longitudinal 75 K	4118	4542	4943
Transverse 300 K	1026	1527	3457
Transverse 75 K	-	-	3710

Table 3.3: A table of the speed of sound in longitudinal and transverse directions for each high symmetry direction calculated from the acoustic phonons in SnTe

Dove [21]. Using the frequency of the acoustic phonon branches in the long wavelength limit, $\mathbf{q}$, and density of SnTe, ρ, values of elastic constant were calculated for this experiment. The values are shown in Table 3.2. Included in Table 3.2 is the bulk modulus B given by

$$B = \frac{C_{11} + 2C_{12}}{3} \tag{3.12}$$

for a cubic material. Also shown is the Poisson's ratio, ν, estimated by the equation

$$\nu = \frac{3B - 2G}{6B + 2G} \tag{3.13}$$

where G is the shear modulus in this case equal to C_{44}. The speeds of sound, v, equal to $\partial\omega/\partial\mathbf{q}$ for each acoustic phonon that data is available for are also shown in Table 3.3.

3.3 Discussion

The phonon dispersion curves in fcc SnTe at 300 K were successfully measured along all high symmetry directions in the Brillouin zone shown in Figure 3.4. The curves are labelled by their group symmetry notation $\Delta_5(A), \Delta_1(O)$ etc. which describes the symmetry of the atomic motion. The DFT calculations carried out by Andreas Hermann show good agreement with the data points in Figure 3.3, although a pronounced splitting of the degenerate transverse modes along [1,0,0] is present caused by an artefact of the high temperature calculation. By taking the average of the splitting as a good estimate shown in Figure 3.5, better agreement is seen. Comparison of the elastic constants between the calculation and experiment which are shown in Table 3.2 also show very good agreement. Both experiment

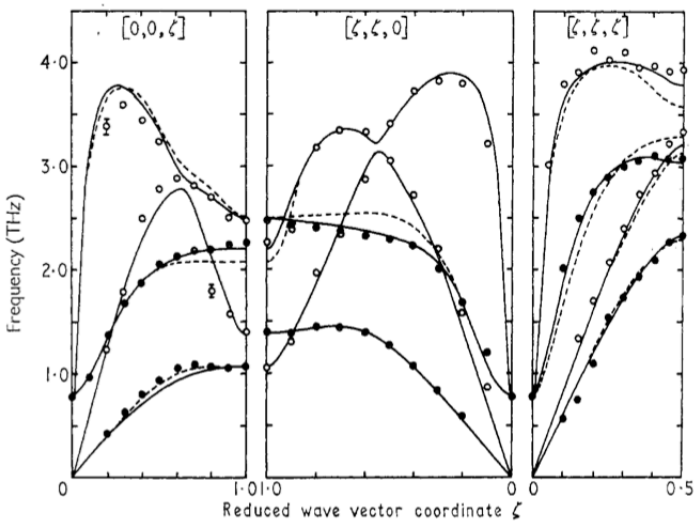

Figure 3.14: *The phonon dispersion results of Cowley et al [27]. The solid markers indicate transverse modes while the open markers longitudinal. These results agree well with ours in Figure 3.4, direct comparison of scales is given by* $4.13\ meV = 1\ THz$.

and calculation agree well with the previous experiment carried out by Cowley *et al*. shown in Figure 3.14 in terms of both energy and branch shape.

Upon cooling the TO-phonon curve was seen to strongly decrease in energy i.e. soften, towards the zone centre shown in Figures 3.6 and 3.7. This has been previously seen in the results of Pawley *et al*. [25] as shown in Figure 1.7. In Pawley *et al.'s* results the TO phonon decreases in energy towards the zone centre for all temperatures to 6 K. However the energy never reached zero indicating it was only approaching a ferroelectric transition. The energy at the zone centre, Γ, in our experiment was estimated from the linear plots of E^2 vs $\mathbf{q^2}$ shown in Figure 3.10. From the plots it is clear at 75 K the energy of the TO phonon at Γ reaches zero. The resistivity curve of the sample measured in this experiment also showed an anomaly at 75 K associated with the structural transition. We can then conclude at 75 K the sample has passed through a phase transition.

The nature of the phase transition is the most interesting point. Many previous experiments have noted SnTe has gone through a structural distortion as discussed at length in Chapter 1. Changes in peak intensity in neutron scattering [30] and peak splitting in X-ray scattering [28] indicate a transition has taken place. But the results reported here are the first proof that the transition is ferroelectric in nature. After the phonon energy has decreased to zero at T_c,

at temperatures below T_c of 50 K and 25 K the measured TO phonon branch recovered to higher energies, shown clearly in Figure 3.6 (d). The energy at Γ vs temperature is shown in Figure 3.11 (a) where a linear decrease to T_c is followed by a linear increase below T_c. The ratio of the slope of the two lines above and below T_c is between 1:4.8 and 1:5. The Landau theory discussed in Chapter 1 gives a linear decrease to zero in a 2^{nd} order transition followed by a linear recovery with twice the slope. However this is only valid for temperatures near T_c whereas the data shown here is for a temperature range of 275 K. The transition is still clearly 2^{nd} order even though the slopes don't exactly match that of Landau theory. This would agree with the previous measured specific heat data by Hatta and Kobayashi [35] discussed in Chapter 1, who also seen the transition to be 2^{nd} order.

The recovered phonon then clearly represents a frozen in co-ordinate and a displacive transition. A polar axis has also formed and the transition is ferroelectric. The symmetry is then lowered by the displacement which as discussed in Chapter 1 is along the [1,1,1] direction and a rhombohedral angle below 60° is present. No previous reports of ferroelectricity have been measured in SnTe. Attempts by Salje *et al.* [36] on samples with a lower n than our samples were drowned out by the large number of free carriers. Even though the conductivity of SnTe is high for all temperature it is still a semi conductor from all previous experimental evidence. It is then a degenerate semi-conductor with the high number of carriers making it look metallic. Most well known ferroelectrics are much more insulating than SnTe allowing for polarisation to be measured. No attempts were made on our samples to measure ferroelectricity.

The TA phonon along the [1,1,1] direction was also measured at all temperature ranges as shown in Figure 3.8. There were no signifcant changes seen, within error, in the TA phonon at any measured temperature. The behaviour seen in the TO phonon was then not caused by a change in instrument resolution or sample environment etc.. There were also no signifcant changes seen in any of the elastic constants above and at T_c as shown in Table 3.2. This agrees with the previous results of Salje *et al.* [36] who only seen a small kink at T_c. The relevance of the changes in in phonon linewidth below T_c shown in Figure 3.11 and 3.12 are postponed to be discussed in Chapter 4 where more data relating the effective mass, m^*, with and without the structural distortion was acquired.

Chapter 4

High Pressure Studies of SnTe

This chapter discusses transport measurements on SnTe carried out under high hydrostatic pressures. First a brief discussion of previous high pressure experiments is given. This is followed by a description of the technique used to measure transport properties in diamond anvil cells. Resistivity, Hall effect and quantum oscillation results are then discussed at various pressures.

4.1 Introduction and Technique

The purpose of the investigation carried out in this chapter was to see how the ferroelectric transition and carrier concentration in SnTe varies with high hydrostatic pressure. The surface state in SnTe predicted by T. Hsieh *et al.* [11] and seen experimentally by Tanaka *et al.* [10], above T_c, is protected by the mirror symmetry of the fcc phase as discussed in Chapter 1. Below T_c the ferroelectric transition would then lower the crystal symmetry acting to destroy some of the surface states. Using the anomaly associated with T_c in the resistivity its pressure dependence was tracked. Above 6 kbar the ferroelectric phase was suppressed. A two component Hall response also becomes apparent under high pressure. The results of the investigation are given in Section 4.2 along with a full discussion in Section 4.3. A brief review of the previous high pressure work carried out on SnTe and the techniques used make up the remainder of this section.

Following an extensive search of the literature, there have been no reports of a high pressure experimental investigation of the ferroelectric transition in SnTe. Kafalas and Mariano [54] have however investigated the crystal structure of SnTe

to 50 kbar at constant temperature (assumed room temperature). The sample was large and cylindrical with a 1.5 mm radius and 20 mm length. They used a belt high pressure apparatus (this type of apparatus is described in the paper by Hall [55]), that allowed pressure to be applied to such a large sample. A pressure transmitting medium (PTM) of solid NaCl was used to ensure a hydrostatic distribution of pressure. Kafalas and Mariano found a structural transition at 18 kbar from the fcc phase to a orthorhomic structure of space group $Pnma$ that coincided with a 360% increase in sample resistance. More recently Zhou *et al.* [56] carried out an investigation of the high pressure phases of SnTe with a diamond anvil cell and silicone oil PTM. Using X-ray diffraction, at 300 K, Zhou *et al.* found the fcc phase was stable to 41 kbar. Above 41 kbar a transition to an orthorhombic phase was measured, which was 1^{st} order in nature. The results presented here are only carried out to 22 kbar where there is no evidence of a cubic to orthorhombic transition, as shall be discussed further in Section 4.3.

Pressure was applied in this investigation using a diamond anvil cell received from Konstantin Kamenev, Edinburgh, and is shown in Figure 4.1. A diamond with a 800 μm culet was glued in place using black stycast 2850 FT epoxy to a hardened BeCu nut as shown in Figure 4.1 (a). The nut was then screwed into the bottom of the hardened BeCu body of the cell and tightened. Another diamond with a 800 μm culet was stycast to the grooved BeCu cylinder. This cylinder passed through the top of the cell body using the threaded bar shown in Figure 4.1 (b) along with several washers, spacers and a top locking nut. The two culets were then aligned under a microscope until they were completely parallel. To contain the sample a gasket was made from 300 μm thick steel that was indented to 150 μm within the pressure region. A hole of 400 μm was drilled in the steel and the gasket placed between the opposing diamonds. Pressure could be applied by tightening the top locking nut while holding the cell body in a vice. A washer with bearings was used so when tightening the top locking nut the grooved cylinder and top diamond would also not turn. A plastic spacer was used to help with drops in pressure due to thermal contraction. A schematic of the entire cell including the gasket is shown in Figure 4.1 (b).

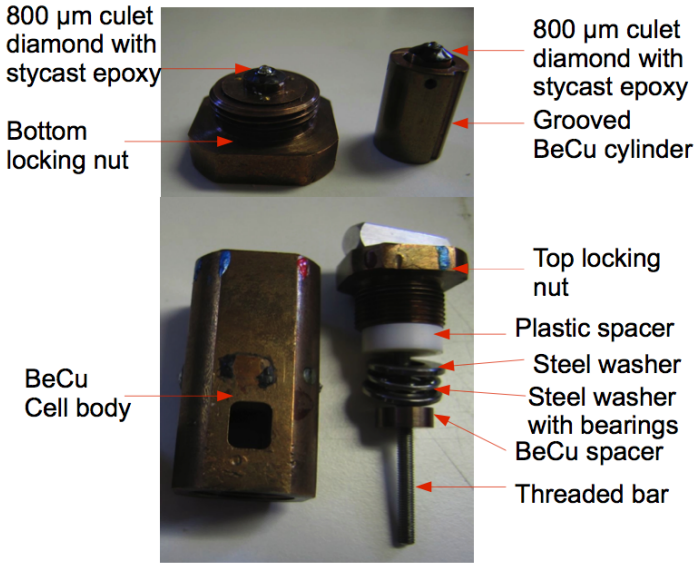

(a)

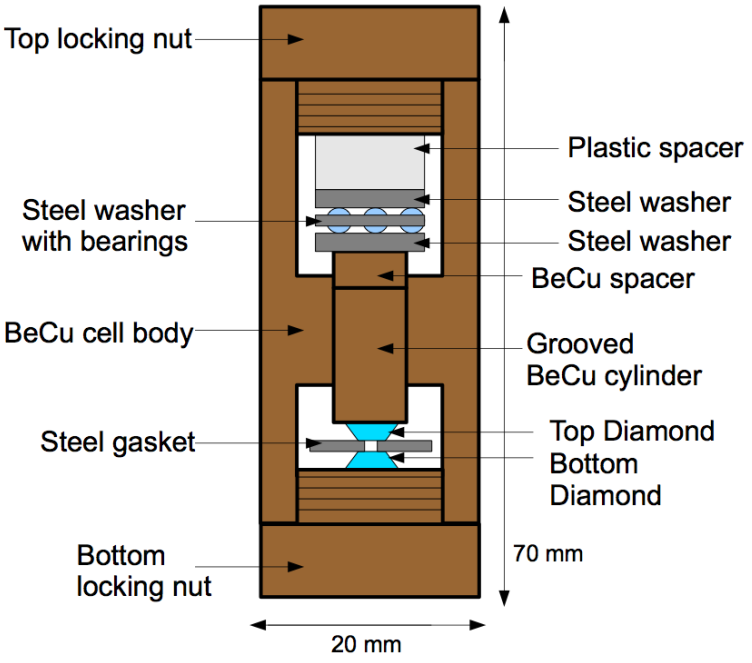

(b)

Figure 4.1: *A Picture of the diamond anvil pressure cell received from Konstantin Kamenev used in this investigation is shown in (a) while a schematic is shown in (b)*

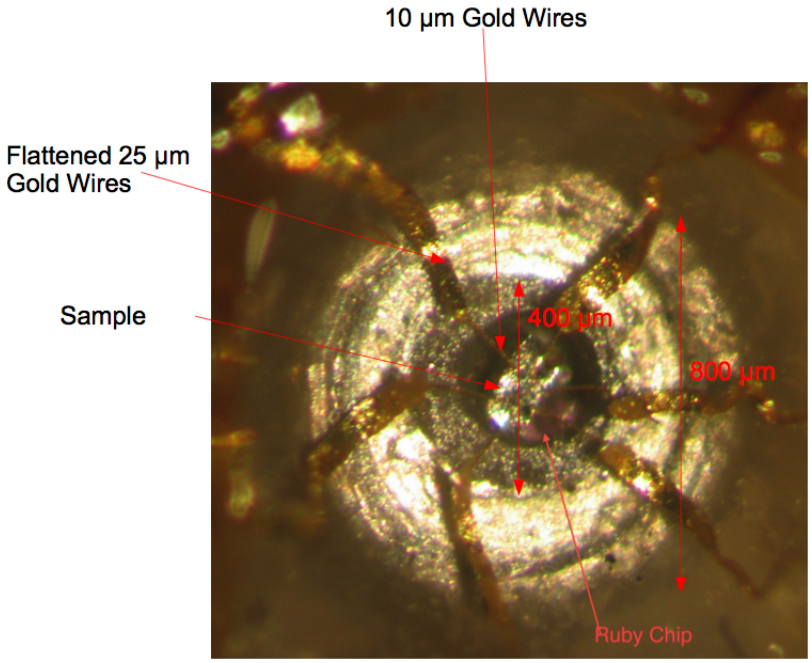

(a)

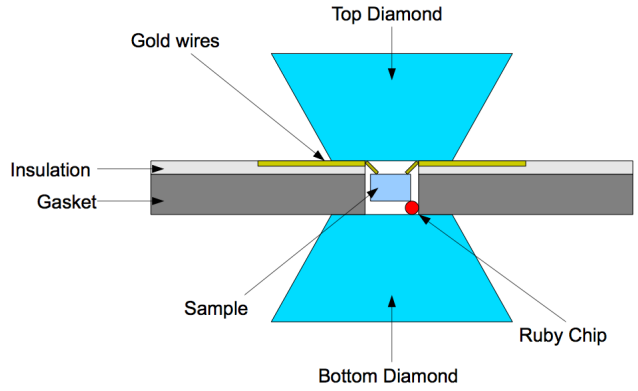

(b)

Figure 4.2: *(a) A picture of the sample within the gasket hole. The white material is the insulation covering the steel gasket. The ruby used for pressure determination is pointed out. (b) A schematic of the sample in the gasket held between the two opposing diamonds.*

To insulate the sample from the gasket so electrical contact could be made to the sample insulation was made from 1266 white stycast epoxy and aluminium (III) oxide powder was mixed in a weight ratio of 50:50. A thin layer of the mixture was added the top surface of the gasket and filled the hole. The cell

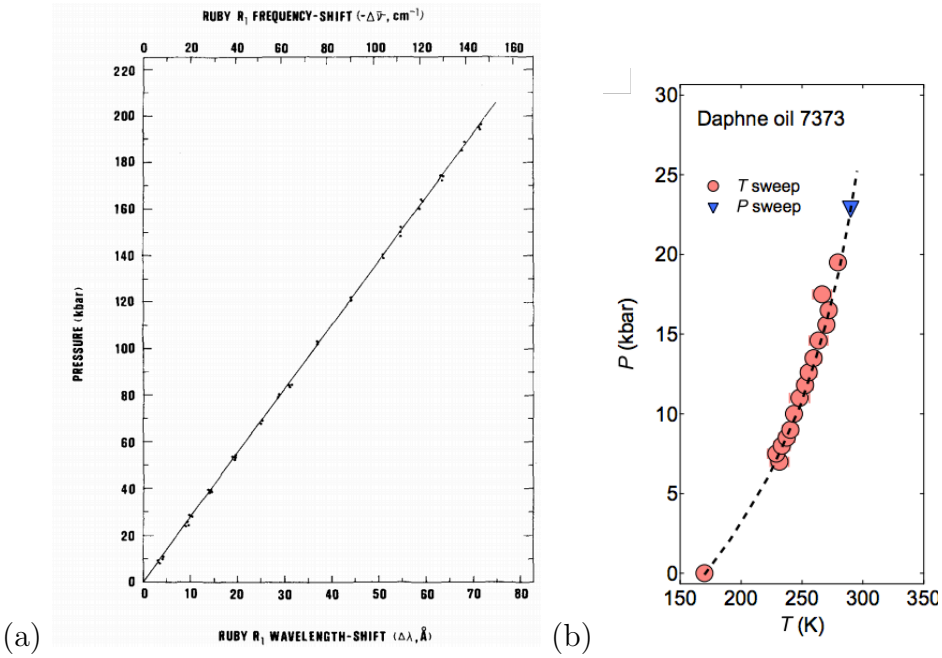

Figure 4.3: *(a) The results of Piermarini et al. [57] showing the spectral shift of the sharp fluorescence R1 line in ruby with pressure. (b) The results of Imura et al. [58] showing the freezing temperature of Daphne oil 7373 as a function of pressure.*

was closed until the insulation thickness reached 60 μm. A hole was then drilled in the insulation of 250 μm so when the sample was placed within the hole it was completely insulated from the gasket. The SnTe sample chosen was a single crystal of length 220 μm, width 150 μm and thickness 135 μm from growth 3 and is shown inside the insulated gasket in Figure 4.2 (a). A schematic of the sample inside the gasket hole is also shown in Figure 4.2 (b). Laue diffraction was carried out beforehand and showed the [1,0,0] direction was along its thickness while the [0,1,0] and [0,0,1] directions were along the width and length respectively.

Six 10 μm gold wire contacts were added to the sample such that the current was applied along the [0,0,1] direction. The other 4 contacts were then voltage contacts along the length and across the width of the sample, so both the Hall effect and magnetoresistance was measured. Contact to the 10 μm wires was then achieved by using larger 25 μm gold wires as shown in Figure 4.2 (a), that were flatted at one end and cut into sharp points using a razor blade. These wires were then split into twisted pairs of current and voltage contacts. To determine the pressure a chip of ruby was placed within the sample space as is pointed

out in Figure 4.2 (a). The spectral shift of the sharp fluorescence lines in ruby varies linearly as a function of pressure as described by Piermarini *et al.*. [57]. The result of Piermarini *et al.*. is shown in Figure 4.3 (a) carried out at room temperature. Using Raman spectroscopy a ruby fluorescence line at 694.23 nm was observed for the ruby chip located within our sample space at 297 K. This fluorescence line is denoted R1 and the pressure was then calculated from its shift at 297 K for all measurements.

The PTM was then added to the gasket hole to make the pressure distribution as hydrostatic as possible. Originally a mixture of methanol:ethanol 4:1 was used since the FWHM of the R1 line has been reported to be less than 0.2 nm at 50 kbar and 77 K by Tateiwa and Haga [59]. A small FWHM would indicate a very hydrostatic distribution of pressure. However due to its quick evaporation rate at room temperature and the time required to close the cell its use became impractical. Instead Daphne oil 7373 was used as a PTM although it has a FWHM of 0.5 nm at 50 kbar and 77 K as reported by Tateiwa and Haga [59]. Upon cooling the Daphne oil froze at a temperature which was pressure dependent. The freezing point of Daphne oil 7373 as a function of pressure is shown in Figure 4.3 (b) taken from Imura *et al.* [58].

After filling the pressure space with Daphne oil 7373 the cell was closed and the top nut tightened to apply pressure. A shift in the R1 line corresponding to 6 kbar was observed. The cell was then cooled to 2 K in the closed cycle refridgerator described in Chapter 2 and resistivity of the sample was measured using a 300 μA current applied at 23 Hz. A calibrated cernox thermometer was firmly bolted to the body of the cell. Heating and cooling was done at slow rates of 0.2 K/min to make sure of a good thermal exchange between the sample and helium gas. Field sweeps were also carried out from $\pm$9 T to measure the Hall voltage and magnetoresistance.

Attempts were made to measure the pressure at low temperature by using an optical fibre but these proved to be unsuccessful. Following each heating and cooling cycle the R1 ruby line was remeasured at 297 K to see if the pressure had changed. After the thermal cycling at 6 kbar the pressure of the sample remained the same. It was then placed in the dilution refridgerator system in Edinburgh so lower temperatures and higher fields could be reached in an attempt to measure quantum oscillations. The pressure was again remeasured after this

further thermal cycling and remained at 6 kbar.

The dilution refridgerator comes from Cryogenic Ltd. and reaches a base temperature of 20 mK by using He^3 and He^4 within its mixing chamber. The cell is then attached using a OFHC bracket, to a high thermal conductivity silver probe that makes contact with the mixing chamber. The hardened BeCu the cell was contructed from does not have a particularly high thermal conductivity so care was taken to make sure sufficient time was given for it to thermalise. A calibrated ruthenium oxide thermometer was attached to the cell and its reading was used for sample temperature estimation. The dilution fridge contains a 14 T superconducting magnet of which the sample had been measured to be in the field centre of. Field ramps from ± 14 T were carried out at a slow rate of 0.02 T/min to accurately measure quantum oscillations, shown in section 4.2.

Higher pressures of 10 kbar were also measured first to from 300 K - 2 K to measure resistivity then removed and placed in the dilution fridge to measure quantum oscillations. Upon thermal cycling an increase of pressure was measured of 3 kbar in the R1 ruby line at 297 K. Before each cool down the pressure was then set as accurately as possible to 10 kbar at 297 K. In other higher pressures of 17 kbar and 22 kbar similiar drifts in pressure were measured upon thermal cycling.

4.2 Results

The resistivity curves at each measured pressure are shown in Figure 4.4 (a), (d), (g) and (j), calculated from the geometric factors. The anomalies indicated by the black arrows correspond to the freezing of the Daphne oil PTM. The freezing temperatures agree well with those previously seen by Imura *et al.* [58] at the same pressures shown in Figure 4.3 (b). Since the contacts may move as the pressure is increased, graphs of the resistivity normalised with the value at 300 K were also plotted in Figure 4.4 (b), (e), (h) and (k). To obtain the resistivity at 300 K a straight line is fitted to the region between 150 - 230 K and extrapolated to 300 K. This is to avoid any inaccuracy caused by the anomaly associated with the Daphne oil freezing. The fits are shown as the dashed lines in Figure 4.4 (b), (e), (h) and (k). The residual resistivity normalised to the resistivity at 300 K for each pressure is shown in Table 4.1. To detect the structural transition the

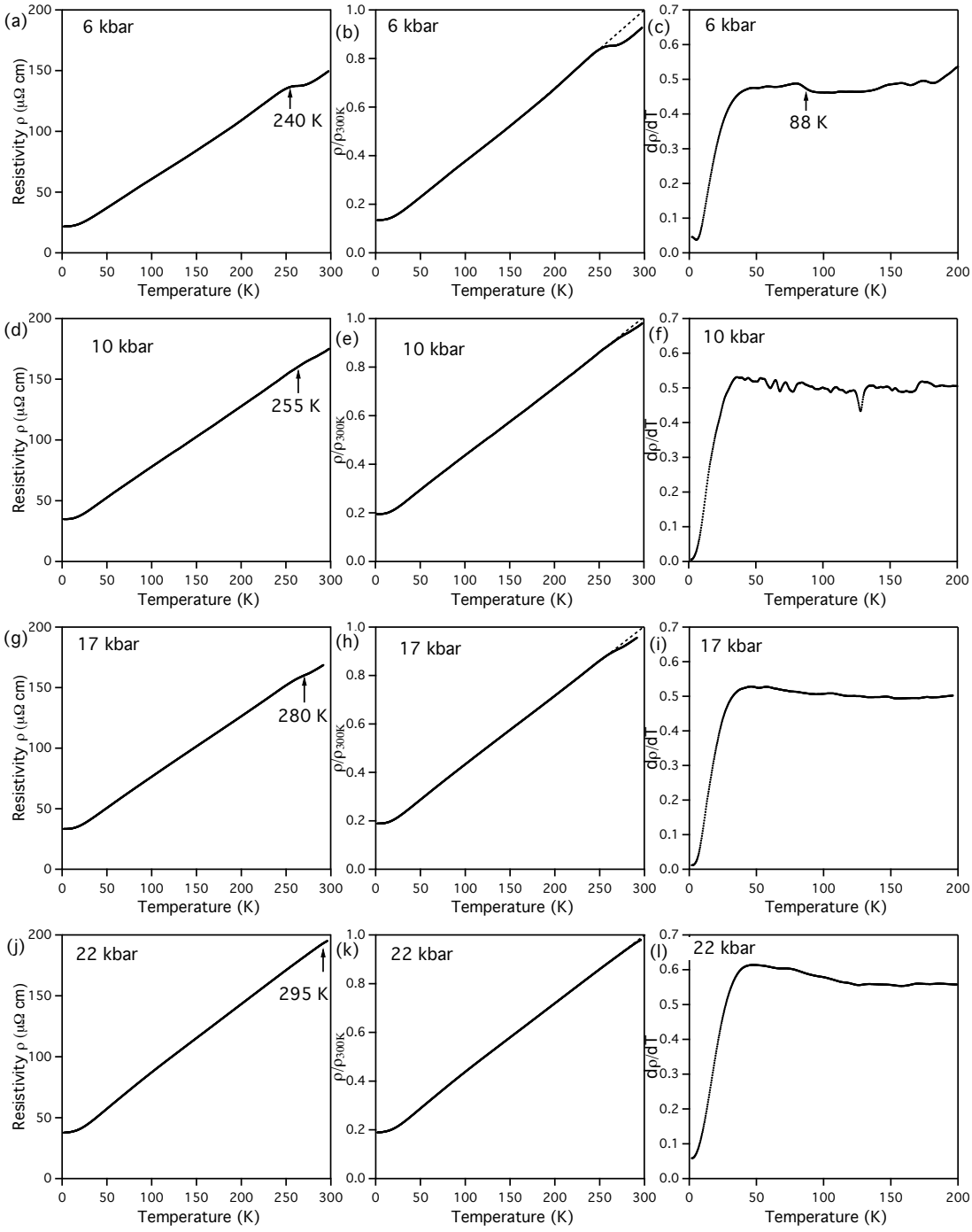

Figure 4.4: *(a), (d), (g) and (j) Resistivity curves at various pressures to 2 K. The black arrows indicate Daphne oil 7373 freezing temperature. (b), (e), (h) and (k) Resistivity curves normalised to the resistivity at 300 K at various pressures. (c), (f), (i) and (l) Graphs of the resistivity ρ differentiated with respect to temperature at various pressures.*

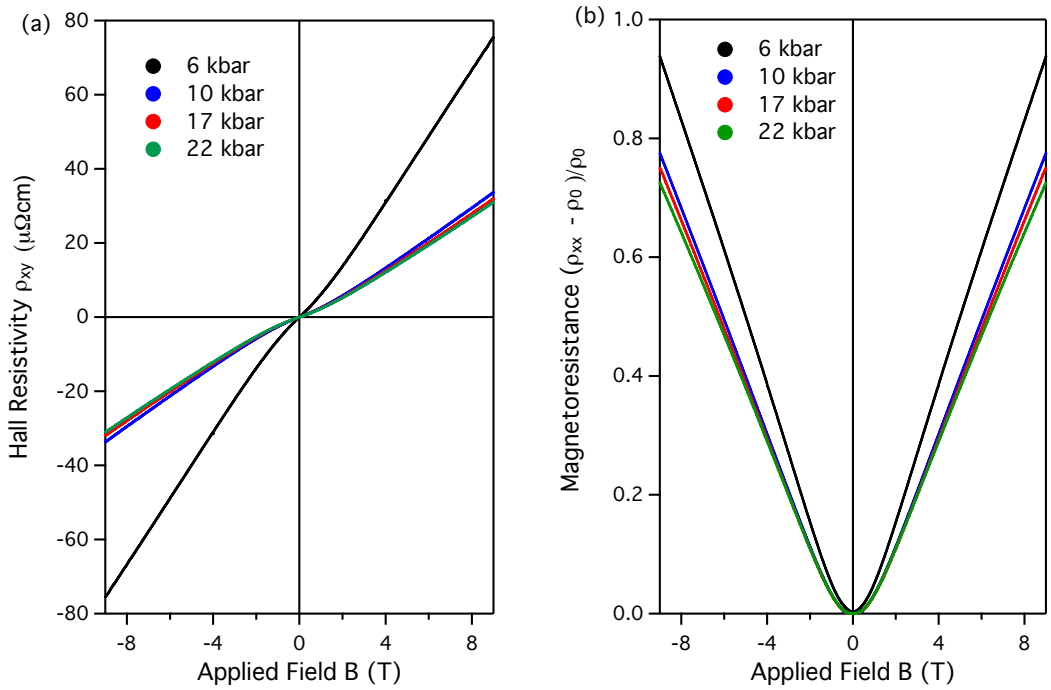

Figure 4.5: *(a) The anti-symmetrised measured Hall resistivity at 2 K for each pressure to 9 T (b) The magnetoresistance, symmetrised, at 2 K for each measured pressure.*

resistivity curves were differentiated with respect to temperature between 2 - 200 K well away from the Daphne oil freezing. These curves are shown in Figure 4.4 (c), (f), (i) and (l). A change in slope corresponding to a $T_c = 88$ K at 6 kbar is shown in Figure 4.4 (c). However at the higher pressures measured no such anomaly was detected.

Pressure (kbar)	ρ_{2K}/ρ_{300K}	$n \times 10^{20}$ cm^{-3}
6	0.134	0.70 ± 0.05
10	0.195	1.51 ± 0.05
17	0.188	1.59 ± 0.05
22	0.189	1.63 ± 0.05

Table 4.1: A table of the resistivity at 2 K, ρ_{2K}, normalised to the resistivity at 300 K, ρ_{300K}, and the carrier concentration n for each pressure.

The Hall resistivity and magnetoresistance for each pressure was measured to 9 T shown in Figure 4.5 at 2 K. Both positive and negative field sweeps allowed

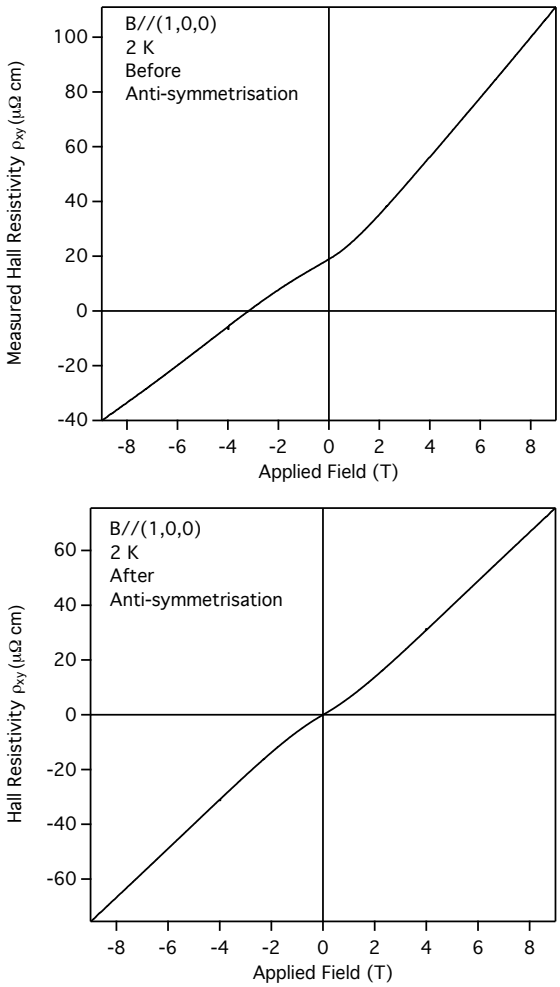

Figure 4.6: *(a) The measured raw Hall resistivity at 6 kbar and 2 K showing misalignment of the contacts has occurred (b) The Hall resistivity after anti-symetrization according to equation (2.3).*

for symmetrisation and anti-symmetrisation of the magnetoresistance and Hall signals using the resistivity tensor described previously in Chapter 2. As an example the raw curve of Hall resistivity at 6 kbar and 2 K is shown in Figure 4.6 (a) without any anti-symmterisation. A field of almost -3.2 T was required to produce zero Hall resistivity. Anti-symmetrisation was then carried out as before using equation (2.3) and the anti-symmetrized curve is shown in Figure 4.6 (b). The carriers are holes throughout all measurements. The values of n are also shown in Table 4.1 deduced from the slope of the linear part at higher fields in each Hall curve.

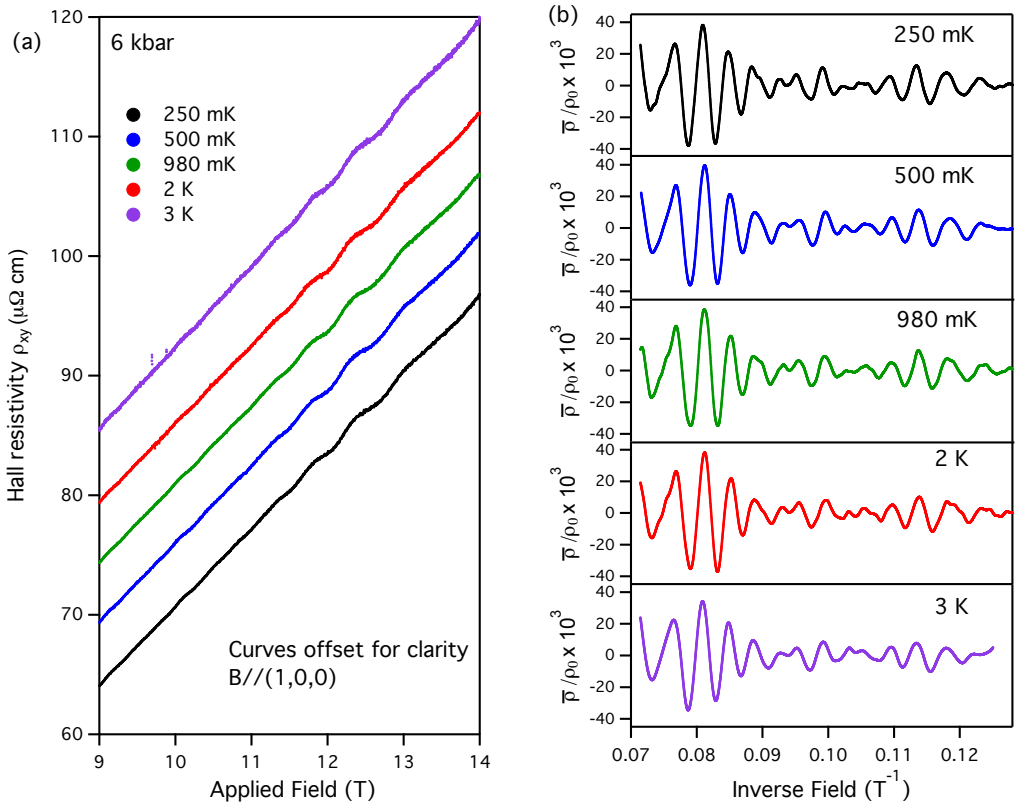

Figure 4.7: *(a) The measured Hall signal at 6 kbar for various temperatures clearly displaying quantum oscillations. The field has been applied along the (1,0,0) direction of the crystal. (b) Plots of the oscillation amplitude $\overline{\rho}$ after a smoothly varying background has been subtracted normalised to the zero field resistivity ρ_0 against inverse field.*

Quantum oscillations were then measured to 14 T in the dilution fridge set up where the field direction was parallel to the (1,0,0) direction in the sample. The oscillations are evident in the hall signal shown in Figure 4.7 (a). A smoothly varying polynomial background is again subtracted to reveal the oscillation amplitudes, $\overline{\rho}$, which are plotted against inverse field in Figure 4.7 (b) for various temperatures. Again the temperature dependence of the oscillations was used to calculate the effective mass. The amplitude only decreases slightly over the temperature range measured. Due to the calibration of the thermometry it was not possible to measure accurately field sweeps above 3.5 K. However effective masses between of $m^* = 0.23$-$0.25\ m_e$ where determined from the fits shown in

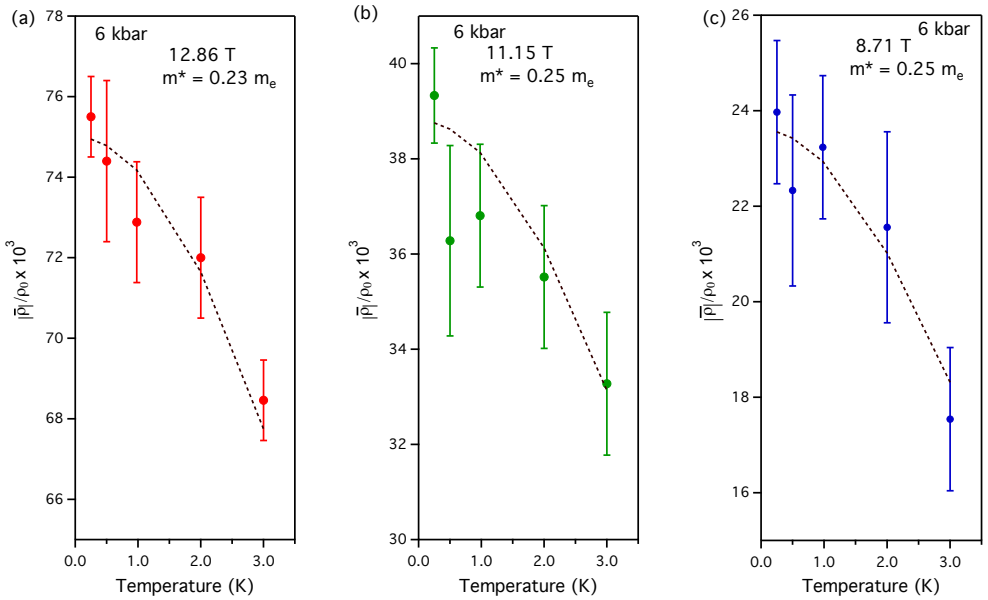

Figure 4.8: *(a)-(c) The magnitude of the amplitude of oscillations* $|\,\overline{\rho}\,|/\rho_0$ *against temperature at for 3 fields, shown as markers. The dashed lines are fits to equation 4.1 in order to determine the effective mass* m^*.

Figure 4. 8 (a) - (c). The fits are equal to

$$\frac{|\,\overline{\rho}\,|}{\rho_0} \propto R_T \propto \frac{\alpha m^* T/B}{\sinh(\alpha m^* T/B)} \tag{4.1}$$

as disussed in Chapter 2. The effective mass was then determined to be $0.25 \pm 0.03\ m_e$. The FFT tranform of the oscillations interpolated to 5000 points with inverse field was then carried out shown in Figure 4.9. The same method of using the Hanning window and padding with 100,000 zeros was used as before in Chapter 2. There are still clearly 4 sharp peaks in the FFT at all temperatures. The smaller peaks above 300 T are equal to twice the frequency of the 4 main peaks as a result of the beating of the oscillations. The Dingle temperature was then estimated using the equation

$$\frac{|\,\overline{\rho}\,|}{\rho_0} \propto R_D \propto \frac{1}{B^2} \exp\left(\frac{-\alpha m^* T_D}{B}\right) \tag{4.2}$$

as was done before in Chapter 2. The oscillations at 250 mK are shown in Figure 4.10 (b). To try and replicate this field dependence, 4 cosine waves were summed

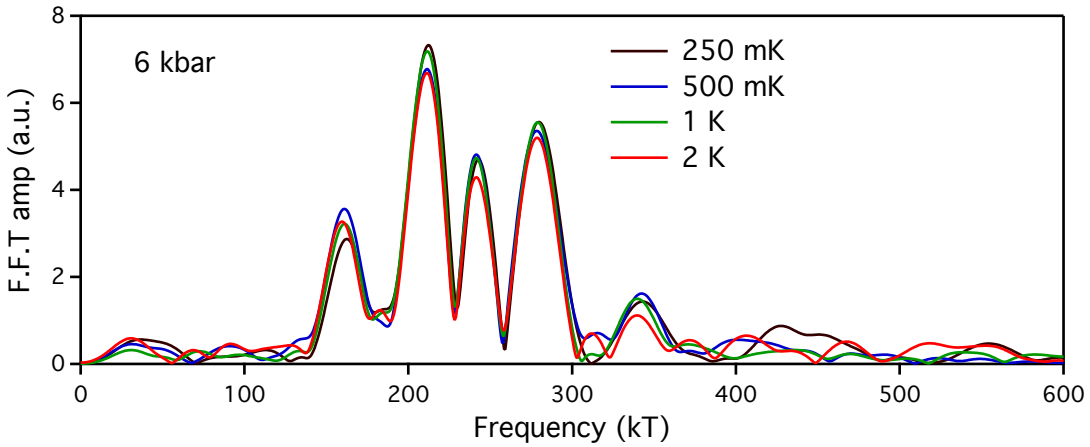

Figure 4.9: *The FFT of the oscillations in the Hall signal at 6 kbar interpolated to 5000 points in inverse field for various temperatures. A Hanning window was used and the data is padded with 100,000 zeros.*

[1,0,0] freq (T) 6 kbar	Scattering length 6 kbar (Å)
161.0	330
211.8	375
243.0	400
278.7	430

Table 4.2: A table showing quantum oscillation frequencies for sample pressurised sample at 6 kbar with field applied along (1,0,0) direction in 1^{st} column. The scattering length for each frequency is then shown in the 2^{nd} column.

to give an amplitude, A, of the form

$$A = \sum_n \cos(2\pi A_n^{rel} F_n B + \phi) \tag{4.3}$$

where F_n are the frequencies deduced from the FFT and ϕ is just a phase correction were plotted. The relative amplitude of each frequency, A_n^{rel}, was also deduced fom the FFT. The result of this simulation is shown in Figure 4.10 (a) carried out with $m^* = 0.25\ m_e$ and $T_D = 12$ K for all frequencies. For the 4 frequencies, which are shown in Table 4.2, using the Dingle temperature $T_D = 12$ K scattering lengths were calculated and are also shown in Table 4.2.

Quantum oscillations were also measured at 10 kbar to 14 T. The magnetoresistance at 10 kbar is shown in Figure 4.11 (a). Again a smoothly varying background was subtracted so $\overline{\rho}$ could be plotted against inverse field as shown

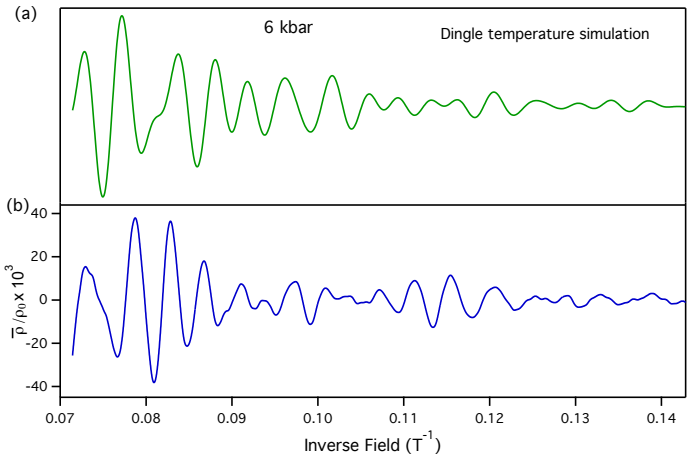

Figure 4.10: *(a) A summation of 4 cosine waves with frequencies deduced from the FFT damped by the Dingle factor R_D with $T_D = 12\ K$. (b) For comparsion the real oscillations at 250 mK after a smoothly varying background has been subtracted plotted against inverse field. The oscillations have been normalised to the zero field resistivity.*

in Figure 4.11 (b) for various temperatures. The plots to determine the effective mass are shown in Figure 4.12 where again the markers are the experimental points and the dashed lines fits to R_T. An effective mass of $m^* = 0.30 \pm 0.3\ m_e$ was deduced. The FFT of the data in inverse field again using a Hanning window with 100,000 padding zeros is shown in Figure 4.13. Now the previously seen 4 main peaks have been reduced to 1 peak of frequency 190 T. The Dingle temperature was estimated using a simulation this time with only 1 cosine wave and is shown in Figure 4.14 (a). For comparison the oscillations at 36 mK are plotted in Figure 4.14 (b). The simulation was carried out for $T_D = 12$ K and m^*. The amplitude profiles show good agreement and a scattering length $l = 317$ Å was deduced from T_D.

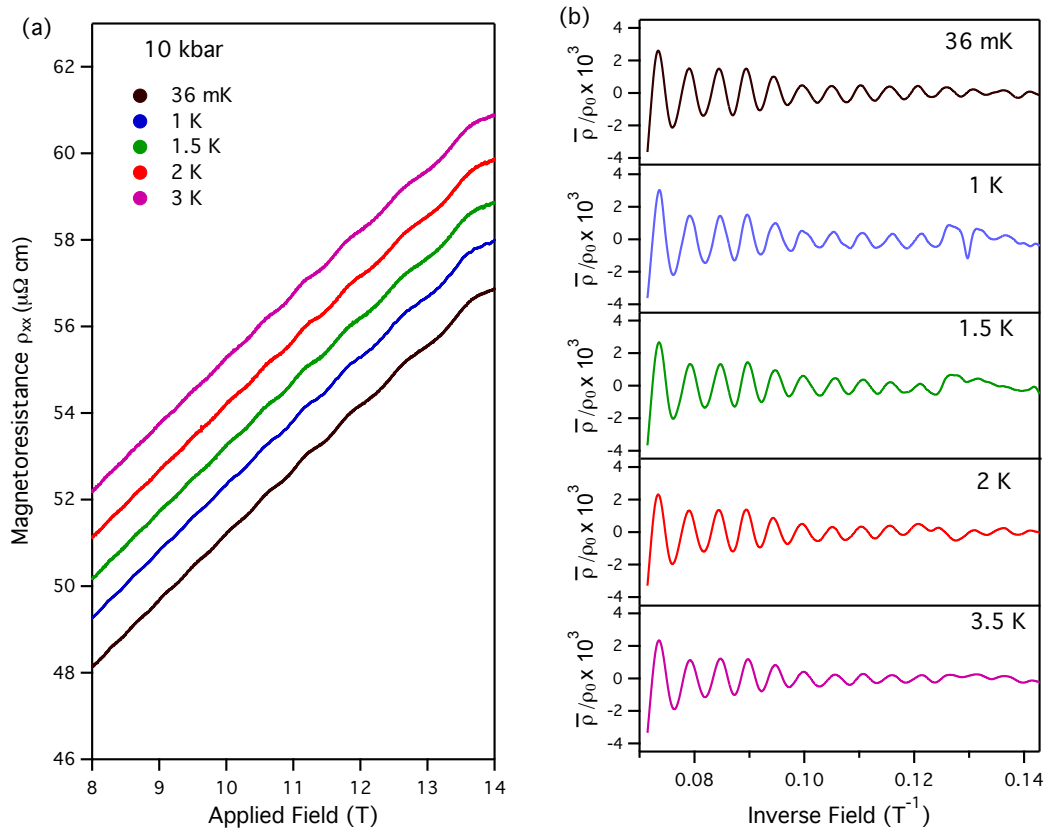

Figure 4.11: *(a) The measured magnetoresistance signal at 10 kbar for various temperatures clearly displaying quantum oscillations. The field has been applied along the (1,0,0) direction of the crystal. (b) Plots of the oscillation amplitude $\overline{\rho}$ after a smoothly varying background has been subtracted normalised to the zero field resistivity ρ_0 against inverse field.*

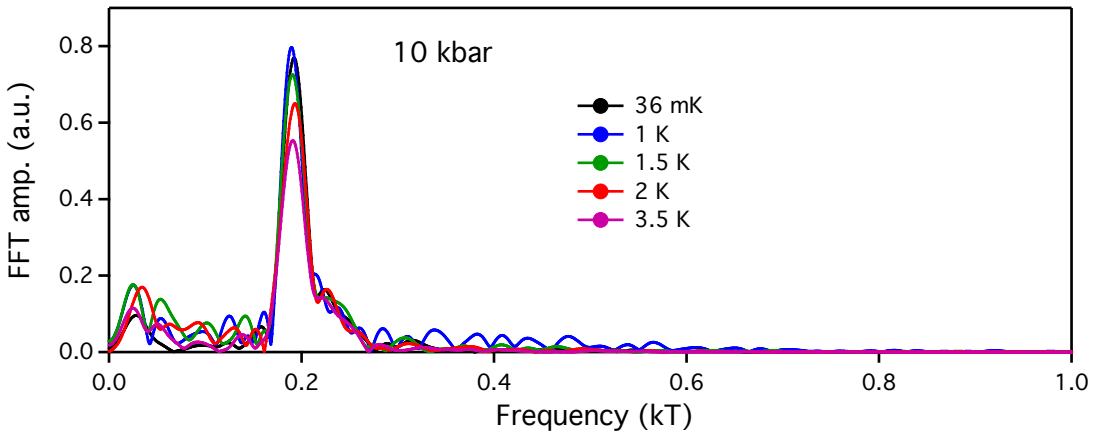

Figure 4.13: *The FFT of the oscillations at 10 kbar interpolated to 5000 points in inverse field for various temperatures. A Hanning window is used and the data is padded with 100,000 zeros.*

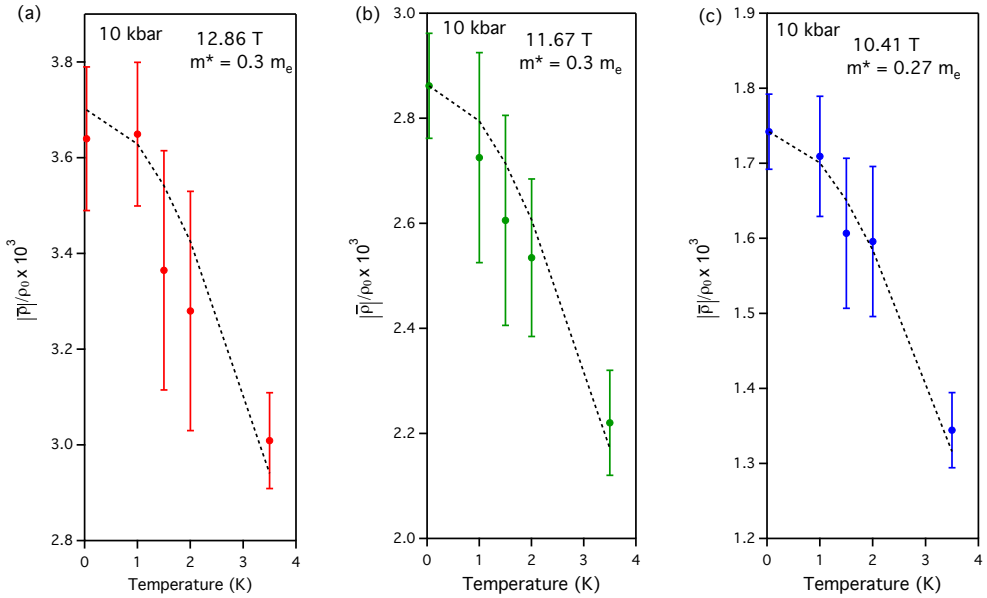

Figure 4.12: *(a)-(c) The magnituge of the amplitude of oscillations* $\mid \overline{\rho} \mid /\rho_0$ *against temperature at for 3 fields at 10 kbar, shown as markers. The dashed lines are fits to equation 4.1 in order to determine the effective mass* $m*$.

4.3 Discussion

As mentioned in section 4.1 previous high pressure experiments saw SnTe undergo a transition from the fcc structure to an orthorhombic phase. Kafalas and Mariano [54] saw the transition take place at 18 kbar on a large sample using solid NaCl as a PTM. A solid PTM may not lead to very hydrostatic conditions, particularly in a sample of the size used in their investigation. The experiment carried out here was similiar to that of Zhou *et al.* [56] who saw the fcc state was stable to 41 kbar using small samples in a diamond anvil cell and liquid PTM. During our investigation to 22 kbar we conclude our sample remained in the fcc phase at 300 K and no orthorhombic transition occured.

The anomaly in resistivity indicating the T_c of the ferroelectric transition was evident at 88 K for a pressure of 6 kbar as shown in Figure 4.4 (c). The sample used in this investigation was a single crystal taken from growth 3 which have a T_c between 80 - 90 K as discussed in Chapter 2. A T_c of 88 K is then in the range expected, however no ambient pressure measurement of T_c was carried out before being loaded into the pressure cell. At 10 kbar and above no anomaly is detected at any temperature in resistivity as shown in Figure 4.4 (f), (i) and (l). A

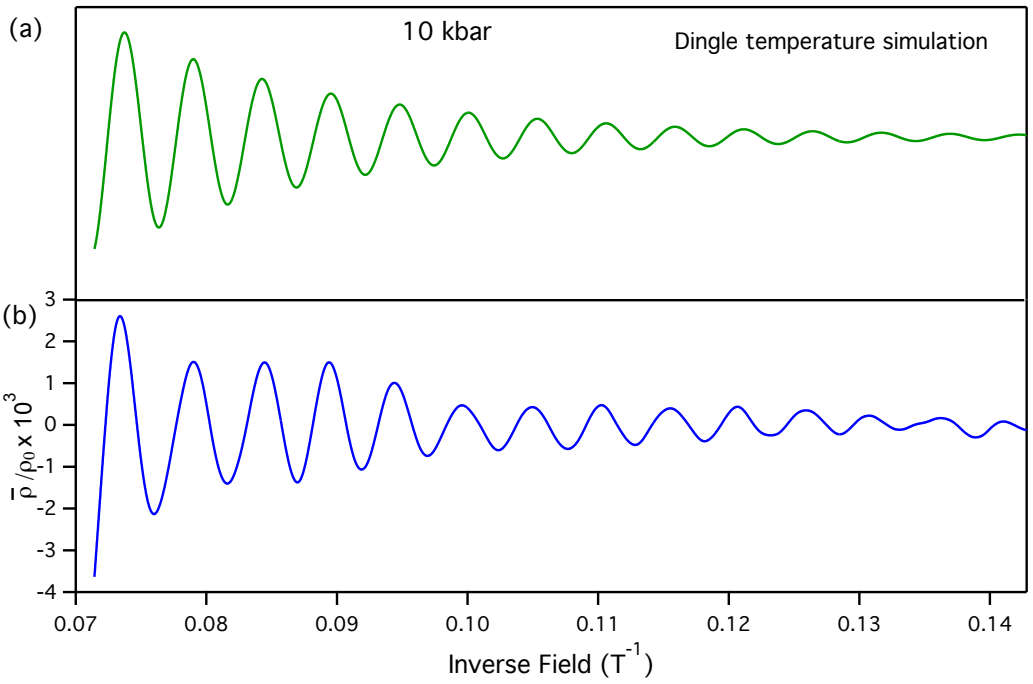

Figure 4.14: *(a) A cosine wave with frequency 190 T deduced from the FFT damped by the Dingle factor R_D with $T_D = 12$ K. (b) For comparsion the real oscillations at 36 mK after a smoothly varying background has been subtracted plotted against inverse field. The oscillations have been normalised to the zero field resistivity.*

clear indication the transition has been suppressed somewhere between 6-10 kbar. Whether the transition remains 2^{nd} order before it becomes suppressed cannot be deduced from the current data set.

The suppression of the ferroelectric transition is much more clearly evident in the quantum oscillation data. In the FFT of the oscillations carried out at ambient pressure in Chapter 2, 4 different oscillation frequencies were measured in all samples that passed through T_c. In the sample studied in this chapter at 6 kbar 4 oscillation frequencies still remain below T_c as shown in Figure 4.9. At 10 kbar where the transition is suppressed a single frequency is observed as shown in Figure 4.13. No quantum oscillation data was collected for 17 kbar and 22 kbar. Previous measurements carried out by Savage *et al.* [14] and measurements carried out in Chapter 2 here suggest the Fermi surface is composed of 4 pockets of holes at each L point in the Brillouin zone. The 4 observed frequencies are then caused by the ferroelectric transition distorting

these pockets making up the Fermi surface. As mentioned in Chapter 2 the most likely cause of 4 different frequencies is the 4 pockets are no longer equivalent, splitting into two sets one along the polar axis and the other inclined to it. The shape of the pockets may also be modified leading to a further doubling of the number of extremal orbits when viewed along a [0,0,1] direction.

As the distortion is suppressed a single frequency at 190 T is measured corresponding to 4 single pockets of equal size. Along with the change in Fermi surface the Hall resistivity, ρ_{xy}, also shows a large change in magnitude going from 6 kbar to 10 kbar shown in Figure 4.5 (a). In the distorted phase at 6 kbar 4 oscillation frequencies at 161.0, 211.8, 243.0 and 278.7 T were observed as shown in Figure 4.9. The frequency, F, is proportional to the extremal Fermi surface, S, area by

$$F = \frac{\hbar}{2\pi e} S \tag{4.4}$$

so the largest pockets in the distorted phase are almost twice the size of the smallest ones. This was also seen in Figure 2.13 for the sample rotated at ambient pressure. A cause of the change in ρ_{xy} may be the various pocket contribution to the carrier concentration. If in the distorted phase the smaller pockets dominate the conduction carriers a larger Hall resistivity could be expected than if all 4 contributed equally as when the transition is suppressed by pressure.

A detailed band structure calculation is required to see how the bands change going from the fcc phase to the rhombohedral ferroelectric phase as well as a Fermi surface calculation. Close comparison between experiment and calculation may then lead to why 4 oscillation frequencies are observed and the changes in observed Hall resistivity ρ_{xy}. It would also provide evidence to which pockets contribute most to the carrier density.

As well as the extremal Fermi surface area the effective masses, m^*, were deduced from the quantum oscillation temperature damping. At 6 kbar in the rhombohedral phase an effective mass of $m^* = 0.25\ m_e \pm 0.03\ m_e$ was calculated. This calculation was done under the assumption that each pocket in the distorted Fermi surface had the same effective mass which may not be the case. At 10 kbar in the fcc phase for one type of pocket in the Fermi surface an effective mass of $m^* = 0.3\ m_e \pm 0.03\ m_e$ was calculated. If we consider only a single band (i.e. ignore the 4 pockets), mass at the L point is expected to increase with the band gap. The trend at a point a small distance from L can however be the

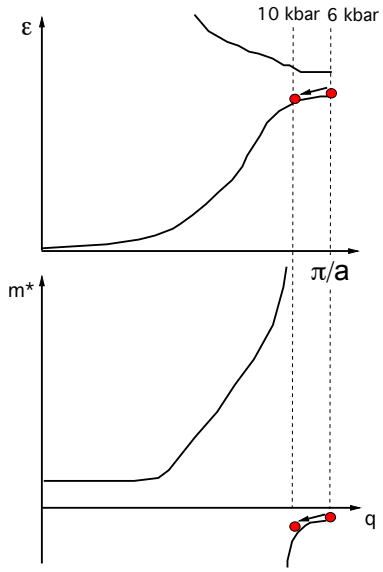

Figure 4.15: *(a) The bandstructure ε vs* $\mathbf{q}$ *of a semi-conductor in the 1 D nearly free electron model (b) The corresponding effective mass m*. Going from 6 kbar to 10 kbar a small increase in effective mass which would correspond to a small opening of the bandgap is seen.*

opposite. An increase in the gap causes m^* to fall as the $\mathbf{q}$ at which m^* diverges is pushed further from L. This is illustrated in Figure 4.15. Thus although a gap is suggested the direction of the change is not clear.

More evidence for the change in bandgap is given below when electron-phonon coupling is considered. Via the Thomas-Fermi theory the effective mass is also related to the velocity of sound which was calculated from the long wavelength acoustic phonon dispersion curves in Chapter 3. As discussed in Chapter 3 the acoustic phonon frequency squared, $\omega(\mathbf{q})^2$, is proportional to the restoring forces, which are the elastic constants, just as in Hooke's law (in the long wavelength limit). This was also discussed in Chapter 1 when considering the Taylor expansion of strain. As the ions move they will produce ionic fields which the conduction electrons act to screen in what is known as Thomas-Fermi screening. The wavevector over which the screening takes place is $\mathbf{k}_{TF} = 1/\lambda_{TF}$, the Thomas-Fermi momentum, is related to the density of states via

$$\mathbf{k}_{TF} = 2\pi e\sqrt{\frac{g(0)}{\epsilon_0}} \tag{4.5}$$

where $g(0)$ is the density of states at the Fermi level and ϵ_0 the corresponding dielectric constant. The density of states is related to the effective mass m^* via

$$g(0) = \frac{m^* \mathbf{k}_F}{\hbar^2 \pi^2} \tag{4.6}$$

at the Fermi level where $\mathbf{k}_F$ is the Fermi wavevector. Therefore the screening of the ionic potential over the wavevector $\mathbf{k}_{TF}$ of the longitudinal acoustic phonons relates the speed of sound v_s to the effective mass by

$$v_s \propto \frac{1}{\sqrt{m^*}} \tag{4.7}$$

as is discussed in the text by Ashcroft and Mermin [60]. The velocity of sound, $\partial\omega/\partial q$ deduced from the acoustic phonons is shown Table 3.3 for SnTe at 300 K and 75 K for all available data. The ratio of the longitudinal acoustic velocity of sound squared along the [1,1,1] direction at 75 K to 300 K is

$$\frac{v_{75}^2}{v_{300}^2} = \frac{4943^2}{4861^2} = 1.04. \tag{4.8}$$

The ratio of the effective mass in the fcc phase stabilised by pressure to the rhombohedral phase at 6 kbar is $0.3m_e/0.25m_e = 1.2$, showing relative agreement.

The shift in effective mass then corresponds to a shift in the density of states and band gap opening. Littlewood *et al*'s [19] ARPES measurements recently showed a shift in the valence band going from the fcc phase to the rhombohedral phase of ≈ 0.1 meV. The shift in band energy ε predicted by Littlewood *et al.* [19] is given by

$$\varepsilon = \pm\sqrt{\varepsilon^2 + p_{el}^2 u^2} \tag{4.9}$$

where p_{el} is the electron-phonon coupling and u the displacement of the two fcc sublattices caused by the ferroelectic transition which is driven by phonons. The results of the phonon linewidth in the TO phonon above and below T_c are shown in Figure 3.10 (b) as a function of temperature and in Figure 3.11 as a function of $\mathbf{q}$ at various temperatures. Above T_c the phonon linewidth increases strongly towards the zone centre, Γ, where the softening occurs, indicating strong electron-phonon coupling as shown in Figure 3.11 (a) and (b) for 300 K and at $T_c = 75$ K. However below T_c at 25 K the phonon linewidth is small and constant for all $\mathbf{q}$

measured as shown in Figure 3.11 (c), indicating small electron-phonon coupling. This change in electron-phonon coupling would then correpsond to the a shift in band gap according to the results of Littlewood *et al* [19].

As well as the effective mass the scattering length, l, was determined from the quantum oscillation data presented here at 6 kbar and 10 kbar. At 6 kbar in the distorted phase the calculated Dingle temperature $T_D = 12$ K lead to $l = 330,\ 375,\ 400$ and 430 Å for the 4 respective oscillation frequencies. At 10 kbar the Dingle temperature was calculated to remain 12 K and $l = 317$ Å for the 4 identical pockets making up the Fermi surface. The graphs of residual resistivity in Figure 4.4 (b) and (e) for 6 kbar and 10 kbar respectively show an increase of ρ_{2K}/ρ_{300K} from 0.134 to 0.195. The residual resistivity is then higher in the fcc phase than the rhombohedral phase. However there is also a decrease in scattering length and increase in effective mass as well as large change in electron-phonon coupling. The resistivity ρ is approximated by the scattering rate τ

$$\rho \approx \frac{m^*}{\tau} \tag{4.10}$$

and the scattering length l is given by

$$l = v\tau \tag{4.11}$$

where v is the velocity of the electrons. Then an increase in resistivity is as to be expected going from the rhombohedral phase to the fcc phase where l has decreased. Again in the estimation of T_D in the rhombohedral phase the same m^* and T_D was assumed for each frequency which may not be the case. One would also need knowledge to which pocket contributes most to the carriers in the distorted phase to understand fully why the residual resistivity has increased in the fcc phase.

On closer inspection of the Hall resistivity, ρ_{xy}, shown in Figure 4.5 (a) its curvature has changed significantly from that of ambient pressures. Shown in Figure 4.16 (a) between the smaller field range of ± 2 T, ρ_{xy}'s curvature is clearly different from that of the ambient pressure measurement of a sample from the same growth shown in Figure 4.16 (b). The dashed black straight lines are guides for the eye. This curvature could be the cause of two competing bands contributing to the Hall signal. Recently Kim *et al*. [61] measured the Hall effect

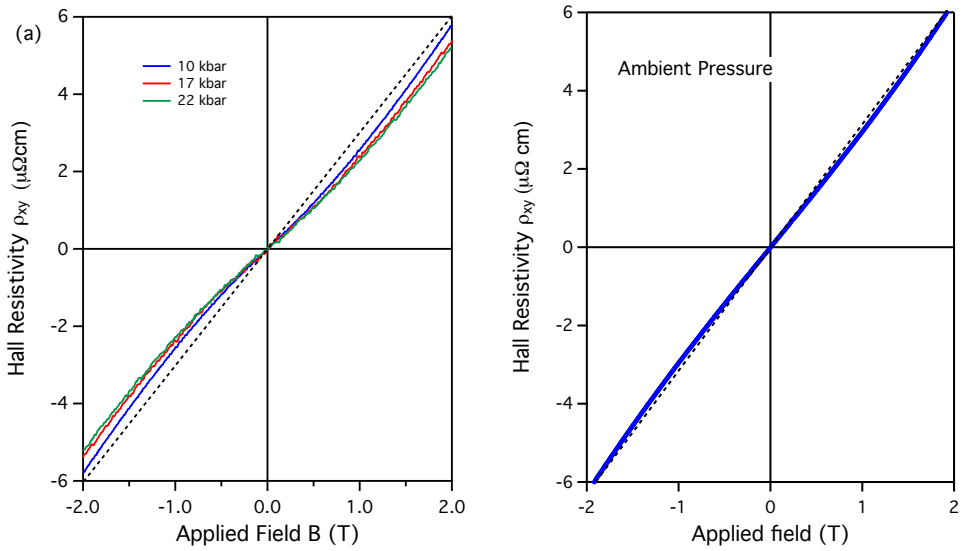

Figure 4.16: *(a) The Hall resistivity ρ_{xy} vs field between ± 2 T at various pressures where the rhombohedral distortion has been suppressed. (b) The Hall resistivity in the rhombhedral phase ρ_{xy} at ambient pressure on sample S31 from the same growth. Dashed lines are guides for the eye.*

in SmB_6 also predicted to be a topological insulator. A similiar two band structure contributed to the Hall effect. Kim *et al.* [61] separated the two bands in ρ_{xy} attributing one to be from the surface states and one from the bulk. The surface states have a high Hall conductivity that outweighs the bulk Hall conductance at low fields. This would be similiar to what is shown in Figure 4.16 (a) above, a band with higher conductance outweighs another band at low fields leading to the curvature. The curvature may be more pronounced at higher pressures when the rhombohedral distortion is suppressed and more surface states are present. Hsieh *et al*'s prediction of the surface states in SnTe are integer quantum hall like which would have a high conductance for applied fields. A two band model for SnTe is currently being carried out to try seen if a surface band exists. This concludes all the measured results on SnTe now the anomalous Hall effect shall be discussed in Fe_3Sn_2.

Chapter 5

The Anomalous Hall Effect and Fe_3Sn_2

The purpose of this chapter is to introduce the 3 main contributions to the anomalous Hall effect in ferromagnetic materials. In particular the intrinsic effect which is dependent on the Berry curvature of Bloch bands is focussed on. The Berry curvature was introduced in Chapter 1 and shall not be rediscussed at length again, other than its contribution to the electron velocity in an electric field. An example of a material where the intrinsic effect dominates is briefly introduced for the purposes of comparison, namely MnSi. The material Fe_3Sn_2 is then discussed at length which includes a literature review of all the current experimental data available.

5.1 Introduction

So far we have only considered the Hall effect for non-magnetic materials. A recurring problem in condensed matter physics is the anomalous Hall effect (AHE) in ferromagnets. The Hall resistivity then includes an extra anomalous term usually described as

$$\rho_{xy} = R_0 H_s + R_s M_s \tag{5.1}$$

where R_0 is the ordinary Hall effect coefficient, R_s is the anomalous Hall coefficient and M_s the magnetisation of the sample for an applied effective field H_s [62]. In the region where the magnetisation increases for applied fields, the anomalous contribution, $\rho_{xy}^{AHE} = R_s M_s$, will dominate ρ_{xy}. When the magnetisation reaches

a saturation value at high enough applied fields, the ordinary Hall effect then becomes the dominant term. Experimentally R_s is found to depend on material-specific parameters, particularly a power law of the longitudinal resistivity ρ_{xx},

$$\rho_{xy}^{AHE} \sim \rho_{xx}^{\gamma} M_s \tag{5.2}$$

as γ takes a value of 1 or 2, in general. The exact value of γ is dependent on the mechanisms causing ρ_{xy}^{AHE}. Two of the three main effects, the intrinsic band structure and the extrinsic side jump impurity scattering both scale with γ=2. The third which is skew scattering has γ=1.

The first microscopic description of the AHE was given by Karplus and Luttinger (KL theory) now known as the intrinsic effect. The electrons acquire an extra anomalous velocity perpendicular to the applied electric field which is non zero when the spin orbit interaction (SOI) is included [63]. This perpendicular motion then contributes to the Hall effect. The anomalous velocity derived by KL is completely reliant on the band structure of the material so is independent of scattering and disorder. The intrinsic effect was thought to be a small contribution to ρ_{xy}^{AHE} for many years in favour of extrinsic scattering mechanisms. Recently however it has seen a revival due to its Berry curvature description. The anomalous velocity described by KL is now expressed in terms of the Berry curvature of Bloch bands where the SOI is still playing its fundamental underlying role to give non-zero anomalous currents [3].

The extrinsic scattering effects must also be considered. The most notable are skew scattering described by Smit [64] and a side-jump contribution descibed by Berger [65]. These are based on the asymmetric scattering of up and down spins from impurities caused by the SOI. But first we shall focus on the description of the intrinsic effect. The review articles by Nagasoa et al. [62] and Xiao et al. [3] go into detail of the derivation of the various intrinsic and extrinsic contributions. The very readable paper by Ong and Lee [66] gives a good description of the intrinsic effect in terms of Berry curvature. The main properties are summarised here.

Since ferromagnets have broken time-reversal symmtery the Berry curvature of the Bloch bands can be non-zero as discussed in Chapter 1. The Berry curvature

of the Bloch band n in $\mathbf{k}$ space, is given by

$$\mathbf{\Omega}_n(\mathbf{k}) = \nabla_{\mathbf{k}} \times \langle u_n(\mathbf{k}) | i\nabla_{\mathbf{k}} | u_n(\mathbf{k}) \rangle \tag{5.3}$$

and the semiclassical equation for an electron in an electric field is

$$v_n(\mathbf{k}) = \frac{1}{\hbar}\nabla_{\mathbf{k}}\varepsilon_n(\mathbf{k}) - \frac{e}{\hbar}\mathbf{E} \times \mathbf{\Omega}_n(\mathbf{k}) \tag{5.4}$$

as discussed in Chapter 1. The term $\frac{e}{\hbar}\mathbf{E} \times \mathbf{\Omega}_n(\mathbf{k})$ is the extra anomalous velocity described by KL but now expressed as a Berry curvature. The anomalous term acts perpendicular to the applied electric field and an intrinsic Hall current $\mathbf{J}^{int}$ can be derived as

$$\mathbf{J}^{int} = \frac{e^2}{\hbar}\mathbf{E} \times \sum_{\mathbf{k}} \Omega(\mathbf{k}) f(\varepsilon_k) \tag{5.5}$$

where $f(\varepsilon_k)$ is the Fermi-Dirac distribution function [66]. This current is then independent of the scattering lifetime τ. The conductivity σ_{xy}^{int}, is stated as

$$\sigma_{xy}^{int} = \frac{e^2}{\hbar} \int \frac{d\mathbf{k}}{(2\pi)^d} f(\varepsilon_k) \Omega_{k_x k_y} \tag{5.6}$$

where σ_{xy}^{int} has no dependence on τ and hence ρ_{xx}^0. Using the usual magnetoconductivity tensors [67] given by

$$\sigma_{xy} = \frac{\rho_{xy}}{\rho_{xy}^2 + \rho_{xx}^2} \approx \frac{\rho_{xy}}{\rho_{xx}^2} \quad \text{and} \quad \sigma_{xx} = \frac{\rho_{xx}}{\rho_{xy}^2 + \rho_{xx}^2} \approx \frac{1}{\rho_{xx}} \tag{5.7}$$

assuming $\rho_{xx} \gg \rho_{xy}$. We can express the intrinisic Hall resistivity, which is what we actually measure, as

$$\rho_{xy}^{int} = \frac{e^2}{\hbar}\langle\Omega\rangle\rho_{xx}^2 \propto \rho_{xx}^2 \tag{5.8}$$

with $\langle\Omega\rangle$ now the weighted average of the Berry curvature. Therefore those bands with non-zero Berry curvature and hence integral Chern numbers will contribute to the intrinsic Hall term.

One should also briefly mention the Chern number of contributing bands can be overall zero but the local Berry curvature is nonzero. This is particularly important near band crossings (or anti-crossings) at the Fermi energy. The SOI interaction spilts the bands of up and down spins by an energy usually denoted as Δ. The Berry curvature of the two bands has opposite signs across Δ. If the

Fermi energy lies within this gap a large intrinsic AHE can be found. Another point to mention is that, the integral of eq 5.6 is over the entire Fermi sea, whereas we could probably assume that it is the electrons on the Fermi surface that contribute most to σ^{int}. Haldane [68] showed that this is actually the case and the intrinsic AHE can also be expressed as a Fermi surface property.

The two extrinsic terms that contribute to ρ_{xy}^{AHE} arise due to impurity scattering. The skew-scattering effect is based on an asymmetry caused from impurities when the SOI in the semiclassical Boltzmann equation [64] is considered. In the usual Boltzmann equation, the transition probability in a state going from left to right equals that of right to left with respect to the magnetisation direction. When the SOI is considered for a ferromagnet, right hand and left hand transitions no longer have the same transition probabilites. Considering this asymmetry, the scattered charge carrier wavevector gains an orthogonal term leading to a transverse current from the applied electric field. This transverse current depends on the scattering rate and hence the anomalous resistivity from skew scattering is $\rho_{xy}^{skew} \propto \rho_{xx}$

The side-jump mechanism in the simplest case is based on Gaussian wavepackets being scattered from spherical impurities. After the scattering has taken place, an outgoing wavepacket will gain an asymmetry [65], caused by the SOI. This leads to a transverse displacement and hence a Hall current. The contribution of the side-jump mechanism scales as $\rho_{xy}^{side} \propto \rho_{xx}^2$ and therefore is also independent of the impurity concentration and τ. Hence it can be difficult to distinguish experimentally between the intrinsic mechanism and that of side-jump scattering. Usually band structure calculations are used to estimate what the contribution from the intrinsic AHE should be, then compare to experimental data.

As already stated for many years only the skew and side-jump mechanisms were thought to be the main contributors to the AHE and the intrinsic effect was small. Hence most authors would fit

$$\rho_{xy}^{AHE} = a^{skew}\rho_{xx} + b^{side}\rho_{xx}^2 \tag{5.9}$$

where a^{skew} and b^{side} are constants. However there are now many instances where the intrinsic term accounts for ρ_{xy}^{AHE}, particularly in materials with a large SOI and non-simple band structure. One such example is that of MnSi whose AHE shows many interesting properties.

5.2 Intrinsic effect in MnSi and Topological Hall effect

MnSi crystallises in the non-centrosymmetric cubic B20 structure and has a helical magnetic structure caused by a Dzyaloshinskii-Moriya (DM) interaction [69]. The DM-interaction is a contribution to the total magnetic exchange between two neighbouring spins $\mathbf{S}_1$ and $\mathbf{S}_2$ given by

$$H_{DM} = \mathbf{D} \cdot (\mathbf{S}_1 \times \mathbf{S_2}) \tag{5.10}$$

where $\mathbf{D}$ is the anistropic exchange interaction. Spin-orbit coupling is the mechanism behind the interaction, which acts to force $\mathbf{S}_1$ and $\mathbf{S}_2$ to be at right angles on a plane perpendicular to the vector $\mathbf{D}$. The orientation of $\mathbf{D}$ is constrained by symmetry. When the crystal field has an inversion symmetry with respect to the centre between the two magnetic ions then $\mathbf{D}$ will vanish [70]. However in the case of non-vanishing $\mathbf{D}$ in a ferromagnet, the DM-interaction acts to the cant the moments, causing exotic magnetic structures such as the helical structure in MnSi. Application of an external magnetic field in MnSi then causes the spins to cant towards a conical structure before eventually aligning with the field at 0.6 T [71].

The paper of Lee *et al.* [71] measured the AHE in MnSi at ambient pressure. They describe the Hall resistivity as

$$\rho_{xy} = R_0 H_s + S_H \rho_{xx}^2 M_s \tag{5.11}$$

where the anomalous Hall conductivity $\sigma_{xy}^{AHE} = S_H M_s$. The field independent scale factor S_H was shown to be temperature independent by Lee *et al.* [71] so that σ_{xy}^{AHE} is only determined by the magnetisation. There is thus no dependence on τ and the anomalous contribution was attributed to be wholly from the intrinsic effect. Of course one could say that the side-jump mechanism would also produce a similiar result. The general consensus now is that in materials without very simple band structures it is the intrinsic contribution that dominates [62]. There are some instances where the side-jump mechanism may dominate the intrinsic effect however. Experimentally it can be assumed that in a metallic ferromagnet where the SOI is large, a temperature independent scaling factor would suggest

an intrinsic AHE. Other corrections could be made for skew scattering due to its temperature dependence. To attribute a large side-jump mechanism, a close comparison with theory is required to exclude the intrinsic effect.

The phase diagram of MnSi also contains a pocket region where magnetic Skyrmions occur on top of a ferromagnetic background [69]. Skyrmions are whirls of magnetisation with topological winding numbers similiar to Chern numbers. Since they are topologically non-trival they are protected and cannot transform smoothly into another magnetic state. In the case of MnSi these Skyrmions are arranged in a hexagonal lattice in a plane perpendicular to the field [69]. The Berry curvature of Bloch bands acts in momentum space where the SOI and local electric fields vary on the inverse atomic length scale. However in the case of smoothly varying magnetic structures, such as Skyrmions, spin orientation varies over length scales much longer than the Fermi wavelength. Conduction electrons passing through Skyrmions can pick up Berry phases due to the local magnetisation in real space leading to a topological Hall effect (THE). The THE in MnSi induced from the Skyrmions can then be separated from the ordinary Hall effect and intrinsic AHE [72, 73].

The existence of such intrinsic properties and topological Hall effects make the AHE a very active area of current research. The iron stannide compound Fe_3Sn_2 may display exotic canted ferromagnetic states, making it an exciting material to investigate the AHE and possible existence of states caused by real space Berry phases. Although known for many years Fe_3Sn_2 has still many undetermined properties, mainly due to experimental difficulties and inaccuracies.

5.3 Fe_3Sn_2 review

Using X-ray diffraction Malaman *et al.* [74] determined the crystal structure of Fe_3Sn_2 to be rhombohedral with space group $R\bar{3}m$. Recent powder neutron diffraction experiments by Fenner *et al.* [75] produced a structure in almost exact agreement with the X-ray results of Malaman *et al.* [74]. The crystal structure found by Fenner *et al.* [75] is shown in Figure 5.1 (a). The Fe ions occupy the 18h crystallographic sites, constructing bilayers of offset Kagome networks. The Kagome networks consist of 2 sizes of equilateral triangles coloured blue and red in Figure 5.1 (a) with Fe-Fe distances of 2.732 and 2.582 Å respectively. There

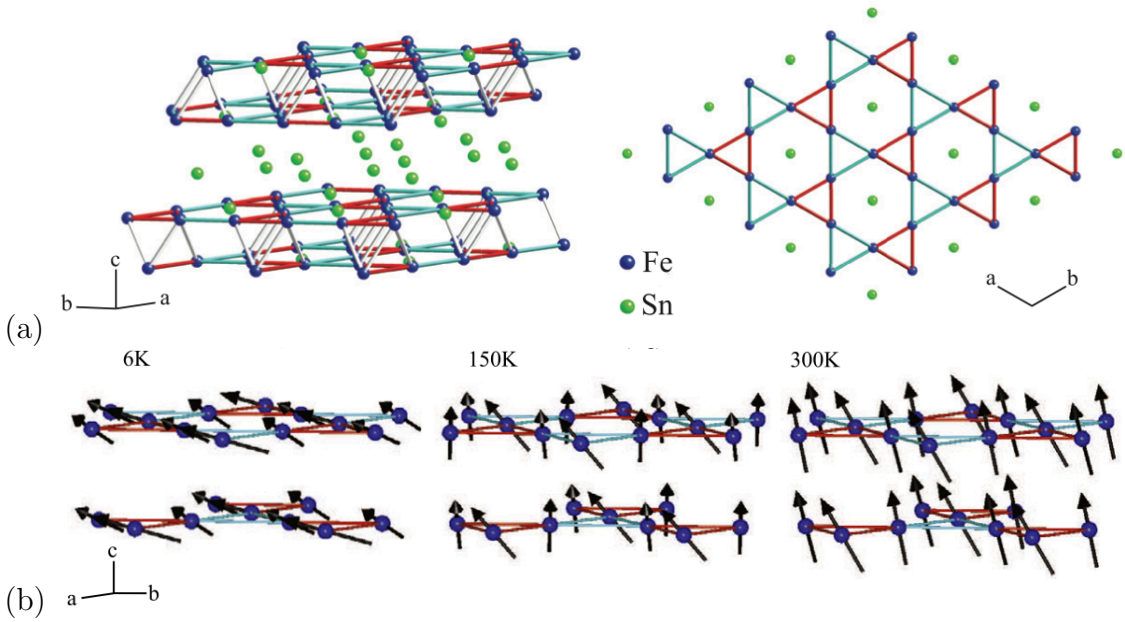

Figure 5.1: *(a) The crystal structure of Fe_3Sn_2 showing the kagome networks formed by Fe bilayers. The Sn atoms also have two positions, the centre of the kagome lattice and between bilayers. (b) The non-collinear magnetic structure of Fe_3Sn_2 at 6 K, 150 K and 300 K respectively from neutron scattering results of Fenner et al. [75] Both (a) and (b) taken from Fenner et al. (2009) [75].*

are two specific sites for Sn ions, within the kagome layers at (0.0000, 0.0000, 0.1041) and between the kagome bilayers at (0.0000, 0.0000, 0.3303) shown as green in Figure 5.1 (a). The Fe-Fe distances between bilayers is 2.584 $\mathring{A}$ and give lattice parameters $a = b = 5.3147\mathring{A}$, $c = 19.7025\mathring{A}$.

At 300 K Fe_3Sn_2 is ferromagnetic with a Curie temperature between 612 K [76] to 657 K [77]. Most early experiments measuring the magnetic properties of Fe_3Sn_2 were done using Fe^{57} and Sn^{119} Mössbauer spectroscopy. Mössbauer spectra give quantitative details on hyperfine interactions, which are small energies from the interaction between the nucleus and its neighbouring electrons. The principle of Mössbauer spectroscopy uses a supply of excited ^{57}Fe and ^{119}Sn nuclei which decay to their ground state slowly via a Gamma ray cascade. This cascade includes a Gamma ray of well defined energy, 14.4keV(ν= 3.48×10^{18}Hz) for ^{57}Fe and 23.87keV (ν= 5.77×10^{18}Hz) for ^{119}Sn. These γ-rays excite a transition in the sample being studied. By moving the source at a speed v, the frequency of the γ-ray is then varied slightly via the Doppler effect, allowing one to probe the hyperfine interactions of the excited nuclei. The 3 interactions

probed are an isomer shift, electric quadrupole splitting and Hyperfine magnetic field splitting (HMF). The HMF in magnetically ordered materials is analogous to Zeeman splitting in electronic energy levels. The HMF lifts the spin degeneracy of the nuclear states in magnetic fields and transitions from an excited to the ground state are bound by strict selection rules.

Trumpy *et al.* [76] were the first to carry out Mössbauer studies in powdered Fe_3Sn_2 using both ^{57}Fe and ^{119}Sn to measure their HMFs respectively. Trumpy *et al.* [76] ^{57}Fe spectra shows at room temperature a single HMF_{Fe} of 199 kG. Upon cooling to liquid nitrogen temperatures HMF_{Fe} at 219 and 211 kG were observed. Trumpy *et al.* suggest a transition temperature of 114 K where the two fields merge into one. They applied an external magnetic field at room temperature observing the one field case split into the two fields at 4 kG. This then suggests the transition is very field sensitive even at modest fields. At the time of publication, Trumpy *et al.* [76] had not fully resolved the Sn^{119} spectra. However several other authors carried out further experiments shortly afterwards providing further insight to the magnetic structure.

The two Mössbauer studies supplemented with magnetisation data by Le Caër *et al.* [77, 78] along with the neutron diffraction study by Malaman *et al.* [79] showed an interesting magnetic structure exists in Fe_3Sn_2. The ^{57}Fe Mössbauer spectra found indications for 3 distinct phases [77]. At high temperatures above 220 K a single spectrum is observed with rather sharp peaks. For intermediate temperatures 77 K - 220 K the spectrum has specific peaks broadened. At 4 K the spectrum is split into two subspectra. Further to this ^{119}Sn spectra [78] for the two specific tin sites have a HMF perpendicular to the *c*-axis below 60 K and parallel above 250 K.

These Mössbauer results allowed Le Caër *et al.* [77, 78] to deduce a magnetic structure for Fe_3Sn_2. At low temperatures the moment spins point completely in the *a*-*b* plane. Upon heating going from 60 K to 250 K a collinear spin rotation from the *a*-*b* plane towards the *c*-axis occurs. Then above 250 K the spins point along the *c*-axis. The description of the rotation Le Caër *et al.* proposed is as follows. At a temperature T, a fraction α(T) of the spins are close to the *a*-*b* plane while (1-α) make an angle of θ_p with the *c*-axis. A plot of α and θ_p against temperature from Le Caër *et al.* [78] is shown in Figure 5.2 (a) and (b) respectively. The rotation is not continuous but increases abruptly at

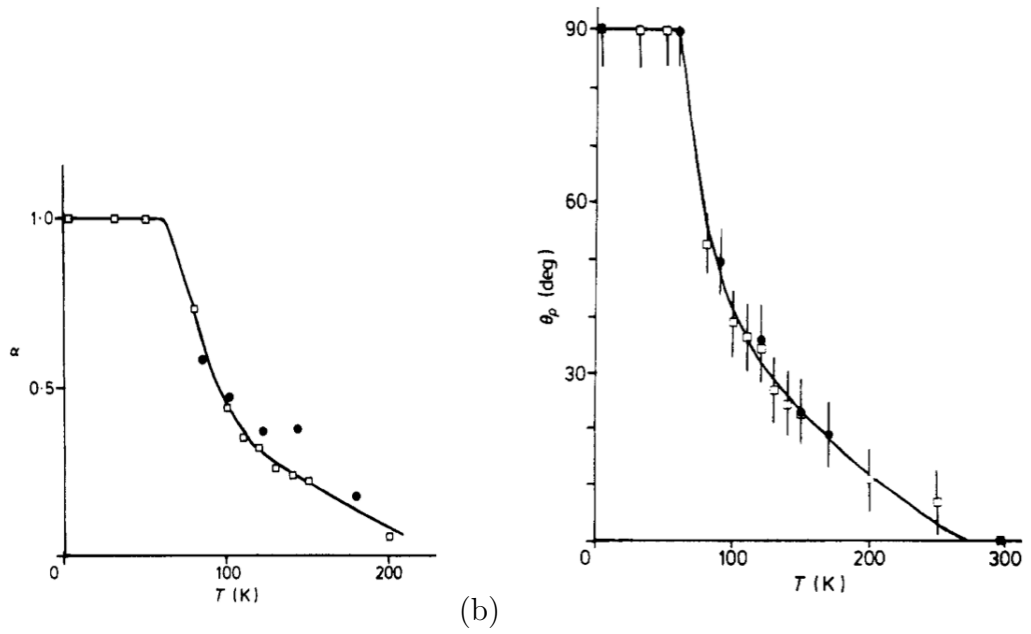

Figure 5.2: *(a) and (b) the Mössbauer results of Le Caër et al. (1979) [78]. (a) The fraction α of Fe spins in the a-b plane as a function of temperature. Open squares respresent ^{119}Sn spectra while closed circles are ^{57}Fe (b) The temperature dependence of the angle θ_p the spins make with the c-axis open squares respresent ^{119}Sn spectra while closed circles are deduced from the neutron diffraction*

approximately 100 K. This may be the cause of the behaviour seen by Trumpy *et al.* [76].

Figure 5.2 (b) of θ_p against temperature includes points deduced from the neutron diffraction study of Malaman *et al.* [79]. The diffraction patterns measured by Malaman *et al.* [79] show a continuous increase of (001) magnetic reflections going from 280 K to 60 K, where they remained constant below 60K. Analysis of their data suggested that the spins made an angle of around 60^o with the $a-b$ plane below 60K. However the Mössbauer data of course strongly proposed the spins were completely in the plane. To explain this Malaman *et al.* [79] modified the magnetic form factor of iron to fit their data, leading to the points in Figure 5.2 (b). Malaman *et al.* [79] also carried out neutron diffraction and Mössbauer spectroscopy experiements with externally applied fields of 56 kOe in the case of neutrons and 14.2 kOe for Mössbauer spectroscopy. Magnetisation measurements as a function of field were also carried out. These experiments were all on polycrystalline samples and show for fields approximately above 5 kOe all the Fe spins lie parallel to the applied field. One should note that polycrystals

only have a 1/3 of the c-axis parallel to the applied field in zero field. This would suggest a single crystal investigation is needed to gain more accurate results. Malaman *et al.* [79] did carry out some single crystal magnetisation measurements which showed that spins aligned with the external field.

More recent studies carried out by Fenner *et al.* [75] describe differeing magnetic behaviour in Fe_3Sn_2. Fenner *et al.* [75] point out that there is no symmetry requirement that the spin rotation must be collinear with moments of equal magntitude. A bilayer Kagome network lacks a centre of inversion, allowing for the DM-interaction, which is one possible cause for non-collinearity. The rotation of the moments towards the *a*-*b* plane could then happen non-collinearly with spin moments of varying magnitude. Fenner *et al* [75] also suggest at a temperature below approximately 80K, Fe_3Sn_2 transitions to a re-entrant spin glass phase.

A spin glass is a disordered magnetic state where the magnetic spins are not aligned in a regular pattern with long range order after passing through a freezing temperature T_f. The spins generally have a large degree of in-built frustration *e.g.* from the crystal structure or bonding and a large number of possible ground states. After passing through T_f the chosen ground state will be metastable with slow relaxation times, hence the term glassy [70]. A re-entrant spin glass occurs when the high temperature phase is already ferromagnetic as opposed to paramagnetic. So the low temperature magnetic phase actually has more disorder than the high temperature one, most likely caused by competing magnetic interactions.

Fenner *et al.*'s [75] magnetisation curves as a function of temperature display a marked dip below 80K, characteristic of a spin glass with T_F=80K. Thermoremanent magnetisation data also showed a clear dependence on the waiting time t_w for measurement of the magnetisation. Fitted data was characteristic of a spin glass phase. Neutron diffraction experiments were used to determine the magnetic structure at 300 K, 150 K and 6 K. The possibility of non-collinear spins prompted Fenner *et al.* [75] to fit their neutron data to both collinear and non-collinear models (Malaman *et al.* [79] considered only collinear spins). Fenner *et al.* [75] conclude the non-collinear model gives slightly better fits to the data than the collinear model, particularly at the lower temperatures studied. The neutron diffraction results of Fenner *et al.* [75] are shown in Figure

5.1 (b), where the arrows represent the non-collinear spins. They suggest a similiar high temperature picture, that the spins point mostly along c at 300 K as shown in Figure 5.1 (b). On cooling the spins rotate, non-collinearly towards the *a*-*b* plane, where the moments can slightly differ in magnitude. Below 80 K the spins are then in a frustrated glassy state pointing mostly along the *a*-*b* plane. The rotation however may begin at much higher temperatures than previously thought with slight non-collinearity at temperatures well above 300 K.

Kida *et al.* [80] measured the AHE and magnetisation in Fe_3Sn_2 polycrystalline samples of RRR = 4, at various temperatures from 300 K to 100 K as a function of field. The magnetisation shows no marked change between 300 to 100K with only a slight decrease in magntitude. The Hall effect follows a similiar pattern and fitted data suggest a strong intrinsic effect makes up the bulk of the anomalous signal. The magnetisation saturates at a value of 1.9 $\mu_B Fe^{-}1$ which is signifcantly less than that expected for localised Fe-moments, indicating the Fe valence electrons are shared between localised and itinerant envirnoments.

A recent theoretical paper by Pereiro *et al.* [81] predicts the existence of Skyrmion excitations in a 2D Kagome lattice. Considering competition between the anitsymmetric exchange interaction, **D**, and the isotropic exchange interaction, **J**, Pereiro *et al.* consider a Hamiltonian of an itinerant electron system given by

$$H = \sum_{\langle ij \rangle} [-J_{ij} \mathbf{s}_i \cdot \mathbf{s}_j + \mathbf{D}_{ij} \mathbf{s}_i \times \mathbf{s}_j] - g\mu_B \mathbf{B} \sum_i s_i \tag{5.12}$$

where $\langle ij \rangle$ denotes the atomic indices to the first nearest neighbour pairs and the last term is the Zeeman effect under an external magnetic field **B** where g is the Lande g-factor and μ_B the Bohr magneton. The Skyrmions then exist as topological excitations which can interact via collisons etc. rather than those in MnSi which remain static on the lattice. Pereiro *et al.* [81] suggest the non-collinear magnetic structures in Fe_3Sn_2 may may a place to look for these excitations.

Ikoma *et al.* [82] considered the possible magnetic phases in the Kagome lattice in a mean-field theory approximation. In their model itinerant electrons and localised spins coexist. The itinerant electrons are treated in a tight binding model and localised spins have antiferromagnetic coupling. There is also a ferromagnetic

exchange interaction between localised and itinerant electrons spins, **K**. The Hamiltonian used was

$$H = t\sum_{ij\sigma} c^{\dagger}_{i\sigma}c_{j\sigma} - \mathbf{K}\sum_{i}\mathbf{s}_i\cdot\mathbf{S}_i + \mathbf{J}\sum_{\langle ij\rangle}\mathbf{S}_i\cdot\mathbf{S}_j \tag{5.13}$$

where the first term represents the nearest neighbour hopping with overlap integral t. The second term then represents the coupling between itinerant electron spin, $\mathbf{s}_i$ and localised spin, $\mathbf{S}_i$ and the 3rd term the anti-ferromagnetic coupling. Their results show a rich phase diagram of the possible ferromagnetic and chiral structures. In particular in the phase boundary between ferromagnetic and chiral states in the Kagome lattice an electric phase separation occured. In this region different exotic magnetic phases may appear.

The Kagome lattice of Fe_3Sn_2 may then contain previously unseen physics that has yet to be reported. Whilst significant data has been collected on polycrystalline samples, very little exists for single crystals. In order to investigate the magnetic structure and AHE further a single crystal experiment is required. Crystals of of Fe_3Sn_2 were grown by the group of Andrew Wills, UCL, using a technique called chemical vapour transport. First Fe and Sn powders were weighed in the correct proportion, ground together and sealed in an argon filled silica tube. The mixture was then heated to 800°C for 1 week. The powder was then placed in a two-zone tube furnace with a temperature gradient of 650°C at the evaporation end to 720°C at the deposition end. A transport agent is used, in this case iodine, as a catalyst and is placed along with the powder at the evaporation end of the furnace. There is then an exothermic reaction between the iodine and powder causing the Fe_3Sn_2 to migrate to the hotter end of the tube furnace to be deposited as small crystals, in a process known as chemical vapour deposition. By isolating a single crystal of significantly high RRR from this grown material the magnetisation and AHE are measured to determine the magnetic structure and effects contributing to the AHE. These results shall be discussed at length in the next chapter.

Chapter 6

Results on Fe_3Sn_2

The focus of this chapter is to firstly discuss the selection and characterisation of Fe_3Sn_2 single crystals by Laue diffraction and resistivity curves. Magnetisation of the samples was then measured using a commercial MPMS. This data was supplemented with measurements of the AHE and magnetoresistance as a function of field over a wide temperature range. Several interesting properties are noticed in the AHE following a complete analysis of available data. Particularly the AHE in the temperature range 300 K-70 K is strongly intrinsic and contains an anomaly that may be related to a topological Hall effect.

6.1 Characterisation and Magnetisation

Several samples of Fe_3Sn_2 were received from the group of Andrew Wills, UCL. Using X-ray Laue diffraction, 3 samples S1, S2 and S3, were concluded to be single crystals by taking many Laue patterns across their surfaces and edges. The samples were air sensitive due to the oxidation of Fe and were kept under vacuum when experiments were not being performed. The crystal S3 is shown in Figure 6.1. Small spots of oxidation are visible, but these were removed relatively easily by cleaving using Scotch tape. Samples were generally triangular or hexangonal in shape with a large flat planar surface and thin in the plane, typically $\approx 40\mu m$. S3 had the shape of a 2mm equliateral triangle shown by the scale in Figure 6.1 with a thickness of $35\mu m \pm 2\mu m$. A Laue pattern from the large planar surface is shown in Figure 6.2 (a) and along one of the thin edges in Figure 6.2 (b). Each pattern is fitted using the Origin express software and we deduce the large planar

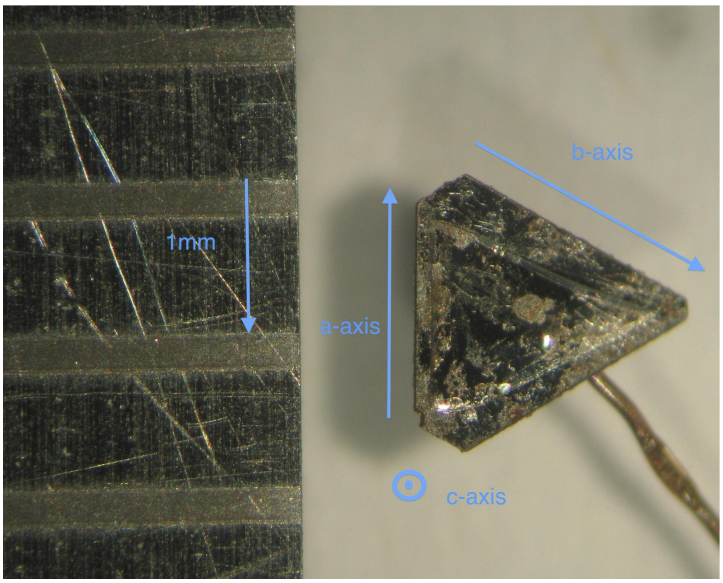

Figure 6.1: *The single crystal sample, S3, of Fe_3Sn_2. Small spots of oxidation are visible. The blue arrow indicates the scale of 1mm. Each axis direction is also shown determined from X-ray Laue diffraction*

surface was perpendicular to the c-axis, while each long edge corresponds to the equivalent $a - b$ axes, as shown by the blue arrows in Figure 6.1.

As a measure of crystalline quality the residual resistivity ratios (RRR) for the 3 samples S1, S2 and S3 were measured. Gold wire contacts (10 μm) are added to each sample, using Ag epoxy, giving a contact resistance of $\leq 2\Omega$. Current is applied and voltage measured along the a-axis in the standard 4 wire probe configuration. Samples are mounted on a large oxygen-free high thermal conductivity (OFHC) copper block and measured in the cryostat described in Chapter 2 from 300 K to 2 K.

Samples are cooled and heated slowly at 0.2 K/min while the resistance is measured. Since the samples are of a rather arbitrary shape the sample with the best geometry, S2, was chosen to deduce a geometric factor. Using Matthiessen's rule at high temperatures from sample S2 the resistivity of the other 2 samples S1 and S was deduced. The resistivity curves for the 3 samples are shown in Figure 6.3. No features are observable such as a change in slope or magnitude at $T_f = 80$ K upon entering the possible spin glass phase. The RRR=$\frac{\rho_{300K}}{\rho_{2K}}$ for each sample S1, S2 and S3 are 13.4, 13.7 and 27.6 respectively as indicated on Figure 6.3. This would suggest sample S3 is of the highest crystalline quality of those

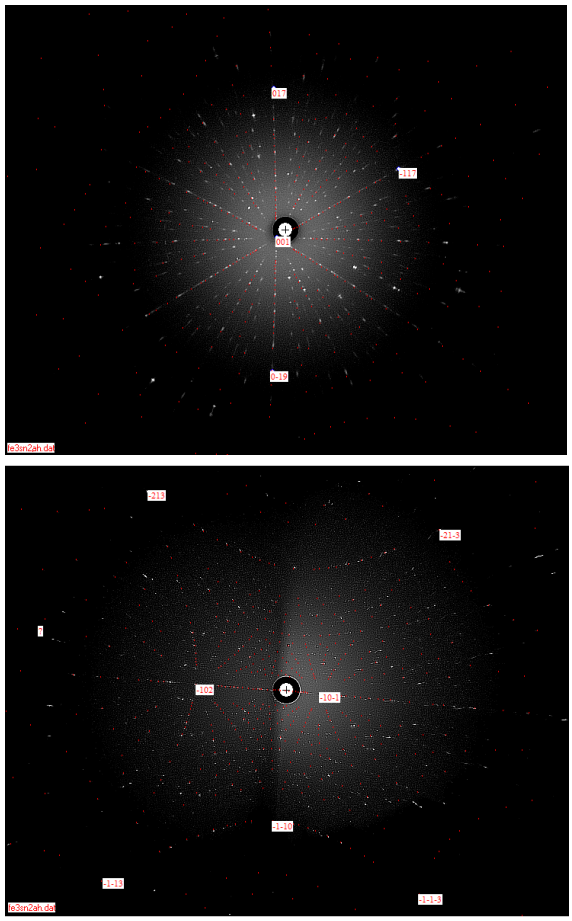

Figure 6.2: *Laue diffraction images along with calculated fits using the Origin express software. The pattern in (a) is for X-rays incident on the large planar surface of the sample in Fig. 5.2. while (b) is along one of the long edges. From these patterns and fits we can deduce the crystallographic directions, incident X-rays are along the c-axis in (a) while along the equivalent a or b axes in (b).*

available. Therefore S3 was chosen to do the majority of the experimental work throughout the remainder of this chapter.

The magnetisation of sample S3 was then measured with a magnetic property measurement system (MPMS XL) from Quantum Design, Inc.. The MPMS makes use of a superconducting quantum interference device (SQUID) to measure the samples magnetic moments. Both the theory and method of detection can be found in the manual of the instrument or the guide by McElfresh [83]. Sample weight was calculated from its dimensions and the density of Fe_3Sn_2 to give a value of 490μg. Calculation was used rather than an analytical balance since the balance requires a minimum weight of 1mg to give an accurate reading. A

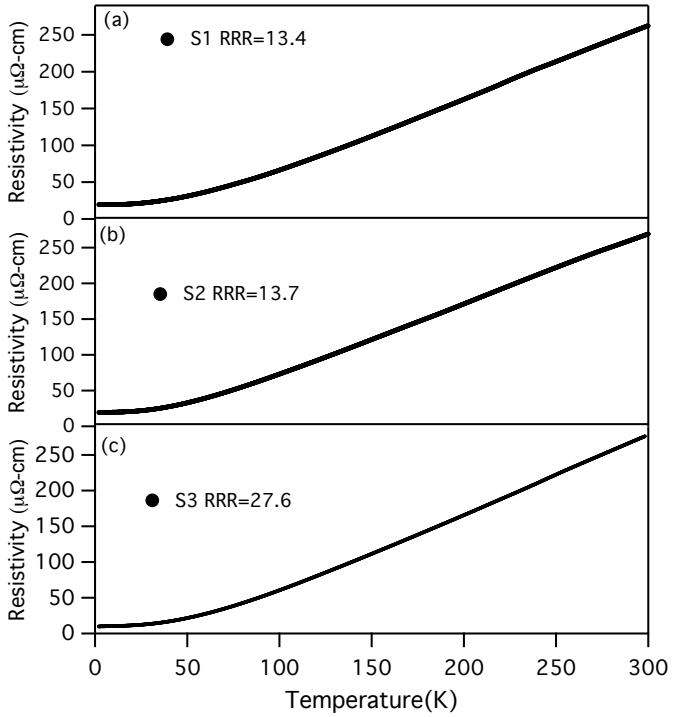

Figure 6.3: *(a)-(c) Resistivity curves of single crystals of Fe_3Sn_2 measured from 300K to 2K on cooling in zero field*

meaurement was carried out anyway and gave a value of 470 μg. The value of 490 μg was deemed to be more accurate however and used for the remainder of discussion.

The sample was mounted in a commerical MPMS straw so the c-axis was parallel to the applied field of the MPMS magnet and held in place using vacuum grease and simple clingfilm. The straw was attached to the end of a rigid rod which enters the sample space through a double seal at the top of the system. The rod is coupled to a stepper motor controlled platform which drives the sample through a series of detection coils in distinct steps. Detection coils are made from a single piece of superconducting wire counterwound into 3 coils placed within the central bore of the MPMS 7T superconducting magnet. The coils make up a second order gradiometer that have currents induced in them by the position of the sample passing through. Induced currents are ideally those created by a point-source magnetic dipole [83]. We can assume the magnetism from S3 is uniform throughout the sample and due to its size compared to the coils a point source. The straw was long and uniform extending far beyond the coils inducing

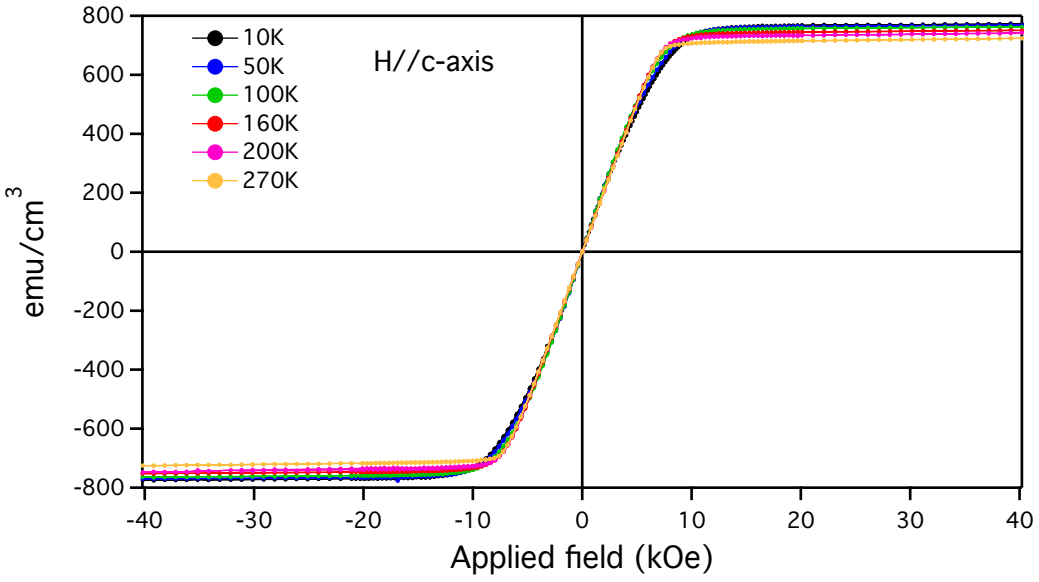

Figure 6.4: *Magnetisation curves in emu/cm^3 for sample S3 at a range of temperatures against the applied field* **H** *from the MPMS superconducting magnet. The field direction was along the c-axis.*

no currents. Currents from the detection coils travel along superconducting wires to the SQUID sensor which is shielded from the magnetic field. The SQUID output a voltage proportional to the magnetisation of the sample to give a highly accurate measure of the magnetic moment.

Sample S3, were cooled to 10K using helium gas within the sample space and was centered to the correct spatial position. The magnet output was increased from zero in increments of 400 Oe to a field of 20000 Oe and then increments of 1000 Oe til 40000 Oe. The same field profile was used on the ramp down and to negative 40000 Oe before being set again to zero. Hence any hysteresis in the sample would be detected. At each field the measurement sweep was repeated twice to increase the reliability of the data. The signal was fitted using an iterative regression method and an output of this signal analysis was expressed in electromagnetic units. Raw data graphs of emu/cm^3 against applied field **H** are shown in Figure 6.4.

The curves in Figure 6.4 show no obvious hysteresis throughout the entire temperature range measured. We have

$$\mathbf{B} = \mu_0(\mathbf{H} + \mathbf{M}) \tag{6.1}$$

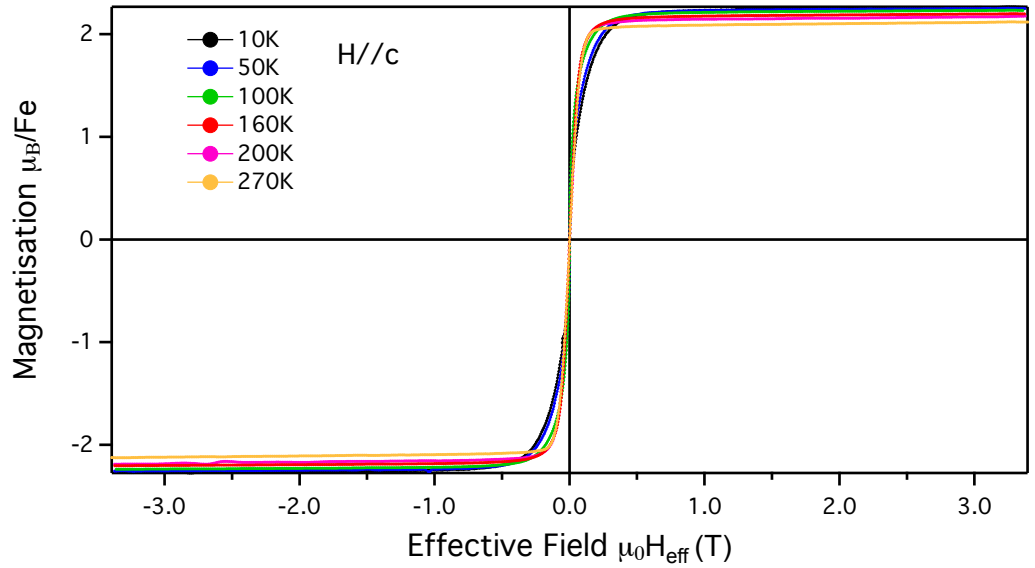

Figure 6.5: *Magnetisation curves for sample S3 in Bohr magnetons per Fe atom as a function of effective field* $\mathbf{H}_{eff}$ *corrected by a demagnetisation factor N=0.69. Field was applied along the c-axis*

where **B** is the flux density in Tesla, **H** is the applied field in A/m and **M** the magnetisation of the sample also in A/m. Since our sample is in the strong ferromagnetic regime demagnetising factors cannot be ignored and we express the effective applied field $\mathbf{H}_{eff}$ as

$$\mathbf{H}_{eff} = \mathbf{H} - N\mathbf{M} \tag{6.2}$$

For a reversible ferromagnet an estimate for the demagnetising factor N can be made from the slope of the linear low field region (the demagnetising factor will be discussed more in Section 6.3). In this case the gradient of the curves between approximately ±8 kOe applied fields is used to calculate a value of N=0.69. Graphs of magnetisation now expressed in Bohr magnetons per Fe atom are shown in Figure 6.5 against the effective field in the sample corrected for demagnetisation.

Each magnetisation curve saturates to a value of approximately 2.1-2.2μ_B per Fe, in good agreement with literature values [75, 77, 79]. However one would expect large changes in the magnetisation particularly if there was a spin glass transition at T_F = 80 K. By focussing on the low field region before

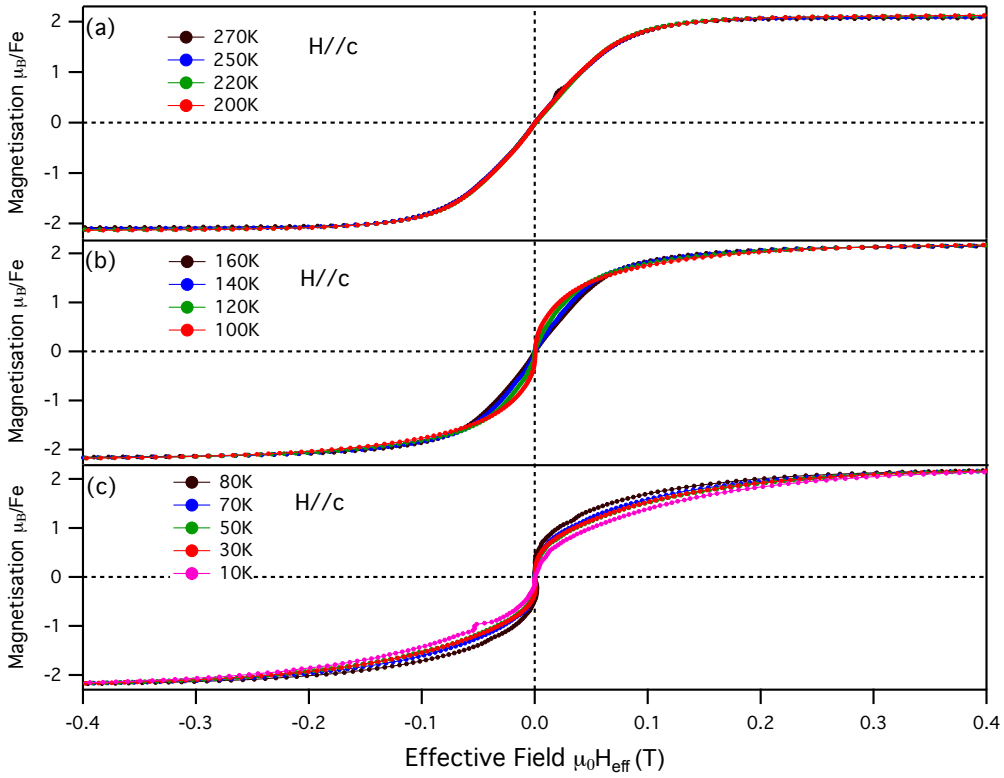

Figure 6.6: *(a)-(c) Magnetisation curves for S3 in Bohr magnetons per Fe atom as a function of effective field* $\mathbf{H}_{eff}$ *corrected by a demagnetisation factor N=0.69. Field was applied along the c-axis*

saturation, shown in Figure 6.6, more features are evident. The significance of these changes in magnetisation shall now be compared to those in the AHE and magnetoresistance and discussed in section 6.3.

6.2 Anomalous Hall Effect

The Hall effect and magnetoresistance were measured simultaneously on S3 using the standard 6 wire Hall configuration. Again current is applied along the *a*-axis while the magnetoresistance is also measured in the same direction. Hall contacts are attached perpendicular to the *a*-axis. One can assume ρ_{xx} and ρ_{xy} to be relatively isotropic within the *a*-*b* plane. The sample is cooled from 300K to 2K. The field ramped from -4T to 4T and back to -4T again to measure any hysteresis at a rate of 0.04 T/min over a range of constant temperatures. On each field sweep the sample is allowed to thermalise for 30 minutes with the

exchange gas of the cryostat before ramping begins. Taking into account the magnetoresistance of the Cernox thermometer (which is small above 10K), and the extreme care to thermalise the sample, an error in the temperature of each field sweep is estimated to be ±10 mK.

Resistivity and conductivity tensors can be calculated for the sample within the magnetic field. As already stated we can assume isotropy for the high symmetry direction of the *a*-*b* plane so $\rho_{xx} = \rho_{yy}$ and $\rho_{xy} = -\rho_{yx}$ and longitudinal-transverse coupling is ignored, as discussed in Chapter 2. The resistivity tensor is written as

$$\rho = \begin{pmatrix} \rho_{xx} & \rho_{xy} & 0 \\ \rho_{yx} & \rho_{yy} & 0 \\ 0 & 0 & \rho_{zz} \end{pmatrix} = \begin{pmatrix} \rho_{xx} & \rho_{xy} & 0 \\ -\rho_{xy} & \rho_{xx} & 0 \\ 0 & 0 & \rho_{zz} \end{pmatrix} \tag{6.3}$$

By inversion the usual conductivity tensors

$$\sigma_{xx} = \frac{\rho_{xx}}{\rho_{xx}^2 + \rho_{xy}^2} \approx \frac{\rho_{xx}}{\rho_{xx}^2} \tag{6.4}$$

and

$$\sigma_{xy} = \frac{\rho_{xy}}{\rho_{xx}^2 + \rho_{xy}^2} \approx \frac{\rho_{xy}}{\rho_{xx}^2} \tag{6.5}$$

can be assumed as discussed in Chapter 5 since in this case $\rho_{xx} \gg \rho_{xy}$. Again both the Hall resistivity and magnetoresistance have been anti-symmetrised and symmetrised as described in the tensor above and previously in Chapter 2 and Chapter 4. As an example the measured Hall resistivity at 300 K is shown in Figure 6.7 (a). While the shape of the curve is quite antisymmetric there is a large magnetoresistance contribution due to misalignment of the contacts and $\rho_{xx} \gg \rho_{xy}$. Therefore the anti-symmetrisation described by equation (2.3) was carried out and the resulting data is shown in Figure 6.7(b). The same process for symmetrisation was carried out for the magnetoresistance data. We spilt the results into 3 distinct regions. The high temperature region 300 K - 160 K, the intermediate 160 K - 80 K and then the low temperature region below 80 K. The Hall resistivity and magnetoresistivity are shown for the high temperature region in Figure 6.8 against the effective field in the sample.

The Hall resistivity follows the shape one would expect. An anomalous part increases rapidly over the region magnetisation also increases for small applied

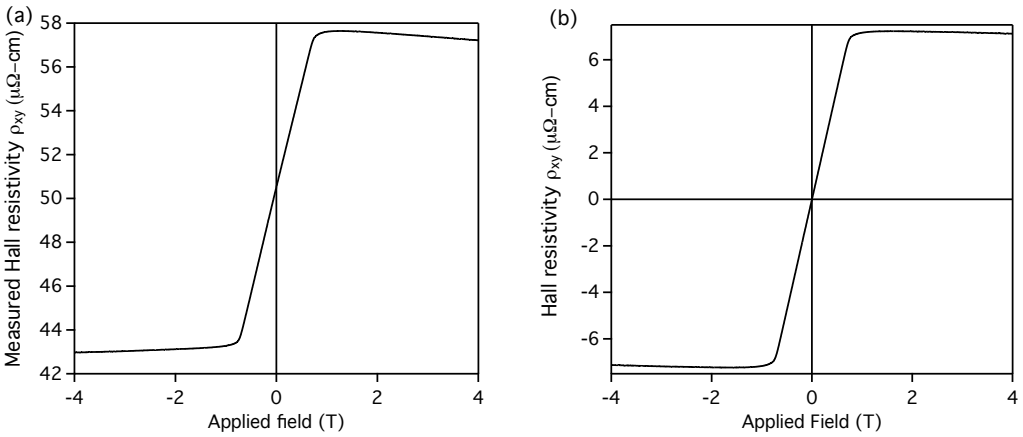

Figure 6.7: *(a) The Hall resistivity measured in sample S3 for a variety of temperatures as a function of field. (b) The simultaneoulsy measured magnetoresistivity ρ_{xx} minus the resisitivity at zero field for the same temperature ρ_0. The field has been applied along the c-axis while the applied current was along the a-axis.*

fields. Then ρ_{xy} saturates and the ordinary Hall effect dominates subsequent changes in ρ_{xy}. The gradient of the normal Hall region suggests hole carriers are mainly present (the sign of the Hall signal was discussed in Chapter 2). The magnetoresistance is negative, not unusual for a ferromagnet, but contains a huge dip feature not previously seen in this material. The feature peaks in magnitude around 160 K before decreasing in magnitude again at lowers temperatures as shown in Figure 6.9 (b). Going from 160 K to 70 K the feature has decreased to almost zero and the magnetoresistance begins to become positive. The Hall resistivity continues to have the same shape as seen at higher temperature shown in Figure 6.9 (a).

Below 70 K we have reached the low temperature region and at 60 K the anomaly in magnetoresistance is no longer detectable as shown in Figure 6.10 (b). The magnetoresistance is now completely positive at low temperatures and still displays a kink at fields just below half a Tesla. The Hall resistivity in this region has also changed shape significantly with a completely different curvature below 40 K. Higher fields of 9 T are investigated for ρ_{xy} for 2 K and 10 K as shown in Figure 6.11. There is now a maximum in ρ_{xy} at approximately 4 T. We do not currently have magnetisation data to 9T so were unable to correct this figure for demagnetisation factors, although the field where the maximum occurs happens is high enough the effective field and applied field would be almost equal.

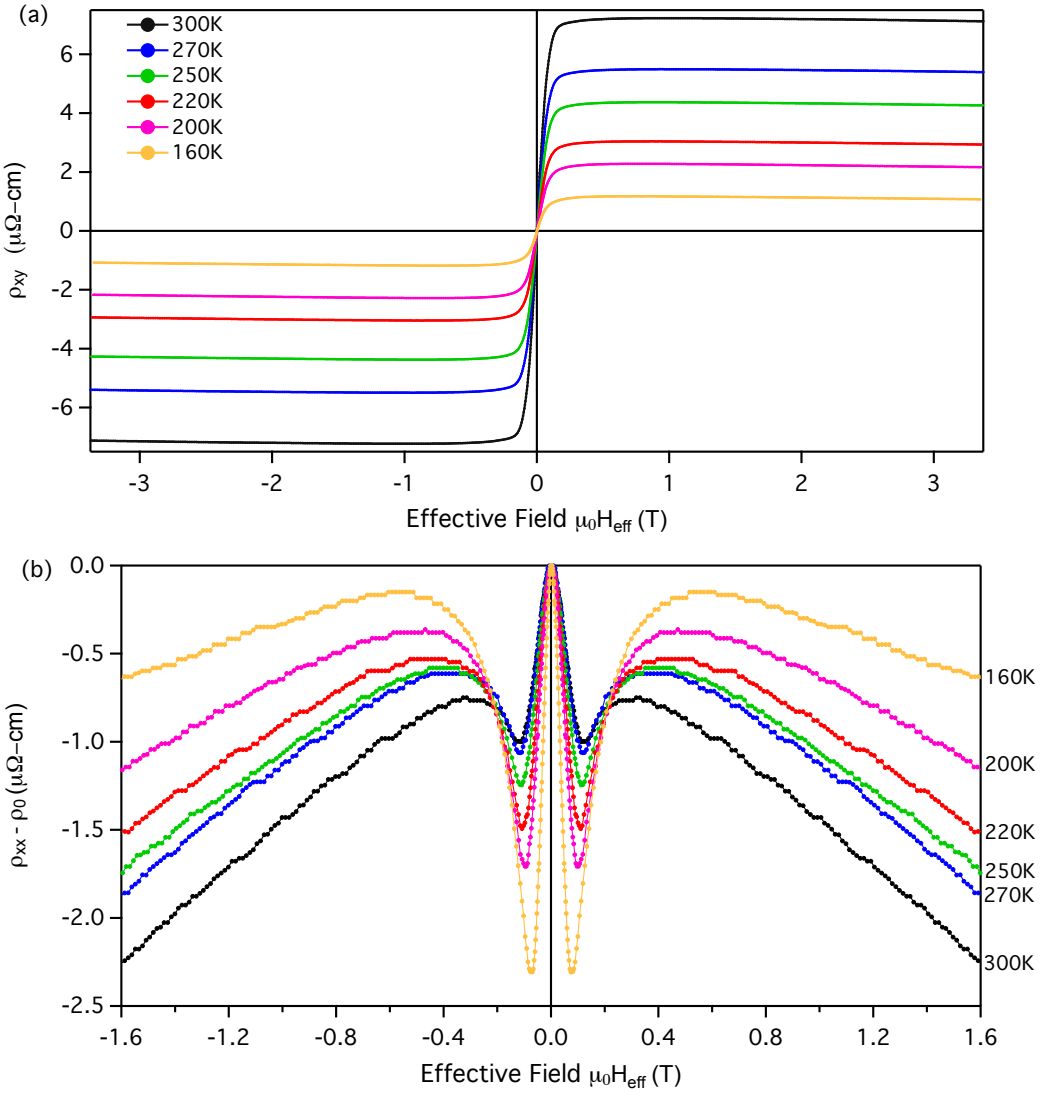

Figure 6.8: *(a) The Hall resistivity measured in sample S3 for a variety of temperatures as a function of field. (b) The simultaneoulsy measured magnetoresistivity ρ_{xx} minus the resisitivity at zero field for the same temperature ρ_0. The field has been applied along the c-axis while the applied current was along the a-axis.*

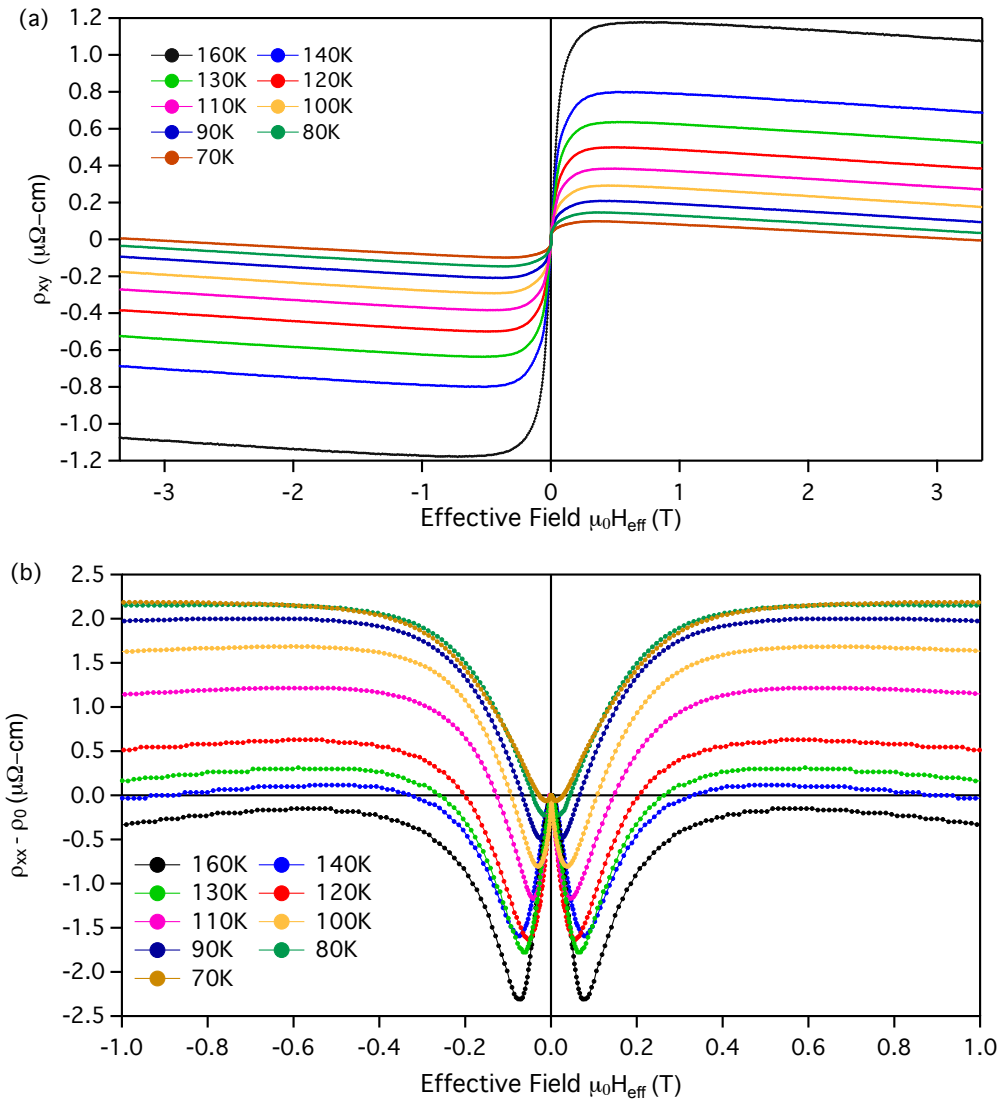

Figure 6.9: *(a) The Hall resistivity measured in sample S3 for a variety of temperatures as a function of field. (b) The simultaneoulsy measured magnetoresistivity ρ_{xx} minus the resisitivity at zero field for the same temperature ρ_0 . The field has been applied along the c-axis while the applied current was along the a-axis.*

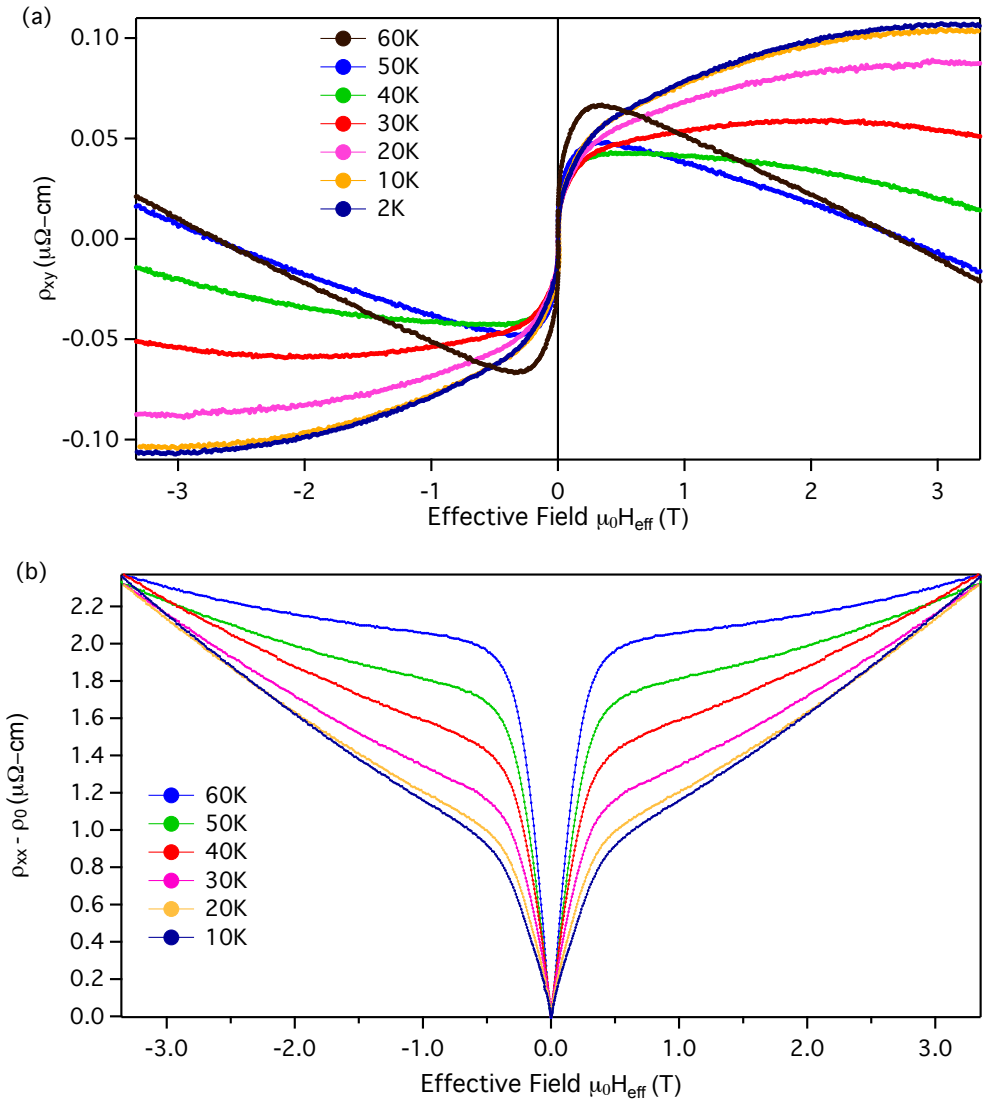

Figure 6.10: *(a) The Hall resistivity measured in sample S3 for a variety of temperatures as a function of field. (b) The simultaneoulsy measured magnetoresistance ρ_{xx} minus the resisitivity at zero field for the same temperature ρ_0. The field has been applied along the c-axis while the applied current was along the a-axis.*

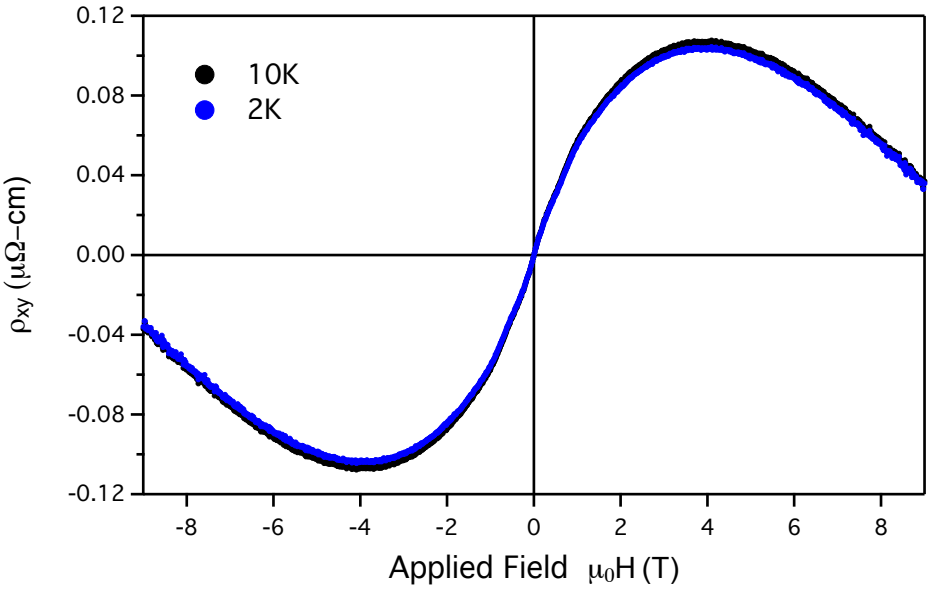

Figure 6.11: *The Hall resistivity measured in sample S3 for 2K and 10K to higher fields of 9T. The field has been applied along the c-axis while the applied current was along the a-axis.*

Each ρ_{xy} curve is fitted to the equation

$$\rho_{xy} = R_0 H_s + S_H \rho_{xx}^2 M_s \tag{6.6}$$

as described in Chapter 5. The ordinary Hall coefficient R_0 is deduced from the linear high field regions of each ρ_{xy} curve in both the high and intermediate temperature regions of Figures 6.8 (a) and 6.9 (a). For the lower temperatures of Figure 6.10 (a) the linear regions between 60-40 K can still be fitted. The high field regions above 4T in Figure 6.11 can also be fitted for 10 K and 2 K. However we can't make accurate estimates at 20 K and 30 K with the current data set, since there is no linear region in the field range measured.

A graph of R_0 against temperature for each fitted curve is shown in Figure 6.12 as the red markers. At temperatures between 300 - 80 K R_0 stays relatively constant, within error, giving a carrier concentration of $n = 1.45 \pm 0.15 \times 10^{22} cm^{-3}$. Below 80 K R_0 steeply decreases to give a value of $n = 3.125 \pm 0.2 \times 10^{22} cm^{-3}$ at the lowest temperatures measured.

Each ρ_{xy} curve then has the normal Hall contribution, $R_0 H_s$, subtracted to

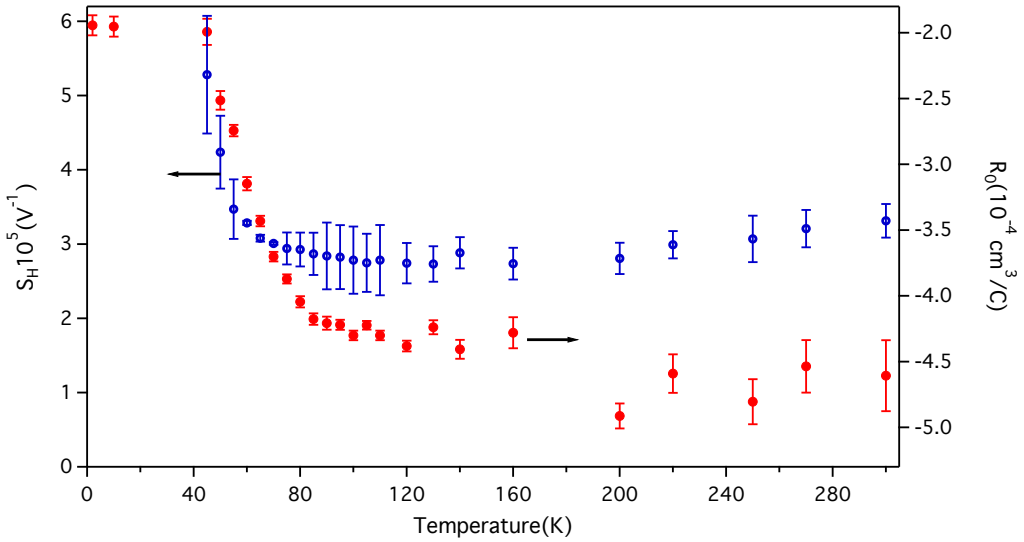

Figure 6.12: *The ordinary Hall coefficient,R_0 shown as red markers against the right axis as a function of temperature. R_0 is calculated from the linear part of each Hall resistivity curve at high field. The field independant scaling coefficient S_H is shown as blue markers on the left axis, this is calculated from the curves of ρ_{xy}^{AHE}.*

give ρ_{xy}^{AHE} the anomalous resistivity, where

$$\rho_{xy}^{AHE} = S_H \rho_{xx}^2 M_s \tag{6.7}$$

for an intrinsic effect. A graph of S_H against temperature is shown in Figure 6.12 as the blue markers. For temperatures down to approximately 60 K, S_H remains constant within error i.e. both S_H and R_0 are virtually independent of T. Graphs of ρ_{xy}^{AHE} against field along with the calculated dependence from equation 6.7 using the measured M_s and ρ_{xx} with a single fit parameter S_H are shown in Figure 6.13 for the high temperature regime.

The two curves of ρ_{xy}^{AHE} and the dependence from equation 6.7 show good agreement at high fields where both M_s and ρ_{xx} have saturated linearly. However there exists a region depicted by the black arrows where the curves don't correspond well. This region follows the same field range as the feature in ρ_{xx} as shown in Figure 6.14 for 160 K. Here the blue curve represents ρ_{xx}. The curves for ρ_{xy}^{AHE} and the dependence from equation 6.7 in the intermediate range of temperatures down to 80 K are shown in Figure 6.15. As the magnitude in the

ρ_{xx} feature decreases (Figure 6.9(b)) then the show better agreement. Around 80 K almost exact agreement is seen between the curves of ρ_{xy}^{AHE} and the dependence from equation 6.7, continuing to 60 K as shown in Figure 6.16 (a). Curves for ρ_{xy}^{AHE} are shown in Figure 6.16(b) where a value of n=$3.125 \pm 0.2 \times 10^{22} cm^{-3}$ is assumed for 40 K and 30 K after being calculated for 10 K from the curves in Figure 6.11. As one can see below approximately 50 K the fits has strongly deviated from the data. The significance of the data and fits shall now be discussed in the next section.

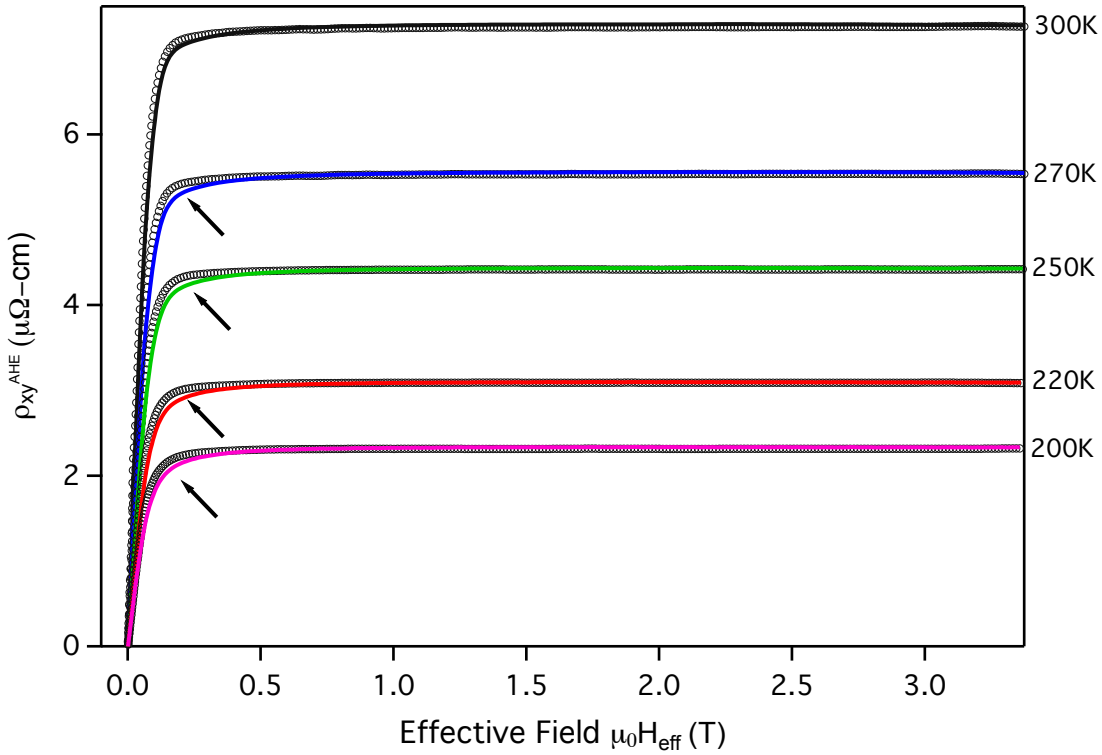

Figure 6.13: *The anomalous Hall resistivity ρ_{xy}^{AHE} against the effective field in the sample, S3, shown as the coloured filled lines between 300 K and 200 K. The dependence from equation 6.7 using the temperature independent scaling factor S_H are shown as open markers. The black arrows dictate the region where the two curves show poor agreement.*

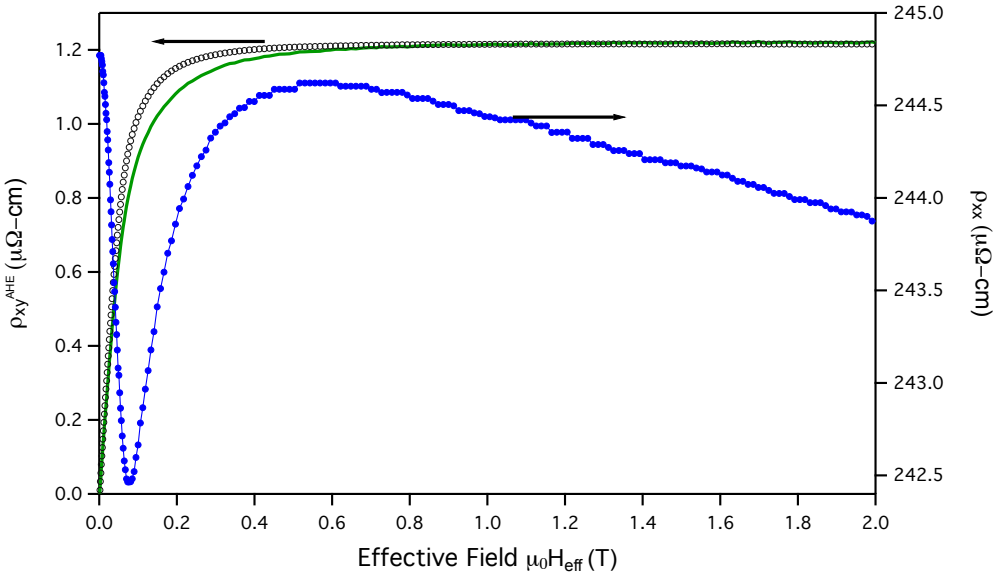

Figure 6.14: *The anomalous Hall resistivity ρ_{xy}^{AHE} at 160 K against the effective field in the sample, S3, shown as the green filled lines. The dependence from equation 6.7 using the temperature independent scaling factor S_H are shown as open markers. The blue curve represents the corresponding ρ_{xx} curve at 160 K. The feature in ρ_{xx} corresponds to the region over which ρ_{xy}^{AHE} and the dependence from equation 6.7 don't correspond.*

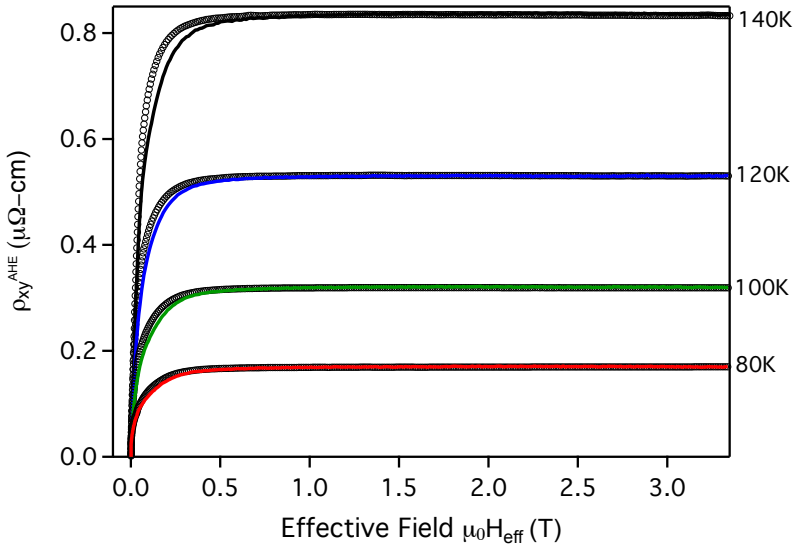

Figure 6.15: *The anomalous Hall resistivity ρ_{xy}^{AHE} against the effective field in the sample, S3, shown as the coloured filled lines, between 140 K and 80 K. The dependence from equation 6.7 using the temperature independent scaling factor S_H are shown as open markers.*

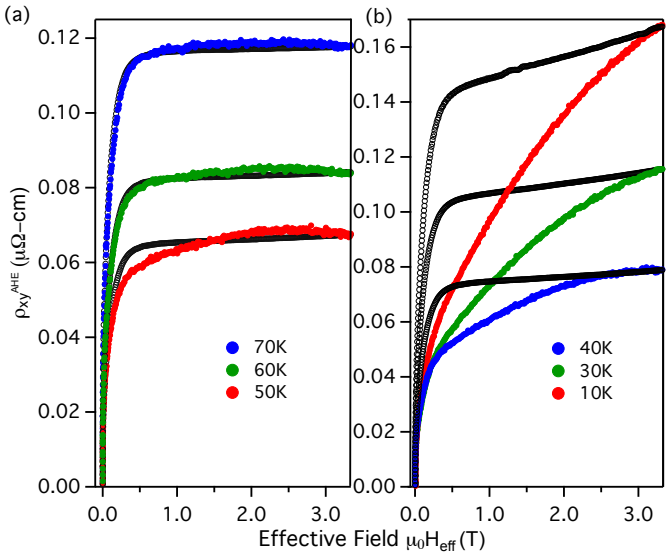

Figure 6.16: *The anomalous Hall resistivity ρ_{xy}^{AHE} against the effective field in the sample, S3, shown as the coloured filled lines. The dependence from equation 6.7 using the temperature independent scaling factor S_H are shown as open markers.*

6.3 Discussion

Single crystals were succesfully isolated from the samples grown by Andrew Wills, UCL. Laue patterns show good crystallinity and on the 3 samples measured relatively high values of RRR are obtained. The crystal with the highest RRR, S3, was used in all results reported here. The measured magnetisation curves in in Figure 6.4 were corrected for a demagnetising factor of $N = 0.69$ to obtain the curves in Figures 6.5 and 6.6 and the effective field on the sample throughout the rest of the analysis.

An explanation of the how the demagnetising factor was determined is analogous to the Meissner effect in a superconductor. For a superconductor in a small applied field, the Meissner effect gives $B = 0$ in the materials interior, at lengths deeper than the penetration. Similarly for an Ising ferromagnet where locally the magnetisation is $M = \pm M_s$, if small fields below saturation are considered then for

$$\mathbf{B} = \mu_0(\mathbf{H} + \mathbf{M}) \tag{6.8}$$

then $H = 0$. For a small needle with uniform magnetisation within a larger

sample there is an energy $-\mu_0 M.H_{eff}$ where H_{eff} is the field from all currents outside the needle. Locally energy would be lowered by aligning M to H_{eff}. For a course grained ellipsoid M and H are uniform, therefore if there domains of both type we must have $H_{eff} = 0$. This is not just restricted to Ising magnets and for the material as a whole,

$$H_{eff} = H_{app} - NM \tag{6.9}$$

and therefore $M = H_{app}/N$. Then measuring a sample in a magnetometer as done here, raw curves of the type shown in Figure 6.4 are obtained. The demagnetising factor is then obtained from the slope between $\pm M_s$. Therefore if we plot M vs H_{eff} we would have an infinite slope for susceptibility, dM/dH, at the origin and the magnetisation changes from $-M_s$ to $+M_s$. In the case studied here a value of $N = 0.69$ was obtained from Figure 6.4.

The magnetisation at low fields applied along the c-axis is shown in Figure 6.6 for all measured temperatures. At high temperatures shown in Figure 6.6 (a) dM/dH is not infinite crossing the origin so it does not look like the case of a ferromagnet described above. Previous measurements discussed in Chapter 5 showed the moments lay along the c-axis for polycrystalline samples at high temperatures. However the moments at high temperature in the single crystal measured here require an extra energy for putting M along the c-axis as shown in Figure 6.6 (a). The moments are then clearly in the a-b plane at high temperature in a single crystal. An applied field, H_{app} of almost 0.2 T is required to align the spins along H. If we imagine the sample as an ellipsoid with the magnetisation along one of its principle axis then there will be a demagnetising energy given by

$$E = \int \frac{NM^2}{2}\mu_0 \tag{6.10}$$

for putting the moments along H. The applied field, H_{app} to turn the moments is then

$$H_{app} = \frac{NM}{2} \tag{6.11}$$

which gives a value of 0.28 T for $M = 2\mu_B$ per Fe, close agreement with the measured H_{app} of 0.2 T.

The magnetisation curves at low fields for lower temperatures are then shown in Figure 6.6 (b) and (c). At 100 K dM/dH is infinite at the origin for

low values of magnetisation, there is then a component of the moments now along the c-direction. As the temperature is decreased further below 80 K this component along c quickly disappears as shown in Figure 6.6 (c). The magnetic structure in the single crystals of Fe_3Sn_2 is then significantly different from that of polycrystals. The difference is then accounted for by considering the demagnetising factor of the plate shaped samples. At high temperatures the moments are not along the c-axis but instead point towards the a-b plane. Upon cooling the moments gain a component along the c-axis which maximises between 100 - 80 K. Below 80 K this component quickly decays and the moments rotate back towards the a-b plane.

The measured anomalous Hall effect and magnetoresistance also show interesting details. The temperature dependence of R_0 is shown in Figure 6.12 as the red markers, deduced from the slope of ρ_{xy} at high fields. In the range 300 K - 80 K a carrier concentration of $n = 1.45 \pm 0.15 \times 10^{22} cm^{-3}$ holes was calculated. This is in relative agreement with previous experiments [80]. Values of $R_0 H_s$ were then substracted from ρ_{xy} to give curves of ρ_{xy}^{AHE} which has the dependence shown in equation 6.7. Values of S_H deduced from equation 6.7 are also shown in Figure 6.12 as the blue markers. S_H and R_0 are both temperature independent going from 300 K to $\approx$ 70 K while in the same temperature range the resistivity of the sample decreases ten fold. R_0 and S_H are then physically meaningful and hence ρ_{xy}^{AHE} scales as a function of ρ_{xx}^2 and is independent of τ. The dominant contribution to the AHE is then most likely the intrinsic effect. Attempts were also made for a scaling relationship of $\rho_{xx} M_s$ to look for skew scattering. But no significant improvement was seen in terms of the fit or scaling relationships.

The curves of ρ_{xy}^{AHE} in Figure 6.13 however show a clear anomaly when compared to the curves of the dependence from equation 6.7. This anomaly occurs over the same region the anomaly in magnetoresistance also occurs as shown clearly in Figure 6.14. The difference between the curves of ρ_{xy}^{AHE} and the dependence shown in equation 6.7 is denoted ρ_{xy}^{*} given by

$$\rho_{xy}^{*} = \rho_{xy}^{AHE} - S_H \rho_{xx}^2 M_s. \tag{6.12}$$

Curves of ρ_{xy}^{*} normalised to the zero field resistivity, ρ_{xx}, squared are shown in Figure 6.17. Normalisation to ρ_{xx}^2 was done due to its relationship with the intrinsic Hall effect. If a topological Hall effect similiar to that seen in MnSi

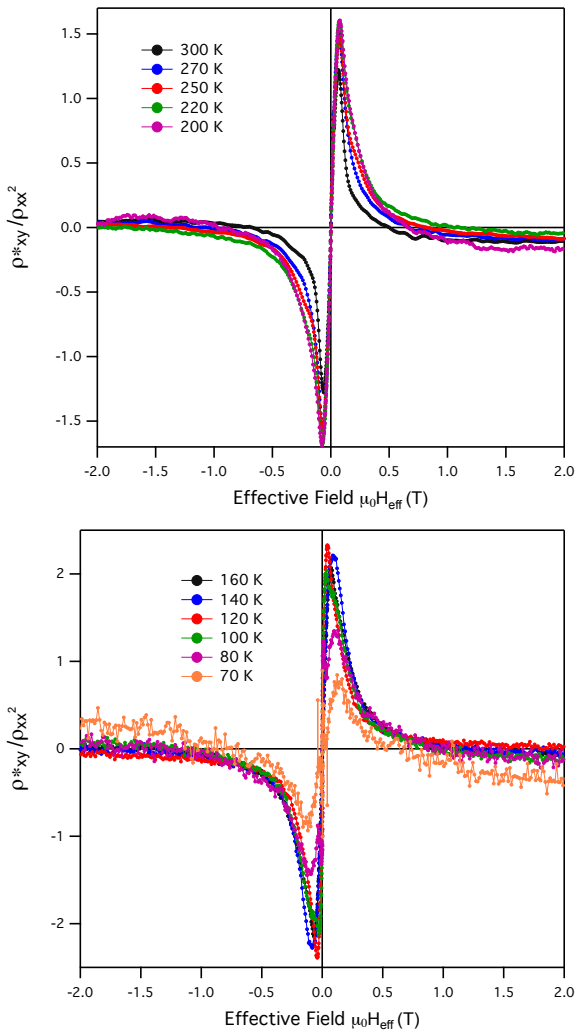

Figure 6.17: *A graph of fits equal to* $S_H\rho_{XX}^2 M_s - \rho_{xy}^{AHE}$ *normalised to the zero field resisitivity* ρ_0 *for a range of temperatures.*

discussed in Chapter 5 was present, the total Hall resistivity would then be

$$\rho_{xy} = R_0 H_s + \rho^{AHE} + \rho_{xy}^T \tag{6.13}$$

where ρ_{xy}^T is the topological Hall resistivity. Then ρ_{xy}^T would be equal to ρ_{xy}^* described above.

The cause of the topological Hall effect like signal can't be determined without more knowledge of the magnetic structures involved. Field induced static Skyrmions would cause a topological Hall effect like that seen in MnSi at ambient pressure by Neubauer *et al.* [72] and high pressure by Ritz *et al.* [73] discussed in

Chapter 5. The presence of Skyrmion excitations was recently predicted in the Kagome lattice by Pereiro *et al.* [**?**], however the signal here is more suggestive of static Skyrmions like those in MnSi. Ikoma *et al* also predicted possible exotic magnetic phases in the Kagome lattice in the phase boundary between chiral and ferromagnetic states. It would then be possible an exotic canted structure existed in the region before magnetic saturation causing a topological Hall effect. This would then fit our data quite well.

The temperature trend of the possible topological Hall effect follows well with that of the magnetisation. At high temperature the magnetic moments in the single crystal lay close to the *a*-*b* plane. Upon cooling a component of magnetisation is seen along the *c*-axis. Corresponding to this is an increase in the magnitude of the anomaly in magnetoresistance associated with the topological Hall effect upon cooling, shown in Figure 6.8 (b). The magntiude of the anomaly in magnetoresistance peaks at $\approx$ 160 K then disappears on further cooling below 80 K, shown in Figure 6.9 (b). In the magnetisation data the increasing component along *c* peaked at $\approx$ 100 K before decreasing dramatically again below 80 K. The magnetic structure causing the topological Hall effect may then require a component along *c* that peaks around 160 K and as the *c* component grows towards 100 K the topological Hall effect is decreased again.

However there could be other explanations for this inconsistency of Hall signal with the magnetisation that does not involve a topological Hall effect. Changes of the magnetic structure under low applied fields before saturation could cause changes in the normal Hall effect and hence n. This could then also explain the anomaly in magnetoresistance due to a change in n. Recently Nakatsuji *et al.* [84] considered the anomalous Hall effect in a non-collinear anti-ferromagnet Mn_3Ge also with a hexagonal structure which gave a large signal. Such an effect could also be present in Fe_3Sn_2.

The anomaly in magnetoresistance and topological Hall effect signal disappears below approximately 70 K. A rotation towards the *a*-*b* plane is then evident below 80 K in the magnetisation data shown in Figure 6.6 (c). The magnetisation, Hall effect and magnetoresistance curves then indicate a magnetic transition has taken place below 80 K. Fenner *et al.* [75] recently measured a re-entrant spin glass below 80 K in Fe_3Sn_2 in polycrystalline samples. The single crystal sample measured here may also be entering this spin glass state or another frustrated

magnetic structure. Further work needs to be carried out to deduce the magnetic structure causing the topological Hall effect signal and the structure below 80 K. The size of the single crystal samples makes neutron diffraction difficult. Although the detection of Skyrmions may be possible in a small angle neutron scattering experiment. Magnetisation measurements for the field applied along the *a*-*b* plane would provide some more evidence for the magnetic structure. Torque magnetometry would also provide more information of the magnetic structure. Some of these suggested experiments are to be carried in the near future.

Chapter 7

Summary and Outlook

7.1 SnTe

Recently topological insulators have emerged as a major topic in condensed matter physics and in this thesis an introduction was given to how these states occur. The semiconductor SnTe belongs to the class of materials known as crystalline topological insulators, where surface states are caused by Dirac cones crossing the band gap. The states are produced by a band inversion at the [1,1,1] direction L point and protected by the mirror symmetry of its fcc crystal structure. However SnTe's large free carrier concentration due to non-stoichiometry make the surface states difficult to detect in transport measurments. Other authors have however detected Dirac like bands just below the Fermi energy in ARPES experiments [10].

Previous authors detected signs of a structural transition in SnTe driven by a soft transverse optic phonon using a variety of different techniques. The structural transition was predicted to be a displacement of the two fcc sublattices along the [1,1,1] direction of the cube along with a corresponding rhombohedral shear angle. This transition was then expected to be ferroelectric in nature with a polar axis being formed by the displacement. There were no previous reports on succesfully measured ferroelectricty in SnTe due to the signal being drowned out by its high number of free carriers.

High quality single crystal samples of SnTe were grown that showed an anomaly in resistivity on cooling associated with a structural transition to the rhombohedral phase. Inelastic scattering was carried out on a single crystal

sample to measure its phonon dispersion curves throughout all high symmetry directions within the Brillouin zone at 300 K. DFT calculations carried out by Andreas Hermann matched well with the measured data. Upon cooling softening of the transverse optic phonon was measured near the zone centre. By extrapolation of linear fits to the data, an estimate of the phonon energy was made at the zone centre. At 75 K the phonon energy had decreased to zero indicating the lattice had become unstable. Upon further cooling the phonon energy was seen to recover to higher energies again at a rate almost 5 times faster than the softening. The recovery indicated a 2^{nd} order phase transition to a lower symmetry phase had taken place with a frozen in coordinate forming a polar axis. This is the first reported measurement of the structural transition in SnTe showing its ferroelectric nature.

Experiments carried out under high hydrostatic pressures showed the ferroelectric transition was suppressed above 6 kbar. Quantum oscillations were used as a probe in determining the extremal Fermi surface area in both the ferroelectric and fcc phases. In the ferroelectric phase 4 oscillation frequencies were measured in contrast to a single frequency measured in the fcc phase under high pressure. The ferroelectric transition then also causes a distortion of the Fermi surface. Why there are 4 different frequencies instead of just 2 due to the formation of the polar axis is still to be determined, although further change in Fermi surface shape could also cause another doubling leading to 4. Fermi surface calculations are ongoing. An increase of effective mass from $m^* = 0.25 \pm 0.03 m_e$ to $m^* = 0.30 \pm 0.03 m_e$ going from the ferroelectric to fcc is also detected from the temperature damping of the quantum oscillations. Further evidence of the change in effective mass was seen in the velocity of sound deduced from acoustic phonon branches. This increase corresponds to the band gap opening in the fcc phase. A change in electron-phonon coupling in the soft TO phonon going from fcc phase to the ferroelectric phase was also measured corresponding to a possible shift in the bandgap accoding to previous results [19].

Large changes in the measured Hall resisitivity were seen following the suppression of the ferroelectric phase with pressure. This may be accounted for by considering the various contributions each pocket in the distorted Fermi surface makes to the carrier concentration. However there is also a significant change in the curvature of the Hall resistivity after ferroelectric suppression at low fields.

The curvature may correspond to more than one band contributing to the Hall signal of different conductivities. A high conductivity band corresponding to a surface state in the Hall signal of SmB_6 has recently been reported [61]. A similiar high conductivity band may be the cause of the curvature seen in our measurements from the surface states in SnTe. In the ferroelectric phase surface states still exist according to the theoretical predication [11]. However in the fcc phase more symmetry and hence surface states exist. Therefore the conductivity of the surface band becomes higher in the fcc phase giving the change in measured curvature. Multiband models are ongoing to fit the measured Hall resistivity.

As well as the multiband model other future work includes a close comparison with band structure and Fermi surface calculations. A repeat of the experiment under pressure for different crystals and orientations would provide more evidence for the change in Hall resistivity curvature and multiband theory. The surface states in SnTe are predicted to be quantum Hall like [11], so a measurement to higher fields may reveal signals that could be attributed to this state as done recently in Bi_2Se_3 using quantum oscillations [85].

7.2 Fe_3Sn_2

The anomalous Hall effect in ferromagnets has been a recurring problem in condensed matter physics due to its many contributions. Both intrinsic and extrinsic effects have been introduced in this thesis. Particular emphasis was placed on the topological nature of the intrinsic effect caused by the Bloch band Berry curvature. Topological Hall effects caused by real space Berry phases in exotic magnetic structures such as Skyrmions in MnSi are also discussed. The material Fe_3Sn_2 which has a bilayer Kagome lattice was discussed with respect to its canted magnetic structure upon cooling in polycrystals. Previous reports measured the moments to point along the c-axis at high temperatures then rotate towards the a-b plane on cooling before entering a spin glass phase at 80 K [75].

The anomalous Hall effect was investigated in single crystals of Fe_3Sn_2 grown by Andrew Wills, UCL. Magnetisation measurements indicate for single crystal samples the moments lay in the a-b plane at high temperatures rather than along the c-axis. The difference is accounted for by considering the demagnetising factor for the plate shaped single crystals. A component along the c axis is then

measured upon cooling cooling towards 100 K. Below 80 K the component along the c-axis decreases rapidly corresponding to a rotation back towards the a-b plane.

In the region between 300 K - 80 K the anomalous Hall effect is strongly intrinsic. An anomaly in the magnetoresistance and anomalous Hall effect is also measured that may correspond to a topological Hall effect. The magnitude of the anomaly increases on cooling to $\approx$ 160 K before decreasing on further cooling and disappearing below 70 K. The cause of this topological Hall like signal is unknown but may be due to an exotic magnetic structure such as Skyrmions. Recently Skyrmion excitations were predicted in the Kagome lattice [81], however the measured signal is more like that caused by static Skyrmions in MnSi. Other exotic magnetic structures are predicted to be possible in the Kagome lattice when exchange between itinerant and localised spins is considered [82]. More knowledge of the magnetic structure in the low field region is then required to know the cause of the suspected topological Hall effect. Below 80 K magnetisation, Hall effect and magnetoresistance data show a new magnetic phase has been entered. This may be the spin glass phase previously seen in polycrystals [75].

More experiments are needed to deduce the magnetic structures in single crystals of Fe_3Sn_2. Sample size makes neutron diffraction difficult although currently attempts are being made to grow larger samples. Small angle neutron scattering may be useful to detect the presence of Skyrmions although no attempts have yet been made. Specific heat measurements are also currently being carried out to gain more information on the transition at 80 K. Further magnetisation measurements for the field applied along the a-b plane are also being carried out. Torque magnetometry would be a useful probe in this material to deduce the moment rotations as well as a close comparison with theory to determine magnetic structures as well as bandstructures.

Bibliography

[1] J. W. Zwanziger, M. Koenig, and A. Pines, "Berry's Phase," *Annu. Rev. Phys. Chem.*, vol. 41, pp. 601–46, 1990.

[2] M. Berry, "Quantal Phase Factors Accompanying Adiabatic Changes," *Proc. R. Soc. Lond. A*, vol. 392, pp. 45–57, 1984.

[3] D. Xiao, M.-C. Chang, and Q. Niu, "Berry Phase Effects on Electronic Properties," *Rev. Mod. Phys.*, vol. 82, pp. 1959–2007, Jul 2010.

[4] M. Z. Hasan and C. L. Kane, "*Colloquium* : Topological Insulators," *Rev. Mod. Phys.*, vol. 82, pp. 3045–3067, Nov 2010.

[5] Y. Hatsugai, "Topological Aspects of the Quantum Hall Effect," *Journal of Physics: Condensed Matter*, vol. 9, no. 12, p. 2507, 1997.

[6] C. L. Kane and E. J. Mele, "Quantum Spin Hall Effect in Graphene," *Phys. Rev. Lett.*, vol. 95, p. 226801, Nov 2005.

[7] M. König, S. Wiedmann, C. Brüne, A. Roth, H. Buhmann, L. W. Molenkamp, X.-L. Qi, and S.-C. Zhang, "Quantum Spin Hall Insulator State in HgTe Quantum Wells," *Science*, vol. 318, no. 5851, pp. 766–770, 2007.

[8] Y. L. Chen, J. G. Analytis, *et al.*, "Experimental Realization of a Three-Dimensional Topological Insulator, Bi_2Te_3," *Science*, vol. 325, pp. 178–181, 07 2009.

[9] D. Hsieh, Y. Xia, *et al.*, "A Tunable Topological Insulator in the Spin Helical Dirac Transport Regime," *Nature*, vol. 460, pp. 1101–1105, 08 2009.

[10] Y. Tanaka, Z. Ren, T. Sato, K. Nakayama, S. Souma, T. Takahashi, K. Segawa, and Y. Ando, "Experimental Realization of a Topological Crystalline Insulator in SnTe," *Nat Phys*, vol. 8, pp. 800–803, June 2012.

[11] T. Hsieh, H. Lin, J. Liu, W. Duan, A. Bansil, and L. Fu, "Topological Crystalline Insulators in the SnTe Material Class," *Nat Comm*, vol. 3, p. 982, February 2012.

[12] S.-Y. Xu, C. Liu, *et al.*, "Observation of a Topological Crystalline Insulator Phase and Topological Phase Transition in $Pb_{1-x}Sn_xTe$," *Nat Commun*, vol. 3, p. 1192, 11 2012.

[13] R. Brebrick, "Deviations from Stoichiometry and Eletrical Properties in SnTe," *J. Phys. Chem. Solids*, vol. 24, pp. 27–36, 1963.

[14] H. Savage, B. Houston, and J. J.R. Burke, "Fermi-Surface Studies in SnTe," *Phys. Rev. B*, vol. 6, pp. 2292–2304, February 1972.

[15] R. F. Bis and J. R. Dixon, "Applicability of Vegard's Law to the $Pb_xSn_{1-x}Te$ Alloy System," *Journal of Applied Physics*, vol. 40, no. 4, pp. 1918–1921, 1969.

[16] Y. W. Tung and M. L. Cohen, "Relativistic Band Structure and Electronic Properties of SnTe, GeTe, and PbTe," *Physical Review*, vol. 180, pp. 823–826, 04 1969.

[17] K. Rabe and J. Joannopoulos, "Ab Initio Relativistic Pseudopotential Study of the Zero-Temperature Structural Properties of SnTe and PbTe," *Phys. Rev. B*, vol. 32, pp. 2302–2314, February 1985.

[18] S. Rabii, "Energy-Band Structure and Electronic Properties of SnTe," *Phys. Rev.*, vol. 182, pp. 821–828, December 1969.

[19] P. Littlewood, B. Mihaila, *et al.*, "Band Structure of SnTe studied by Photoemission Spectroscopy," *Phys. Rev. Lett.*, vol. 105, p. 086404, August 2010.

[20] J. O. Dimmock, I. Melngailis, and A. J. Strauss, "Band Structure and Laser Action in $Pb_xSn_{1-x}Te$," *Physical Review Letters*, vol. 16, pp. 1193–1196, 06 1966.

[21] M. Dove, *Introduction to Lattice Dynamics*. No. 4 in Cambridge topics in Mineral Physics and Chemistry, 9780511619885: Cambridge University Press, 1993.

[22] Chandra, P. and Littlewood, P. B., "A Landau Primer for Ferroelectrics," *eprint arXiv:cond-mat/0609347*, 2006.

[23] G. Shirane and Y. Yamada, "Lattice-Dynamical Study of the 110° K Phase Transition in $SrTiO_3$," *Physical Review*, vol. 177, pp. 858–863, 01 1969.

[24] G. Shirane, J. D. Axe, J. Harada, and J. P. Remeika, "Soft Ferroelectric Modes in Lead Titanate," *Physical Review B*, vol. 2, pp. 155–159, 07 1970.

[25] G. S. Pawley, W. Cochran, R. A. Cowley, and G. Dolling, "Diatomic Ferroelectrics," *Phys. Rev. Lett.*, vol. 17, pp. 753–755, October 1966.

[26] H. Alperin, S. Pickart, J. Rhyne, and V. Minkiewicz, "Softening of the Tranverse-Optic Mode in PbTe," *Physics Letters*, vol. 40A, no. 4, pp. 295–296, 1972.

[27] E. Cowley, J. Darby, and G. Pawley, "The Lattice Dynamics of Tin Telluride," *J. Phys. C (Solid St. Phys.)*, vol. 2, pp. 1916–1925, October 1969.

[28] L. Muldawer, "New Studies of the Low Temperature Transformation in SnTe," *J. Nonmetals*, vol. 1, pp. 177–182, June 1973.

[29] K. Kobayashi, Y. Kato, Y. Katayama, and K. Komatsubara, "Carrier-Concentration-Dependent Phase Transition in SnTe," *Phys. Rev. Lett.*, vol. 37, pp. 772–774, February 1976.

[30] M. Iizumi, Y. Hamaguchi, K. Komatsubara, and Y. Kato, "Phase Transition in SnTe with Low Carrier Concentration," *Journal of the Physical Society of Japan*, vol. 38, pp. 443–449, September 1975.

[31] L. Brillson, E. Burstein, and L. Muldawer, "Raman Observation of the Ferroelectric Phase Transition in SnTe," *Phys. Rev. B*, vol. 9, pp. 1547–1551, July 1974.

[32] K. Kobayashi, Y. Kato, Y. Katayama, and K. Komatsubara, "Resistance Anomaly due to Displacive Phase Transition in SnTe," *Solid State Commun.*, vol. 17, pp. 875–878, October 1975.

[33] S. Katayama and D. Mills, "Theory of Anomalous Resisitivity Associated with Structural Phase Transitions in IV-Vi Compounds," *Phys. Rev. B*, vol. 22, no. 1, pp. 336–352, 1980.

[34] A. J. Bevolo, H. R. Shanks, and D. E. Eckels, "Molar Heat Capacity of GeTe, SnTe, and PbTe from 0.9 to 60 K," *Physical Review B*, vol. 13, pp. 3523–3533, 04 1976.

[35] I. Hatta and K. Kobayashi, "Mean-Field Behaviour of the Specific Heat at the Phase Transition of SnTe with a Low Carrier Concentration," *Solid State Commun.*, vol. 22, pp. 775–777, 1977.

[36] E. K. H. Salje, D. J. Safarik, *et al.*, "Tin Telluride: A weakly co-elastic metal," *Physical Review B*, vol. 82, pp. 184112–, 11 2010.

[37] J. R. Burke, R. S. Allgaier, B. B. Houston, J. Babiskin, and P. G. Siebenmann, "Shubnikov-de Haas Effect in SnTe," *Physical Review Letters*, vol. 14, pp. 360–361, 03 1965.

[38] D. Shoenberg, *Magnetic Oscillations in Metals*, vol. 1. Cambridge University Press, 1984.

[39] R. S. Allgaier and B. Houston, "Weak-Field Magnetoresistance and the Valence-Band Structure of SnTe," *Physical Review B*, vol. 5, pp. 2186–2197, 03 1972.

[40] G. Abdul-Jabbar, *The Emergence of Magnetic Order in the Rare Earth Intermetallic PrPtAl*. PhD thesis, University of Edinburgh Physics, James Clerk Maxwell Building King's Buildings, October 2014.

[41] I. Sheikin, "Introduction to de Haas van Alphen Effect-CM-DTC lecture course," 2013.

[42] A. Q. R. Baron, "Introduction to High-Resolution Inelastic X-Ray Scattering," *e-print http://arxiv.org/pdf/1504.01098.pdf*, 2015.

[43] G. Shirane, S. Shapiro, and J. Tranquada, *Neutron Scattering with a Triple-Axis Spectrometer*, vol. 1. Cambridge University Press The Edinburgh Building Cambridge: Cambridge University Press, 2002.

[44] P. Chaikin and T. Lubensky, *Principles of Condensed Matter Physics*. Cambridge University Press The Edinburgh Building Cambridge: Cambridge University Press, 5 ed., 1995.

[45] www.esrf.eu/UsersAndScience/Experiments/DynExtrCond/ID28/BeamlineLayout, "ESRF website ID28 beamline.," June 2015.

[46] C.Stock, R. Birgeneau, S. Wakimoto, J. Gardener, W.Chen, Z. Ze, and G. Shirane, "Universal Static and Dynamic Properties of the Stucural Transition in Pb(ZnNb)O_3," *Phys. Rev. B*, vol. 69, p. 094104, March 2004.

[47] E. Burkel, "Phonon Spectroscopy by Inelastic X-ray Scattering," *Rep. Prog. Phys*, vol. 63, no. 2, pp. 171–232, 2000.

[48] M. Holt, Z. Wu, H. Hong, P. Zschack, P. Jemian, J. Tischler, H. Chen, and T. C. Chiang, "Determination of Phonon Dispersions from X-Ray Transmission Scattering: The Example of Silicon," *Physical Review Letters*, vol. 83, pp. 3317–3319, 10 1999.

[49] G. Kresse and J. Furthmüller, "Efficient Iterative Schemes for *ab initio* Total Energy Calculations Using a Plane Wave Basis Set," *Phys. Rev. B*, vol. 54, pp. 11169–11186, 1996.

[50] G. Kresse and D. Joubert, "From Ultrasoft Pseudopotentials to the Projector Augmented-Wave," *Phys. Rev. B*, vol. 59, pp. 1758–1775, 1999.

[51] K. B. John P. Perdew and M. Ernzerhof, "Generalized Gradient Expansion Made Simple," *Phys. Rev. Lett.*, vol. 77, pp. 3865–3868, 1996.

[52] D. Alfé, "PHON:A Program to Calculate Phonons Using the Small Displacement Method," *Comput. Phys. Commun.*, vol. 180, no. 12, pp. 2622–2633, 2009.

[53] P.Souvatzis, O.Eriksson, M. Katsnelson, and S. Rudin, "Entropy Driven Stabilization of Energetically Unstable Crystal Structures Explained from First principles Theory," *Phys. Rev. Lett.*, vol. 100, no. 9, p. 95901, 2008.

[54] J. A. Kafalas and A. N. Mariano, "High-Pressure Phase Transition in Tin Telluride," *Science*, vol. 143, no. 3609, p. 952, 1964.

[55] Hall, H. T., "Ultra-High-Pressure, High-Temperature Apparatus: the "Belt"," *Review of Scientific Instruments*, vol. 31, pp. 125–131,, 1960.

[56] D. Zhou, Q. Li, Y. Ma, Q. Cui, and C. Chen, "Unraveling Convoluted Structural Transitions in SnTe at High Pressure," *The Journal of Physical Chemistry C*, vol. 117, pp. 5352–5357, 03 2013.

[57] G. J. Piermarini, S. Block, J. D. Barnett, and R. A. Forman, "Calibration of the Pressure Dependence of the R1 Ruby Fluorescence Line to 195 kbar," *Journal of Applied Physics*, vol. 46, no. 6, pp. 2774–2780, 1975.

[58] K. Imura, K. Matsubayashi, H. S. Suzuki, N. Kabeya, K. Deguchi, and N. K. Sato, "Pressure–Temperature Phase Diagram of Golden SmS," *Journal of the Physical Society of Japan*, vol. 78, p. 104602, 2015/06/24 2009.

[59] N. Tateiwa and Y. Haga, "Evaluations of Pressure-Transmitting Media for Cryogenic Experiments with Diamond Anvil Cell," *Review of Scientific Instruments*, vol. 80, no. 123901, 2009.

[60] N. W. Ashcroft and N. D. Mermin, *Solid State Physics*, vol. 1. Saunders College Publishing, 1976.

[61] D. J. Kim, S. Thomas, T. Grant, J. Botimer, Z. Fisk, and J. Xia, "Surface Hall Effect and Nonlocal Transport in SmB_6: Evidence for Surface Conduction," *Sci. Rep.*, vol. 3, 11 2013.

[62] N. Nagaosa, J. Sinova, S. Onoda, A. H. MacDonald, and N. P. Ong, "Anomalous Hall Effect," *Rev. Mod. Phys.*, vol. 82, pp. 1539–1592, May 2010.

[63] R. Karplus and J. M. Luttinger, "Hall Effect in Ferromagnetics," *Phys. Rev.*, vol. 95, pp. 1154–1160, Sep 1954.

[64] J. Smit, "The Spontaneous Hall Effect in Ferromagnetics II," *Physica*, vol. 24, no. 1–5, pp. 39–51, 1958.

[65] L. Berger, "Side-Jump Mechanism for the Hall Effect of Ferromagnets," *Phys. Rev. B*, vol. 2, pp. 4559–4566, Dec 1970.

[66] N. P. Ong and W. L. Lee, "Geometry and the Anomalous Hall Effect in Ferromagnets," *Foundations of Quantum Mechanics in the Light of New Technology (Proceedings of ISQM Tokyo 2005), edited by S. Ishioka and K. Fukikawa (World Scientific, Singapore) p121*, 2006.

[67] A. Pippard, *Magnetoresistance in Metals*, vol. 1 of *Cambridge studies in low temperature physics*. Cambridge University Press The Edinburgh Building Cambridge: Cambridge University Press, 1 ed., 1989.

[68] F. D. M. Haldane, "Berry Curvature on the Fermi Surface: Anomalous Hall Effect as a Topological Fermi-Liquid Property," *Phys. Rev. Lett.*, vol. 93, p. 206602, Nov 2004.

[69] S. Mühlbauer, B. Binz, F. Jonietz, C. Pfleiderer, A. Rosch, A. Neubauer, R. Georgii, and P. Böni, "Skyrmion Lattice in a Chiral Magnet," *Science*, vol. 323, pp. 915–919, 02 2009.

[70] S. Blundell, *Magnetism in Condensed Matter*. Oxford Master Series in Condensed Matter Physicstter physics, Oxford University Press, 1 ed., 2001.

[71] M. Lee, Y. Onose, Y. Tokura, and N. P. Ong, "Hidden Constant in the Anomalous Hall Effect of High-Purity Magnet MnSi," *Physical Review B*, vol. 75, pp. 172403–, 05 2007.

[72] A. Neubauer, C. Pfleiderer, B. Binz, A. Rosch, R. Ritz, P. G. Niklowitz, and P. Böni, "Topological Hall Effect in the *A* Phase of MnSi," *Physical Review Letters*, vol. 102, pp. 186602–, 05 2009.

[73] R. Ritz, M. Halder, C. Franz, A. Bauer, M. Wagner, R. Bamler, A. Rosch, and C. Pfleiderer, "Giant Generic Topological Hall Resistivity of MnSi Under Pressure," *Physical Review B*, vol. 87, pp. 134424–, 04 2013.

[74] B. Malaman and B. Roques, "Structure Cristalline du Stannure de Fer Fe_3Sn_2," *Acta Cryst.*, vol. B32, p. 1348, 1976.

[75] L. A. Fenner, A. A. Dee, and A. S. Wills, "Non-Collinearity and Spin Frustration in the Itinerant Kagome Ferromagnet Fe_3Sn_2," *Journal of Physics: Condensed Matter*, vol. 21, no. 45, p. 452202, 2009.

[76] G. Trumpy, E. Both, C. Djéga-Mariadassou, and P. Lecocq, "Mössbauer-Effect Studies of Iron-Tin Alloys," *Phys. Rev. B*, vol. 2, pp. 3477–3490, Nov 1970.

[77] G. L. Caer, B. Malaman, and B. Roques, "Mössbauer effect study of Fe_3Sn_2," *Journal of Physics F: Metal Physics*, vol. 8, no. 2, p. 323, 1978.

[78] G. L. Caer, B. Malaman, L.Haggstrom, and T. Ericsson, ""Magnetic Properties of Fe_3Sn_2.III. A^{119} Sn Mössbauer Study"," *Journal of Physics F: Metal Physics*, vol. 9, no. 9, p. 1905, 1979.

[79] B. Malaman, D. Fruchart, and G. L. Caer, "Magnetic Properties of Fe_3Sn_2. II. Neutron Diffraction Study (and Mössbauer Effect)," *Journal of Physics F: Metal Physics*, vol. 8, no. 11, p. 2389, 1978.

[80] T. Kida, L. A. Fenner, A. A. Dee, I. Terasaki, M. Hagiwara, and A. S. Wills, "The Giant Anomalous Hall Effect in the Ferromagnet Fe_3Sn_2 —a Frustrated Kagome Metal," *Journal of Physics: Condensed Matter*, vol. 23, no. 11, p. 112205, 2011.

[81] M. Pereiro, D. Yudin, J. Chico, C. Etz, O. Eriksson, and A. Bergman, "Topological Excitations in a Kagome Magnet," *Nat Commun*, vol. 5, 09 2014.

[82] D. Ikoma, H. Tsuchiura, and J.-i. Inoue, "Magnetic Phase Diagram of Metallic Pyrochlore Lattice in the Double-Exchange Model," *Physical Review B*, vol. 68, pp. 014420–, 07 2003.

[83] M. McElfresh, "Fundamentals of Magnetism and Magnetic Measurements featuring Quantum Design's Magnetic Property Measurement System,"

[84] S. Nakatsuji, N. Kiyohara, and T. Higo, "Large Anomalous Hall Effect in a non-Collinear Antiferromagnet at Room Temperature," *Nature*, vol. 527, pp. 212–215, 11 2015.

[85] J. G. Analytis, R. D. McDonald, S. C. Riggs, J.-H. Chu, G. S. Boebinger, and I. R. Fisher, "Two-Dimensional Surface State in the Quantum Limit of a Topological Insulator," *Nat Phys*, vol. 6, pp. 960–964, 12 2010.

Publications

Modulated magnetism in PrPtAl. Gino Abdul-Jabbar, Dmitry A. Sokolov, *Christopher D. O'Neill*, Christopher Stock, Didier Wermeille, Franz Demmel, Frank Krüger, Andrew G. Green, Florence Lévy-Bertrand, Béatrice Grenier and Andrew D. Huxley: Nature Physics 11, 321327 (2015)